Quantum Chaotic Scattering and Ballistic Electron Transport in Microcavities

A Dissertation
Presented to the Faculty of the Graduate School
of
Yale University
in candidacy for the degree of
Doctor of Philosophy

by
Mark William Keller

May 1995

ABSTRACT

Quantum Chaotic Scattering and Ballistic Electron Transport in Microcavities

Mark William Keller
Yale University
1995

Experiments are reported on quantum electron transport in micon-sized cavities made from the two-dimensional electron gas of a GaAs/AlGaAs heterostructure. The cavities are fabricated in a manner that allows the electron density to be varied by a gate voltage without affecting the cavity size or shape. Various cavity shapes are studied for which the classical scattering is either chaotic or non-chaotic. At low temperature (≈ 0.1 K) the conductance of the cavities exhibits fluctuations as a function of magnetic field or Fermi wavevector. The power spectra of these fluctuations are compared to a semiclassical theory of chaotic scattering, and the typical area enclosed and length traveled by the electrons are extracted for each cavity. The typical areas and lengths are compared with the expected values from simulations, and the extent of disorder in the cavities is inferred from the comparison. The weak localization effect in the cavities is also studied. The ensemble average behavior is constructed explicitly by measuring the weak localization at many different values of Fermi wavevector for each cavity. The weak localization is compared with simulations and found to agree remarkably well with no adjustable parameters. For both the fluctuations and the weak localization, the behavior of a nominally non-chaotic cavity could not be distinguished from that of the chaotic cavities.

Acknowledgements

Many students who came before me helped create a strong tradition of experimental and theoretical work in mesoscopic physics at Yale. Their work set a high standard and provided a valuable foundation as I tried to make my own contribution to the tradition. Several former ProberLab graduates provided help and/or wisdom, especially Venkat Chandrasekhar and Mike Rooks. My immediate predecessor was Steve Klepper, who patiently answered my questions and demonstrated the value of being careful and persistent in doing experiments.

The idea for my thesis research came from Oded Millo, who developed fabrication methods and made measurements with me during the first two years of the work. Oded and I learned many experimental techniques together, since he came to the group from a background in surface science, but he always managed to be a teacher at the same time. When the physics got murky, especially in the quantum chaos literature, I could count on Oded to get me unstuck.

Dan Prober was a constant source of encouragement and important physical insight as my thesis advisor. When frustration lowered my enthusiasm, his optimism helped me to keep plugging away. Dan's special qualities are reflected in the fact that I always felt I was treated more like a colleague than an employee, a feeling that not all graduate students enjoy.

I was fortunate to have a supportive group of faculty members for my thesis committee. Vic Henrich provided hospitality and an introduction to experimental physics during my first year at Yale. Doug Stone invested the time and effort to understand the practical limitations faced by experimentalists. Bob Wheeler was a source of enthusiasm and impressed me with his conviction that all phenomena observed in the lab can be understood, usually through a proper application of Maxwell's equations. Harold Baranger was a meticulous outside reader, and his comments improved my understanding of several important ideas.

In assembling the dilution regrigerator and preparing it for experiments, I had help from Anurag Mittal, Ellen Hornbeck, and Jeff Sleight, and software help from Peter Burke. Anurag spent long days and a few nights in the clean room and running the fridge with me, in addition to fostering my taste for fine coffee. I wish him well as he continues the quantum transport tradition of ProberLab.

Life at Yale was not all research, all the time. Besides the people mentioned above, those who contributed to the lighter side of life included officemates Rich

Steinberg and Nick Rizzo, labmates Mike Gaidis and Jim McCambridge, and buildingmates Paul McEuen, Paul Dresselhaus, Curt Richter, Rachel Lombardi, and Mark Amman. The help of many support staff, especially Pat Brodka, Jayne Miller, and Mary Lally, made dealing with procedures more pleasant.

Behind all my accomplishments at Yale were my parents and my wife Evelyn. Their love and support made this work possible. This dissertation is dedicated to the memory of my grandmother who fed my interest in math and science with a steady supply of puzzles and games.

Table of Contents

List of Figures and Tables

Table Page

List of Symbols and Abbreviations

$\langle f(x) \rangle_x$	Average of f over a range of x
$\propto$	Proportional to
$\approx$	Approximately equal to
$\in$	Element of
1D	One-dimensional
2D	Two-dimensional
2DEG	Two-dimensional electron gas
A	Directed area enclosed inside cavity
α	(Inverse of the typical area enclosed inside cavity) $\div 2\pi$
A_{tot}	Total cavity area
B	Magnetic field
DR	Dilution refrigerator
E	Energy of scattering particle
e	Electron charge
EBL	Electron beam lithography
ϕ_0	Flux quantum ($= h/e$)
FT	Fourier Transform
G	Conductance
γ	Inverse of the typical length traveled inside cavity
η	Inverse of the typical number of bounces inside cavity
h	Planck's constant
$\hbar$	Planck's constant $\div 2\pi$
Int[...]	Integer part of [...]
k, k_F	Electron Fermi wavevector
k_B	Boltzmann's constant
ℓ_ϕ	Electron phase coherence length
L	Length of path traveled inside cavity
L_{dir}	Direct distance between lead openings
LHe	Liquid Helium
LIA	Lock-in amplifier
LN2	Liquid nitrogen
MBE	Molecular beam epitaxy
MC	Mixing Chamber of the dilution refrigerator

n	Sheet density of electrons in the 2DEG
N	Number of bounces inside cavity
NID	Not intentionally doped
PMMA	Poly-methyl-methacrylate
PR	Photoresist
R	Resistance; Radius of stadium cavity
RuO	Ruthenium oxide
S	S matrix
S_B	Power spectrum of $G(B)$
S_k	Power spectrum of $G(k)$
T	Electron temperature
T_c	Characteristic temperature for quantum interference ($\equiv \hbar\theta/k_B$)
T_{mc}	Mixing Chamber temperature
t	Time spent inside cavity
θ	Inverse of the typical time spent inside cavity
τ_ϕ	Electron phase coherence time
UCF	Universal Conductance Fluctuations
v	Velocity of scattering particle
V_g	Gate voltage
W	Lead width
WL	Weak Localization

1

INTRODUCTION

The experiments described in this dissertation continue a thread of investigation into low temperature electronic conduction known as "mesoscopic physics". The name refers to the fact that the metallic conductors involved are larger than the atomic scale, but smaller than the macroscopic scale where transport can be described in terms of average intrinsic properties such as conductivity. The defining length scale for mesoscopic physics is the electron phase coherence length, since all mesoscopic effects arise from coherent scattering and interference of electron waves. There are some relatively famous effects associated with this branch of physics, such as the Aharonov-Bohm effect, Weak Localization, and Universal Conductance Fluctuations, that have been studied both theoretically and experimentally in Yale's Department of Applied Physics in the past. For general reviews of mesoscopic physics see Imry, 1995 (theory), and Washburn and Webb, 1986 (experiments).

One of the major concepts that arose from the early work in mesoscopic physics was the idea that electron transport through a phase coherent conductor is equivalent to a quantum scattering process (Landauer, 1970; Buttiker, 1986). Measurements of electrical resistance can be completely described in terms of a scattering matrix which couples incoming and outgoing scattering channels. The early mesoscopic experiments used metal film samples in which electron transport was diffusive, *i.e.*, electrons scattered from random impurities much more often than from the edges of the structure. The details of the scattering potential were not known, and the problem of transport was treated theoretically by averaging over all possible configurations of impurities with the same impurity density. In the last several years the development of GaAs/AlGaAs heterostructures with very high electron mobility has allowed access to a different regime of electron conduction, known as the ballistic regime because all large-angle electron scattering occurs at the edges of the structure rather than at random impurities. In this regime the quantum scattering from a particular scattering potential, determined by the sample shape, can be studied. Such samples offer an experimental system for studying the quantum scattering properties of shapes for which classical scattering is chaotic,

which is a topic of great interest recently. Chaotic scattering in both classical and quantum systems is described in Chapter 2.

Two familiar phenomena in mesoscopic physics are Universal Conductance Fluctuations (UCF) and Weak Localization (WL). Both effects have been thoroughly studied in diffusive conductors and are well understood in that context. For reviews, see Lee, Stone, and Fukuyama, 1987 (UCF) and Bergmann, 1984 (WL). UCF are seemingly random variations in conductance observed as the magnetic field, Fermi energy, or impurity configuration is changed. WL is a decrease in the average conductance (averaged over any of the parameters that produce the fluctuations) due to constructive interference of backscattered electrons in the presence of time-reversal symmetry. The experimental signal of WL is a minimum in conductance at zero magnetic field, since the field destoys the WL as it breaks time-reversal symmetry. Ballistic conductors also exhibit conductance fluctuations and a zero-field minimum in conductance that are exactly analogous to the effects seen in diffusive transport. The theory of these effects in ballistic cavities, and the influence of the chaotic or regular (= non-chaotic) dynamics of the classical analogues of the cavities, are described in Chapter 3.

Chapter 4 covers the design and fabrication of ballistic microcavities for experimental studies of quantum chaotic scattering. Two fabrication techniques, low energy ion exposure and shallow wet etch, were used to create cavities whose electron density could be changed (using an overlying metal gate) without affecting the shape. This is an important feature of the samples used in this work which was not shared by the samples used in studies of quantum chaotic scattering by other researchers.

Chapter 5 contains a description of the apparatus used to measure the conductance of the cavities as a function of magnetic field or Fermi energy at temperatures of about 100 mK. The dilution refrigerator system described here represents a significant advance in the facilities for low temperature experiments at Yale.

The experimental results for five ballistic cavities (four chaotic and one regular) are presented in Chapter 6. The power spectrum of the conductance fluctuations is used to find the typical area enclosed and typical length traveled by electrons before escape from each cavity. These areas and lengths are compared with values from numerical simulations. The WL for three of the cavities is also compared with numerical simulations. The fluctuations and WL in the regular

cavity are compared with the effects seen in the chaotic cavities. Some of the results for two of the chaotic cavities have been published: Keller *et al.*, 1994.

Chapter 7 contains a summary of the experimental results and a discussion of the conclusions that can be drawn from them. The findings are compared with recent studies of quantum chaotic scattering in similar ballistic cavities by Marcus *et al.*, 1992, Berry *et al.*, 1994a and 1994b, and Chang *et al.*, 1994.

2

THEORY OF CHAOTIC SCATTERING

2.1 Classical Chaotic Scattering

The fundamentals of classical chaos are covered in many textbooks and review articles. The article by Jensen, 1987 is a good overview and the textbook by Baker and Gollub, 1990 covers the basics quite well. Empirically, the defining feature of chaos is a lack of predictibility in a deterministic system due to an extreme sensitivity to initial conditions. To deal with chaos in scattering systems, the ideas of chaos in closed systems must be extended to the case of finite interaction time. This will first be illustrated using a model system which displays the main features of classical chaotic scattering. The specific case of scattering in chaotic cavities will then be described.

2.1.1 Three Disk Model System

The geometry of the three disk scattering system is shown in Figure 2.1a. A classical particle of fixed velocity approaches the scattering region at an angle Θ_{in}, scatters among the disks for a time τ_{trap}, and exits at an angle Θ_{out}. The scattering function $\Delta\Theta \equiv \Theta_{in} - \Theta_{out}$ is plotted as a function of the impact parameter b in Figure 2.1b. For most intervals of b the scattering function is a piecewise smooth function with a finite number of discontinuities. If the entire range of b showed this behavior, the scattering would be called regular (non-chaotic). However, near $b = 2.3$ and $b = 4.5$ the discontinuities in $\Delta\Theta$ become closely spaced and when the axis is expanded, as in Figure 2.1c, they are found to occur on all scales. It can be shown that $\Delta\Theta$ is singular at values of b which form a fractal set. (This feature of the scattering phase space is analogous to the fractal nature of the phase space of closed chaotic systems.) In any small interval of b around one of the singularities, $\Delta\Theta(b)$ varies wildly, and the amplitude of the variations in $\Delta\Theta(b)$ does not tend to zero as the size of the interval is reduced. This extremely sensitive dependence of a scattering function on an initial condition is the defining feature of chaotic scattering. As in closed chaotic systems, any uncertainty in initial conditions makes it impossible to predict the response of the system. The rigorous justification for labeling such scattering chaotic follows from an analysis

of the dynamics on the subset of phase space that represents unstable trapped trajectories (those which enter the scattering region but never leave). Particles that enter very near one of these trapped trajectories remain in the scattering region for a long time before finally escaping, and it is these trajectories which are responsible for the singularities in the scattering function. Figure 2.1d shows the correlation between a long trapping time and the rapid variations in $\Delta\Theta(b)$.

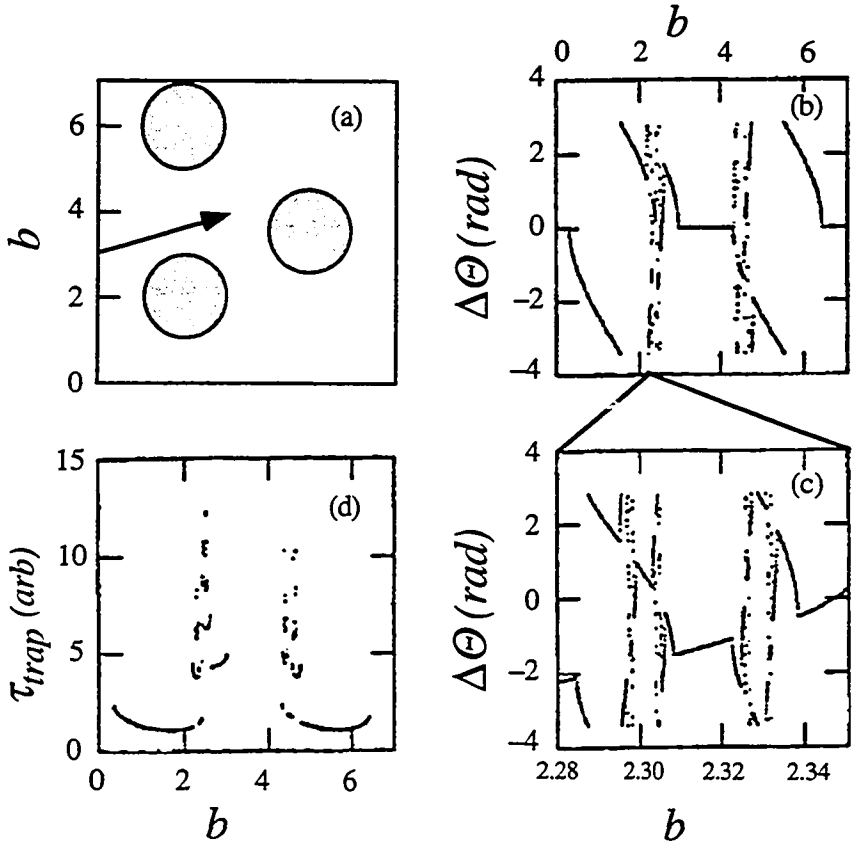

Figure 2.1 Three disk model system which displays the main features of classical chaotic scattering. The shaded disks are infinite potential barriers which scatter a particle entering with fixed velocity and angle, and variable impact parameter b. (a) Scattering geometry showing definition of impact parameter b. Arrow is the incoming trajectory for $b = 3$. (b) Scattering function $\Delta\Theta \equiv \Theta_{in} - \Theta_{out}$ versus b. (c) Expanded view showing fluctuations in $\Delta\Theta(b)$ on all scales. (d) Trapping time versus b showing correlation between chaos in $\Delta\Theta(b)$ and long trapping time. From Smilansky in Giannoni *et al.*, 1991.

2.1.2 2D Scattering Cavities

The classical analog of the experimental system which is the subject of this dissertation is a two-dimensional scattering cavity such as the one shown in Figure 2.2. Particles enter and leave through the straight sections which are referred to as leads. If a single particle were injected into such a cavity, one could study a scattering function just as for the three-disk system. The scattering would be regular or chaotic depending on the shape of the cavity. These single-particle dynamics are not accessible in a cavity formed from an electron gas since many electrons with various initial conditions enter the cavity simultaneously. Therefore we must consider a classical analog with a distribution of injected particles. The quantities of interest are then the probability distributions for the length traveled inside the cavity and the directed area[1] enclosed by the particles before escaping. These distributions have been calculated for cavities of various shapes by numerically integrating the classical equations of motion.[2] There is also an approximate analytical method for finding the distributions which relies on the mixing property of chaotic cavities (Jensen, 1991). This method reveals how the distributions change with lead width for fixed cavity shape, but it cannot be used for regular cavities.

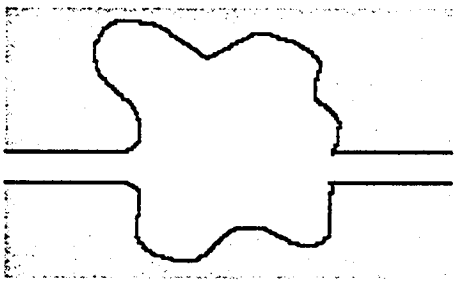

Figure 2.2 A ballistic conductor with a scattering cavity. Particles enter through the left lead, scatter around inside the cavity, and escape through either lead.

---

[1] The directed area of a path in this context is defined in terms of the effective flux that would result if a magnetic field were present: $A \equiv \frac{1}{B}\int_{in}^{out} \vec{\mathbf{A}} \cdot d\vec{\mathbf{l}}$ where $\vec{\mathbf{A}}$ is the vector potential and B is the magnetic field. For closed paths ($in = out$), it is the same as the net geometrical area (taking rotational sense into account).

[2] A large number of particles with fixed velocity and a distribution of initial angles (usually $cos\theta$) is injected into the cavity and the trajectory of each particle is followed as it bounces from the boundaries of the cavity, which are typically combinations of straight lines and circular arcs. When each particle escapes, the path length and the area are recorded to form the two distributions.

From many studies of classical scattering in cavities, it is known that the length and area distributions are qualitatively different for cavities in which the scattering is chaotic as compared to those for which it is regular. When the scattering is chaotic,[3] both distributions are exponential:

$$P(L) \propto e^{-\gamma L} \tag{2.1}$$

$$P(A) \propto e^{-2\pi\alpha|A|} \tag{2.2}$$

Here P is probability, L is length, and A is directed area.[4] The details of the cavity shape affect the parameters γ and α, but the distributions are always exponential as long as the scattering is chaotic. (This implies that there is always a typical scale for these distributions in the chaotic case, and this uniform functional dependence is referred to as "universal".) When the scattering is regular, the distributions are generally power laws:

$$P(L) \propto L^{-m_L} \tag{2.3}$$

$$P(A) \propto |A|^{-m_A} \tag{2.4}$$

The details of the cavity shape affect the exponents m_L and m_A. (Since the distributions have different functional forms for different regular cavities, regular scattering is referred to as "non-universal".)

The distribution of time spent in the cavity, $P(t)$, is also of interest and can be obtained from $P(L)$ by noting that $L = vt$ for ballistic transport. A fourth distribution that is sometimes useful is that for the number of bounces with the cavity walls, $P(N)$. This is related to $P(L)$ through $N = L/L_{typ}$, where L_{typ} is the typical distance travelled between bounces. Thus we have

$$P(t) \propto e^{-\theta t} \tag{2.5}$$

$$P(A) \propto e^{-\eta N} \tag{2.6}$$

for chaotic cavities, and analogous power law distributions for regular cavities.

---

[3] Here we restrict the term "chaotic" to mean only "hyperbolic" chaotic scattering. There are also "nonhyperbolic" systems with a mixture of chaotic and nonchaotic structures in phase space. These systems have chaotic scattering functions but nonexponential distributions of escape times. For details see, for example, Gutzwiller, 1991.

[4] The factor of 2π which appears in equation (2.2) comes from the definition introduced in Jalabert, Baranger, and Stone, 1990 and used in all subsequent work by these authors and most other researchers in this field. It appears somewhat strange since $2\pi\alpha$, and not α itself, is the inverse of the typical area. However, it turns out (see Chapter 3) that the typical magnetic field scale for quantum effects is close to that which produces one flux quantum (h/e) through the area $1/\alpha$, so the definition in equation (2.2) is convenient, although potentially confusing.

The distributions in equations (2.1) and (2.2) are only valid for L and A larger than some minimum length or area. This is not surprising because, as we saw in the three disk system, chaotic behavior in the scattering function is correlated with a long trapping time. For the exponential form to hold, the particles must scatter enough times from the walls that their initial momentum distribution becomes randomized into a uniform distribution (Jensen, 1991). This randomization, also known as mixing, usually occurs faster than the typical escape rate from the cavity, so equations (2.1) and (2.2) will always hold when the exponent, γL or $2\pi\sigma|A|$, is larger than about 1. If the mixing time is much shorter than the escape time, they will also hold for much smaller L and A. (Analogous arguments apply to equations (2.5) and (2.6).) For regular cavities there is a similar limited range of validity which must be determined by examining the results of the simulations for each cavity.

Typical distributions found by numerical simulation for a chaotic stadium cavity and a regular square cavity are shown in Figure 2.3. The exponential and power law forms are clearly followed for large L and A. The fundamental difference between chaotic and regular scattering is reflected in the different forms of these distributions. As discussed in the next section, these distributions influence the scattering properties of the quantum mechanical analog.

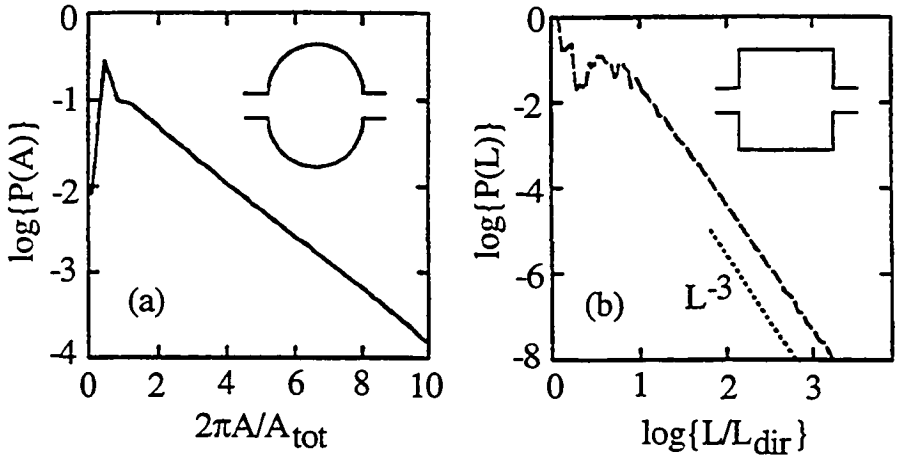

Figure 2.3 Classical distributions of area and length. (a) Area distribution for a stadium cavity with chaotic scattering. Area axis is normalized by the total area between the lead openings, A_{tot}. (b) Length distribution for a square cavity with regular scattering. Length axis is normalized by the direct distance between the lead openings, L_{dir}. Adapted from Baranger, Jalabert, and Stone, 1993b.

2.2 Quantum Chaotic Scattering

Applying the ideas of chaos theory to quantum mechanical systems requires some care. Chaos is characterized by an extreme sensitivity to initial conditions that arises from nonlinearity in the equations of motion. The solutions of the linear Schrödinger equation do not display this property. Furthermore, the uncertainty principle limits the resolution with which quantum phase space can be divided, so the infinitely fine structure of chaotic phase space is not possible, at least for long times. However, the Schrödinger equation is believed to apply to any system regardless of the presence of chaos, and it is expected that there will be some signatures of chaos in quantum systems. The field of "quantum chaos" is concerned with these signatures, *i.e.*, it is the investigation of the features of quantum systems that reflect whether the classical analog is chaotic or regular. This field has become very active in recent years. Reviews of quantum chaos in general are Gutzwiller, 1991 and Giannoni *et al.*, 1991. A review of quantum chaotic scattering by Smilansky can be found in Giannoni *et al.*, 1991.

Quantum scattering is generally described in terms of a scattering matrix S which relates incoming and outgoing channels. A typical element $S_{n,m}(E)$ describes the amplitude for a scatterer with energy E to enter in channel m and leave in channel n. The properties of S for model systems that can have either regular or chaotic classical scattering were investigated by Blumel and Smilansky (Blumel and Smilansky, 1988, 1989, and 1990; Smilansky in Giannoni *et al.*, 1991). Using a semiclassical approximation for S, they calculated various correlation functions which revealed the statistical properties of S. Based on the results, they proposed the hypothesis that when the classical scattering is chaotic, S will have statistical properties that are consistent with S belonging to a particular ensemble of random matrices having the appropriate symmetries. (For a review of random matrices in the context of quantum transport theory, see Stone *et al.*, 1991). Random matrix theory makes several specific predictions about distributions and correlations of the elements of S. Blumel and Smilansky tested their hypothesis using numerical simulations of quantum scattering in their model systems. They found that when the classical scattering was chaotic, S did obey the predictions of random matrix theory.

The semiclassical approximation is the central tool in the analysis of quantum chaotic scattering. A full quantum solution often yields little insight into complex behavior, but a semiclassical analysis can show how the complex quantum

behavior arises from features of the classical dynamics. This is illustrated in the case of the autocorrelation function

$$C_{n,m}(\Delta E) \equiv \left\langle S^*_{n,m}(E+\Delta E) S_{n,m}(E) \right\rangle_E \quad , \tag{2.7}$$

for which Blumel and Smilansky found the following result when the classical scattering is chaotic:

$$C_{n,m}(\Delta E) = \frac{C_{n,m}(0)}{1 - i\Delta E / \hbar\theta}. \tag{2.8}$$

The striking feature of this result is that θ here is the same θ that appears in the classical probability distribution of time spent in the scattering region, equation (2.5). Thus, the autocorrelation function of the quantum S matrix is determined by a property of the chaotic dynamics of the classical analog. As discussed in the next chapter, the conductance of a microstructure at low temperature can be expressed in terms of the elements of S. Equation (2.8) therefore establishes a link between a quantum transport measurement in a ballistic cavity and the chaos in the scattering of classical particles in the same cavity. This link is the fundamental physical idea behind the experiments presented in this dissertation.

3

CHAOTIC SCATTERING AND QUANTUM TRANSPORT IN BALLISTIC CAVITIES

3.1 Introduction

Soon after Blumel and Smilansky's work on the S matrix, the ideas of quantum chaotic scattering were applied to the transmission coefficients of a scattering system (Doron, Smilansky, and Frenkel, 1991) and also directly to the conductance of ballistic cavities (Jalabert, Baranger, and Stone, 1990; Baranger, Jalabert, and Stone, 1993a and 1993b). The results of these studies are several predictions that will be compared with the experimental results described in Chapter 6. Before the predictions themselves are described, some background ideas must be covered. A general reference for quantum transport in semiconductor microstructures is Beenakker and van Houten, 1991.

3.2 Basic Concepts of Ballistic Quantum Transport

The incoming and outgoing channels for scattering in a ballistic cavity are the waveguide modes of the leads. By convention, the x-direction is along the lead and the y-direction is transverse to the lead. The cross-section of each lead is assumed to be an infinite square well of width W, so the wavefuntions are sine functions with the allowed transverse momenta given by

$$k_y = \frac{n\pi}{W} \qquad n = 1,2,3,... \tag{3.1}$$

Electrons can occupy all the modes with $k_y \leq k_F$, so the number of propagating modes is the integer Int$[k_F W/\pi]$. (The subscript F will be dropped from here on, but any k should be understood as the Fermi wavevector.) One electron of each spin can occupy each mode.

In most theoretical studies the electrons are assumed to be phase coherent throughout the scattering process. (See Imry, 1995 for a thorough discussion of the precise meaning of phase coherence in this context.) In experiments there is always a finite phase coherence time τ_ϕ that will destroy quantum interference for sufficiently long paths. Experiments are normally designed so that the typical paths

can be traversed in a time much less than τ_ϕ, and the loss of interference from much longer paths is then neglible. For a chaotic cavity this implies $\tau_\phi >> 1/\theta$. The dephasing time increases as the electron temperature is lowered, so the practical requirement is that the experiments be done at a sufficiently low temperature.

Landauer and Buttiker (Landauer, 1970; Buttiker, 1986) have developed a theory that relates the conductance of a phase coherent structure to a quantum scattering problem. The theory can be applied to structures with any number of leads, but only the form for two leads is needed here. This form is

$$G = 2\frac{e^2}{h} \sum_{n,m=1}^{Int[kW/\pi]} |t_{nm}|^2 \tag{3.2}$$

where t_{nm} is the transmission amplitude from mode m to mode n. Each t_{nm} is an element of the S matrix, so the conductance directly reflects the quantum scattering properties of the structure.

The starting point for the calculations of Jalabert *et al.* is the following expression for the transmission amplitude (Baranger and Stone, 1989):

$$t_{nm} = -i\hbar(v_n v_m)^{1/2} \int_{left} dy \int_{right} dy' \, \psi_n^*(y') G(y', y, E) \psi_m(y) \tag{3.3}$$

The interpretation of this expression is quite intuitive: the electron arrives at y on the left side of the cavity in mode m, propagates inside the cavity through the Green function G, and leaves at y' on the right side of the cavity in mode n. All of this occurs at energy E (the Fermi energy), and v_n and v_m are the longitudinal (x-direction) velocities of the modes.

3.3 Conductance Fluctuations

The quantum conductance of a ballistic cavity can be computed as described in Baranger, Jalabert, and Stone, 1993b and references therein. The method is essentially a discrete version of the relation in equation (3.3). The Green function for a spatially discrete Hamiltonian inside the cavity is found recursively and then projected discretely onto the modes in the leads. The classical conductance can be found by injecting a distribution of particles at one lead and following their ballistic trajectories to obtain the transmission probability (Beenakker and van Houten, 1989 and 1990; Baranger, DiVincenzo, Jalabert, and Stone, 1991). Numerically computed results for $G(k)$ and $G(B)$ are shown in Figure 3.1. The most obvious feature is the large fluctuations ($\delta G_{rms} \sim e^2/h$) in the quantum conductance over a range of B or k where the classical conductance is completely smooth. This

indicates the fluctuations are a quantum interference effect. In contrast to the case of conductance fluctuations in diffusive systems, where complex structure in $G(k)$ and $G(B)$ arises from the disorder of random impurities, the fluctuations of a ballistic cavity arise from the complex classical dynamics of a relatively simple shape with no disorder.

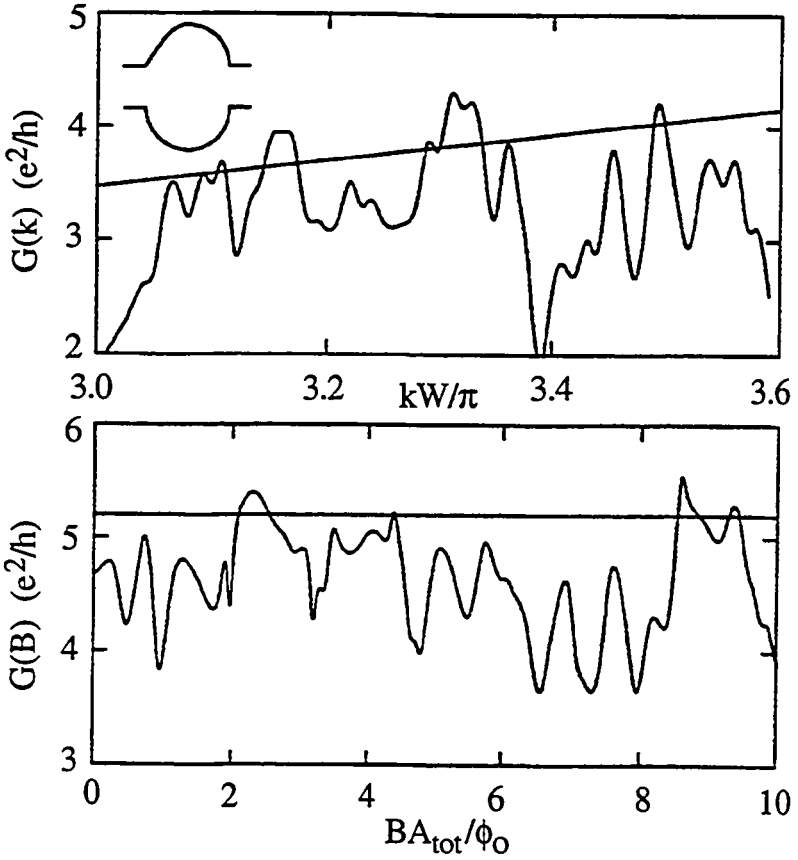

Figure 3.1 Numerical results for $G(k)$ and $G(B)$ of an asymmetrized stadium cavity. Straight lines are classical results, fluctuating curves are quantum results. Adapted from Baranger, Jalabert, and Stone, 1993b (their spinless transmission T was multiplied by $2e^2/h$ to obtain G).

As mentioned in Chapter 2, a semiclassical analysis can reveal the link between the complex behavior of Figure 3.1 and the underlying classical dynamics. The analysis is based on equation (3.3) with a semiclassical approximation for G. G is expressed as a sum over classical paths connecting the left and right leads of the cavity (see Baranger, Jalabert, and Stone, 1993b for more details):

$$G(y',y,E) \propto \sum_{p(y,y')} \sqrt{D_p} \exp\left[\frac{i}{\hbar} S_p(y',y,E) - i\frac{\pi}{2}\mu_p\right] \qquad (3.4)$$

Each term in the sum has a classical amplitude D_p and a phase given by the action integral S_p along path p. μ_p is the Maslov index for path p (see Giannoni *et al.*, 1991). Thus the electron is treated as a classical particle with a phase that allows for interference between different paths. The goal of the analysis is not to describe the particular sequence of bumps that appears in $G(k)$ or $G(B)$, but to describe the statistical properties of the bumps. Thus the quantities of interest are the autocorrelation functions of the conductance, $C(\Delta k) \equiv \langle \delta G(B,k+\Delta k)\delta G(B,k)\rangle_k$ and $C(\Delta B) \equiv \langle \delta G(B+\Delta B,k)\delta G(B,k)\rangle_B$, where $\delta G \equiv G - \langle G\rangle$ is the deviation of G from the mean. The semiclassical analysis of these quantities is described at length in Baranger, Jalabert, and Stone, 1993b. A key assumption is that the complex scattering inside the cavity destroys any correlation between the incoming and outgoing angles of the classical trajectories. Classical simulations show this assumption is justified for *chaotic* cavities. The results of the analysis for chaotic cavities are:

$$C(\Delta k) = \frac{C(0)}{1+(\Delta k / \gamma)^2} \tag{3.5}$$

$$C(\Delta B) = \frac{C(0)}{\left[1+(\Delta B / \phi_0\alpha)^2\right]^2} \tag{3.6}$$

where ϕ_0 is the flux quantum h/e. As in Chapter 2, these quantum correlation functions are determined by the parameters γ and α from the classical probability distributions in equations (2.1) and (2.2). It is conventional to define the characteristic scale of the fluctuations as the halfwidth of the autocorrelation function. This convention is followed for $C(\Delta k)$, giving $\Delta k_c = \gamma$. The halfwidth of $C(\Delta B)$ is $\sqrt{\sqrt{2}-1}(\phi_0\alpha) \approx 0.64\phi_0\alpha$, but the characteristic field is usually taken to be simply $\Delta B_c = \phi_0\alpha$. It is interesting to note that the halfwidth of $C(\Delta B)$ is only about one tenth of the field that produces ϕ_0 through the "typical" area enclosed, $1/2\pi\alpha$. This indicates the importance of the longer trajectories in the distribution.

For comparison with experiments, or with numerical quantum calculations, it is more convenient to work with the Fourier Transform of $C(\Delta k)$ or $C(\Delta B)$, which is simply the power spectrum (Fourier Transform magnitude squared) of $G(k)$ or $G(B)$.[5] These power spectra have the forms

---

[5] More precisely, the identity is:

$$S_x(f) \equiv \left|\int_{-\infty}^{+\infty} dx G(x) e^{i2\pi fx}\right|^2 = \int_{-\infty}^{+\infty} d\Delta x C(\Delta x) e^{i2\pi f\Delta x} \qquad x = k \text{ or } B;\ f = \frac{1}{\Delta k} \text{ or } \frac{1}{\Delta B}$$

$$S_k(f) = S_k(0)e^{-2\pi\gamma f} \qquad f = \frac{1}{\Delta k} \tag{3.7}$$

$$S_B(f) = S_B(0)\left(1 + 2\pi\phi_0\alpha f\right)e^{-2\pi\phi_0\alpha f} \qquad f = \frac{1}{\Delta B} \tag{3.8}$$

The frequencies can be normalized so they reflect the connection to length and area more directly:

$$S_k(\Lambda) = S_k(0)e^{-\gamma\Lambda} \qquad \Lambda = \frac{2\pi}{\Delta k}$$

$$S_B(\Omega) = S_B(0)(1 + 2\pi\alpha\Omega)e^{-2\pi\alpha\Omega} \qquad \Omega = \frac{\phi_0}{\Delta B}$$

With these definitions, Λ is the change in electron wavelength when the wavevector changes by Δk, and Ω is the area through which the flux changes by one quantum when the field changes by ΔB.

The test of the semiclassical results proceeds as follows. $G(k)$ and $G(B)$ are experimentally measured or numerically computed for a given cavity. Their power spectra are computed and then fit using the form in equation (3.7) or (3.8), with $S_k(0)$ and γ or $S_B(0)$ and α as fitting parameters. This determines the quantum values of γ and α for the cavity. The classical scattering is then numerically simulated to generate $P(L)$ and $P(A)$, which are fit using the exponential forms in equations (2.1) and (2.2) to determine the classical values of γ and α for the cavity. The semiclassical approximation is correct to the extent that the two determinations of γ and α give the same result. Jalabert, Baranger, and Stone, 1990 have done numerical tests and found good agreement for a variety of cavity shapes and over a wide range of the lead width W for a fixed shape. The experimental tests will be described in Chapter 6.

The semiclassical analysis of *regular* cavities has also been examined by Baranger, Jalabert, and Stone, 1993b. The assumption of uncorrelated incoming and outgoing angles is not valid for regular cavities, and this fact has made an analytical solution impossible to date. However, the power spectra can be calculated numerically, and they are found to be clearly different from those of chaotic cavities, as shown in Figure 3.2 for S_k. The chaotic cavity follows the exponential form of equation (3.7) while the regular cavity shows a much slower falloff at high frequencies. This difference can be traced to the different classical length distributions for the two cavities. The power spectrum of $G(B)$ is also different for regular and chaotic cavities, although the link to the classical area distributions is sometimes less clear. *In general, the nonexponential classical distributions of regular cavities result in power spectra that fall off more slowly than*

those of chaotic cavities, which are always exponential (S_k) or nearly exponential (S_B). Distinguishing between the two types of behavior requires several decades of sensitivity in the power spectra.

The discussion in Baranger, Jalabert, and Stone, 1993b covers the approximations and assumptions used in the semiclassical analysis in detail. Only the two most important limitations from an experimental viewpoint will be discussed here. The first restriction on the analysis is that the electron cyclotron radius must be larger than the cavity size. There is no precise cutoff, but as the classical trajectories become more curved, the distribution $P(A)$ becomes asymmetric (positive directed areas become more probable than negative ones) and the correlation function (3.6) can no longer be characterized by a single value of α. Since the range of k even in a gated sample is limited, this effectively restricts the study of the fluctuations to small values of B. The second major restriction is that the number of modes, kW/π, must be much greater than 1. This is not surprising since the nature of any semiclassical approximation is to ignore the "diffraction" effects that dominate in the limit of a single mode.

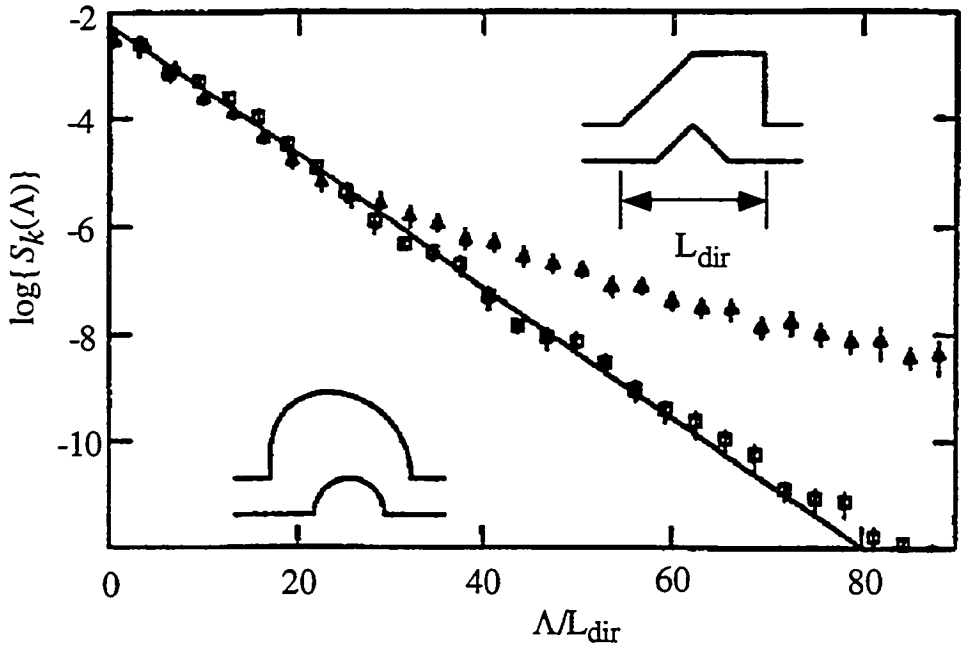

Figure 3.2 Power spectrum of $G(k)$ for a chaotic cavity (bottom shape, square points) and for a regular cavity (top shape, triangle points). Straight line shows the expected exponential form for the chaotic cavity. Frequency is normalized using the direct distance between the leads. $kW/\pi = 33$. From Baranger, Jalabert, and Stone, 1993b.

3.4 Weak Localization

In addition to the fluctuations in Figure 3.1, there is also a quantum interference effect on the average conductance, illustrated in Figure 3.3. In the upper panel, the solid curve is $G(k,B = 0)$ and the dashed curve is the same thing after smoothing, which is equivalent to an average over energy. The dotted curve is

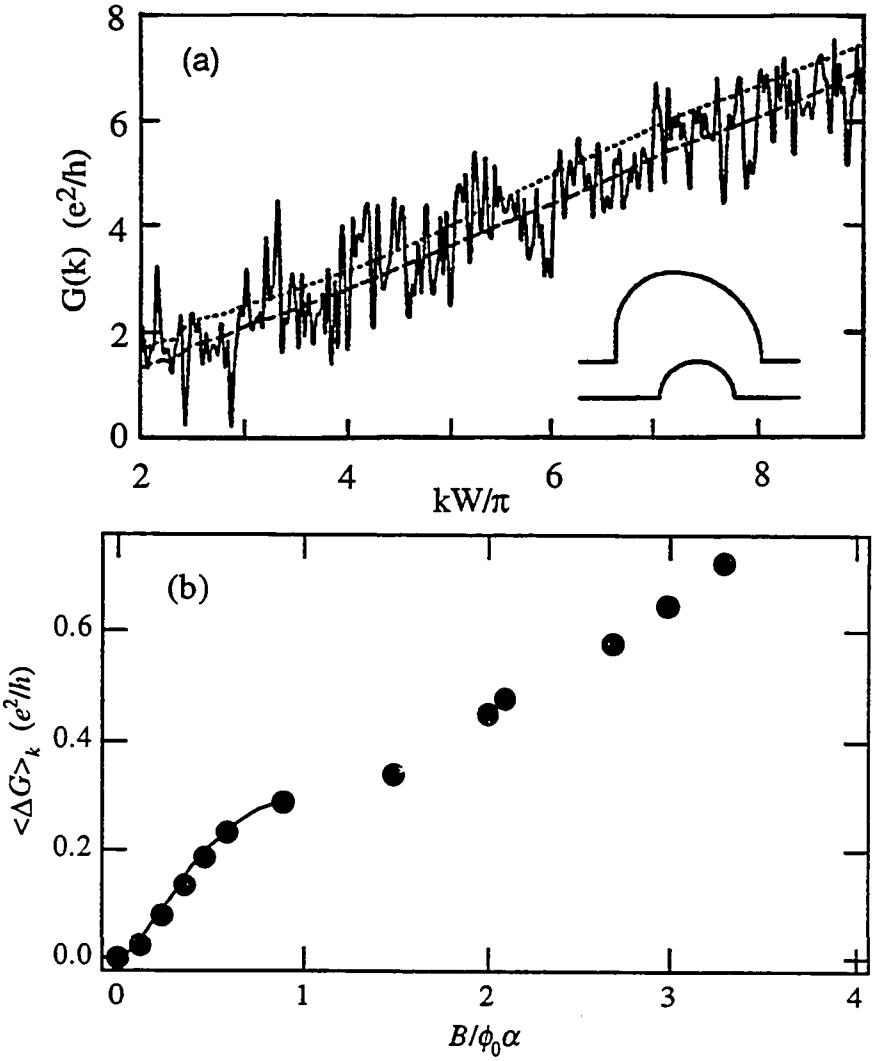

Figure 3.3 Numerically calculated quantum $G(k)$ showing the effect of a magnetic field B on the average conductance. (a) Solid line is $G(k)$ at $B = 0$. Dashed line is smoothed $G(k)$ at $B = 0$. Dotted line is smoothed $G(k)$ at $B = 2\phi_0/A_{tot}$. (b) Average $G(B)$ over the range $kW/\pi \in [4,11]$. Curve is a Lorentzian fit to the points for $B < \phi_0\alpha$. Adapted from Baranger, Jalabert, and Stone, 1993b (their average change in spinless transmission was multiplied by $2e^2/h$ to obtain $\langle \Delta G(B) \rangle$). Error bars are approximately the same size as point markers.

$G(k, B = 2\phi_0 / A_{tot})$ after smoothing, where A_{tot} is the total area of the cavity. The presence of two flux quanta through the cavity produces a noticeable increase in the average conductance. In the lower panel, the average conductance change $\langle \Delta G(B) \rangle \equiv \langle G(k,B) - G(k,0) \rangle_k$, is shown as a function of B for the same cavity. The average effect is an increase in G by an amount of order e^2/h. This behavior is very similar to the weak localization effect found in disordered conductors where the electron transport is diffusive. As in the diffusive regime, the effect is related to the breaking of time-reversal symmetry by the magnetic field.

A semiclassical analysis of the weak localization has been carried out (Baranger, Jalabert, and Stone, 1993a and 1993b). For *chaotic* cavities, the result is that $\langle \Delta G(B) \rangle$ is predicted to have the form of an inverted Lorentzian:

$$\langle \Delta G(B) \rangle \propto \left[1 - \frac{1}{1 + (2B / \phi_0 \alpha)^2} \right] \tag{3.9}$$

The width of $\langle \Delta G(B) \rangle$ is determined by the parameter α from the classical area distribution in equation (2.2). The lower panel of Figure 3.3 shows a fit of equation (3.9) to the numerical points for small B. For small B the fit is very good, but for $B > 2\phi_0\alpha$ there are deviations from equation (3.9). The behavior at $B > 2\phi_0\alpha$ depends on the shape of the cavity, but all chaotic cavities saturate or have a large change in slope at $B \approx \phi_0\alpha$. Thus they can be fit quite well with equation (3.9).

The semiclassical analysis of weak localization in *regular* cavities does not lead to an analytical solution because, just as for the fluctuations, the assumption of uncorrelated incoming and outgoing angles is not valid. Numerical calculations for $\langle \Delta G(B) \rangle$ in two polygonal cavities are shown in Figure 3.4. $\langle \Delta G \rangle$ is generally linear in B from very near $B = 0$ to well beyond $B = \phi_0\alpha$. Baranger, Jalabert, and Stone, 1993b, discuss how this linear behavior appears to arise from flux cancellation in polygonal cavities with parallel sides. These authors have also found more general arguments for the existence of linear weak localization in any cavity with a power law distribution of areas (A.D. Stone, private communication, 1994). Thus the general prediction is that *weak localization in regular cavities is linear well beyond $B = \phi_0\alpha$, in contrast to the Lorentzian shape with halfwidth $\phi_0\alpha/2$ found for chaotic cavities.* This prediction will be compared with experimental results in Chapter 6.

The limitations on the semiclassical analysis mentioned at the end of the previous section also apply to the weak localization results.

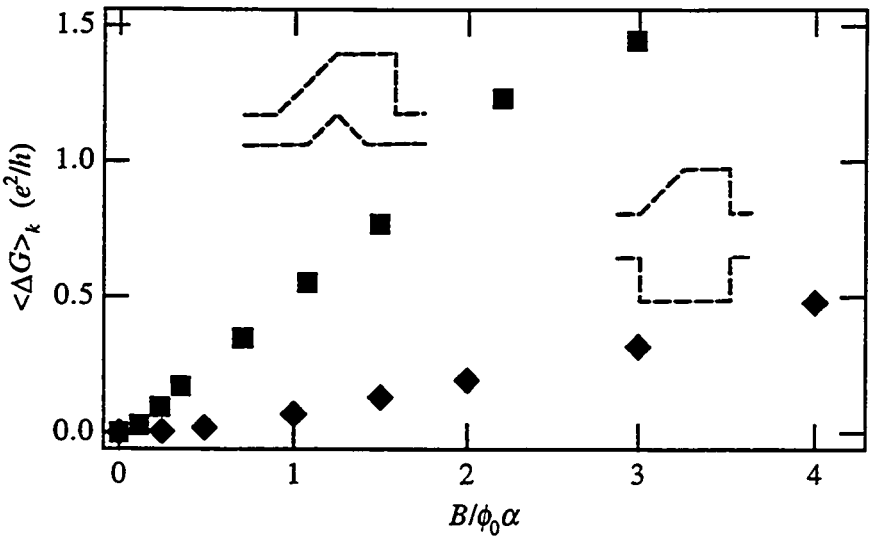

Figure 3.4 Weak localization for two regular cavities: Half-asymmetric polygon (squares) and Full-asymmetric polygon (diamonds). From Baranger, Jalabert, and Stone, 1993b (their average change in spinless transmission was multiplied by $2e^2/h$ to obtain $\langle \Delta G(B) \rangle$). Error bars are approximately the same size as point markers.

3.5 Random Matrix Theory Analysis

In addition to the "microscopic" approaches of exact quantum calculation or semiclassical approximation, conductance fluctuations and weak localization can also be studied using the "macroscopic" approach of random matrix theory. This was done for the case of diffusive transport (see Stone *et al.*, 1991 for a review) and it has also been done very recently for ballistic transport in chaotic cavities (Baranger and Mello, 1994a). Baranger and Mello considered chaotic cavities with no direct paths between the leads, for which they could assume S is described by the "circular ensembles" of random matrix theory. (S is a member of the Circular Orthogonal Ensemble for $B = 0$, and a member of the Circular Unitary Ensemble when B is large enough to break time reversal symmetry.) They derived the size of the (ensemble average) weak localization effect and the variance of the fluctuations in $G(k)$ or $G(B)$ for any number of modes in the leads. Their results for the limit $kW/\pi \rightarrow \infty$ are summarized in Table 3.1.[6] Baranger and Mello compared these

[6] The published results for spinless particles were multiplied by 2 in the case of weak localization and by 4 in the case of the variance of the fluctuations to account for spin.

predictions with numerical results for a typical chaotic cavity and found good agreement. This work showed that the effects are "universal" in the sense that they do not depend on the details of the cavity shape or size or on k as long as $kW/\pi >> 1$. Regular scattering cavities are not necessarily expected to show the same universal behavior.

	Weak Localization Amplitude	Conductance Fluctuation RMS Amplitude
$B = 0$	$\frac{1}{2}\frac{e^2}{h}$	$\frac{1}{\sqrt{2}}\frac{e^2}{h}$
$B \geq \phi_0 \alpha$	0	$\frac{1}{2}\frac{e^2}{h}$

Table 3.1 Random matrix theory predictions for quantum interference effects in chaotic cavities in the limit $kW/\pi \rightarrow \infty$.

Very recently, the effects of a finite τ_ϕ have been included in the random matrix theory analysis by Baranger and Mello, 1994b. They have derived predictions for the size of the WL and the conductance fluctuations in cavities with any kW/π and any number N_ϕ of effective channels for "escape" through phase breaking. The result most relevant for the experiments discussed here is that the "universal" predictions shown in Table 3.1 are only valid when $N_\phi << kW/\pi$. In other words, if the electrons typically escape through the geometrical leads before being "lost" to phase breaking, then the size of the quantum interference effects is unaffected. Experiments designed to test the predictions in the regime of $N_\phi \geq kW/\pi$ have recently been reported (Clarke *et al.*, 1994).

3.6 Experimental Requirements

Based on the theoretical work described in the previous sections, the desired characteristics of an experimental system for the study of chaotic scattering can now be listed.

- It must be possible to make cavities of a variety of shapes and sizes. These cavities should come as close as possible to the ideal of scattering only from the boundaries, and the boundaries should be as free of disorder as possible.

- It must be possible to vary the magnetic field and/or the Fermi wavevector of the electrons without affecting the cavity shape.
- The cavities should be studied in the semiclassical regime of large kW/π, and at small B where the electron trajectories are approximately straight.
- The cavities must be cooled to a temperature low enough that the electrons remain phase coherent over the length of the typical trajectories involved.

The following two chapters describe the fabrication of samples and the construction of a low temperature measurement system designed to satisfy these criteria.

4

FABRICATION OF BALLISTIC CAVITIES FROM GaAs/AlGaAs HETEROSTRUCTURES

4.1 Basic Properties of the Heterostructure

A cross-sectional view of a typical high mobility GaAs/$Al_xGa_{1-x}As$ heterostructure is shown in Figure 4.1. The highest quality heterostructures are grown by molecular beam epitaxy (MBE) in ultrahigh vacuum chambers, starting from a substrate wafer of semi-insulating GaAs. A thick layer of undoped GaAs is grown first, followed by a "spacer layer" of undoped AlGaAs, then a layer of AlGaAs doped with Si, and finally a thin cap layer of GaAs to protect the reactive AlGaAs layers. The Al fraction is typically near x = 0.30.

100-200 Å	NID GaAs
~ 500 Å	n-type $Al_xGa_{1-x}As$ ($\approx$ 1-3 x 10^{18} Si/cm^3)
100-400 Å	NID $Al_xGa_{1-x}As$
1.0 μm	NID GaAs
	Semi-insulating GaAs substrate

Figure 4.1 Typical layer structure of a high mobility GaAs/$Al_xGa_{1-x}As$ heterostructure. NID layers are not intentionally doped.

The reason for creating such a structure can be seen by examining the energy bands shown in Figure 4.2. The discontinuity in the conduction band at the GaAs/AlGaAs interface creates a narrow potential well with discrete energy states that define the bottoms of 2D subbands. The n-type dopants in the AlGaAs provide electrons which fill up these subbands. With the appropriate doping level and spacer layer thickness, the lowest subband alone can be populated, as shown by the Fermi level in the figure. Thus a properly designed heterostructure supports a strictly two-dimensional electron gas (2DEG), with all electrons having the same z wavefunction and being free to move parallel to the surface of the wafer.

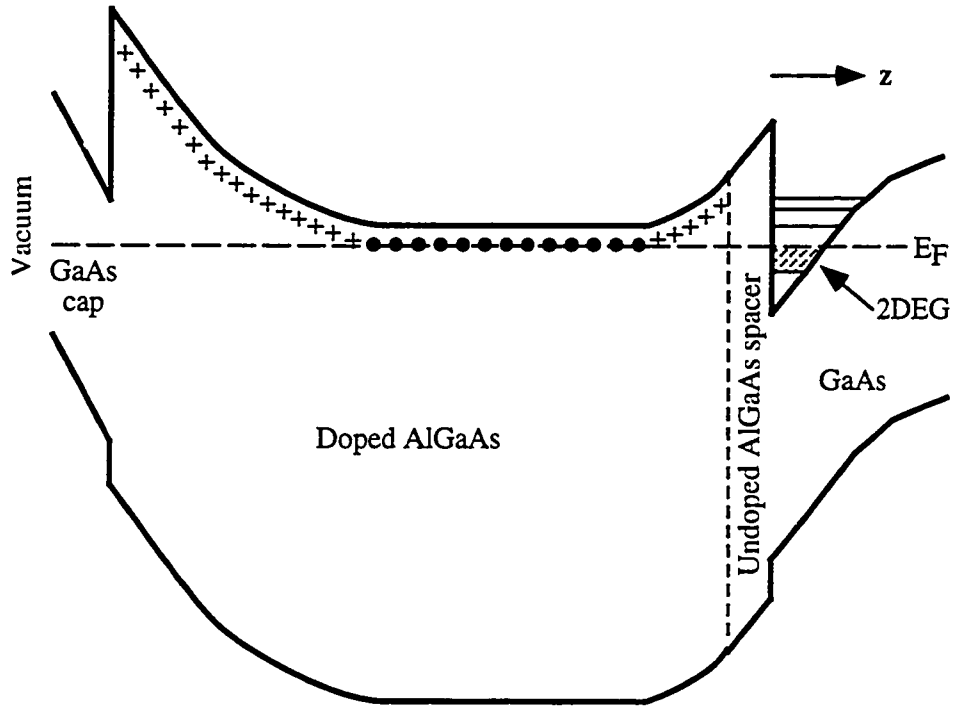

Figure 4.2 Energy bands of a typical GaAs/AlGaAs heterostructure. Donors are indicated by + (ionized) or • (un-ionized) Horizontal lines in the triangular well at right are the discrete states which define the bottoms of the 2D subbands.

The truly 2D nature of the electron gas itself already makes this system significantly different from a thin metal film. However, the primary reason for the great interest in GaAs/AlGaAs for electron transport studies is the fact that defect scattering of electrons travelling in the 2D layer can be extremely weak. This is the result of the undoped AlGaAs spacer layer that separates the disordered region of ionized donors from the 2DEG. The electron mean free path inferred from

conductivity measurements can be 10 μm for material grown in a good MBE chamber, and values in excess of 100 μm have been realized at a few exceptional facilities.[7] Since it is fairly easy to confine the 2DEG to size scales of a few μm, the regime of electron transport on length scales shorter than the mean free path can easily be reached. However, the mean free path, which measures the distance over which electrons lose their initial forward momentum, does not tell the whole story. The potential energy variations seen by the 2DEG are shallow and rapid, resulting in many small-angle scattering events (typically 10 degrees per event) on a length scale smaller than the mean free path. The smaller scattering length over which electrons remain in exactly the same momentum state can be measured using the Shubnikov-de Haas effect, and it is typically found to be less than 1/10th of the mean free path (see Coleridge, 1991). When small-angle scattering is taken into account, it is clear that studies of electron transport with negligible defect scattering require structures of total size near 1 μm. This makes the fabrication more challenging.

For chaotic scattering studies it is also important to be able to change the electron density of the 2DEG. This can be done conveniently by placing a metal gate on top of the GaAs cap layer and applying a voltage between the gate and the 2DEG. At room temperature the charge on the gate is compensated by the large density of surface states and the gate does not affect the 2DEG. At temperatures below about 100 K, the surface states and the un-ionized donors in the AlGaAs are frozen in place and the 2DEG density can be increased or decreased using the gate.

The heterostructures used in this work were obtained from two MBE growers. Dr. Bob Sacks, formerly of United Technologies Research Center in East Hartford, CT and now at Ohio State University, grew one of the wafers used in this work. Ms. Haddas Shtrikman of the Weizmann Institute of Science in Rehovot, Israel grew the other one. Detailed descriptions of these heterostructures and their bulk transport properties are given in Appendix A.

4.2 Large Scale Fabrication

In order to measure a micron-sized cavity it must be connected to the macroscopic world of electronic instruments. This requires several intermediate

---

[7] When the spacer exceeds a certain thickness, the defect scattering is limited by unintentional impurities in the GaAs, rather than by the donors. Thus the scattering strength depends on the cleanliness of the MBE chamber, and the best results are achieved only after many months of continuous operation at ultrahigh vacuum.

structures to make the transition from the coaxial connectors on the instruments at room temperature to the submicron leads that inject electrons into the cavity at a temperature of order 0.1 K. The connections from the instruments to the header that holds the GaAs chip will be discussed in Chapter 5. The fabrication of the cavities themselves is discussed in Section 4.3. The large structures on the sample chip and the wire bonding process are described in this section.

The layout of the large scale structures is shown in Figures 4.3 and 4.4. The GaAs wafer was diced into 3.5 mm by 3.5 mm chips. The 2DEG was etched away everywhere except inside a 100 μm by 100 μm "mesa" at the center of the chip. Ohmic contacts were placed along the edges of the mesa, overlapping small tabs of mesa that protruded from the central square. The ohmic contacts were then connected by metal film leads to 300 μm by 300 μm pads to which wire bonds could be attached. Alignment marks for electron beam lithography were placed at the center of the mesa.

The large scale fabrication was done using conventional photolithography, wet chemical etching, and metal liftoff processes. An annotated recipe for each step can be found in Appendix B. All of these fabrication steps were done in the Microfabrication Facility at Yale. The masks used initially were emulsion on glass plates made at Yale. Later a set of chromium on quartz plates was made at the National Nanofabrication Facility at Cornell (see Appendix C). With careful attention to many details and lots of practice, a yield of about 80% was eventually achieved for the large scale fabrication process. This provided a fairly reliable supply of samples for the microstucture fabrication attempts, which had a much lower yield.

Completed samples were mounted in headers that could be plugged into sockets wired to the low temperature apparatus. When the ion exposure samples were made, the header was a cylinder of Delrin with 8 pins around the perimeter and a Cu stub in the center, a custom design made by the Yale machine shop.[8] The samples were attached to the Cu stub with silver paint.[9] A ball-type wire bonder[10] was used to attach 1 mil Au wires to the large pads on the sample, and the other

---

[8] The custom headers have the advantage that they can be made completely nonmagnetic if the materials in the pins are chosen carefully, e.g. pure Cu.

[9] The silver paint was type SC-12 from the Micro-circuits Company. It was dried under a 100 W light bulb for 30 to 60 minutes.

[10] Kulicke and Soffa Model 472.

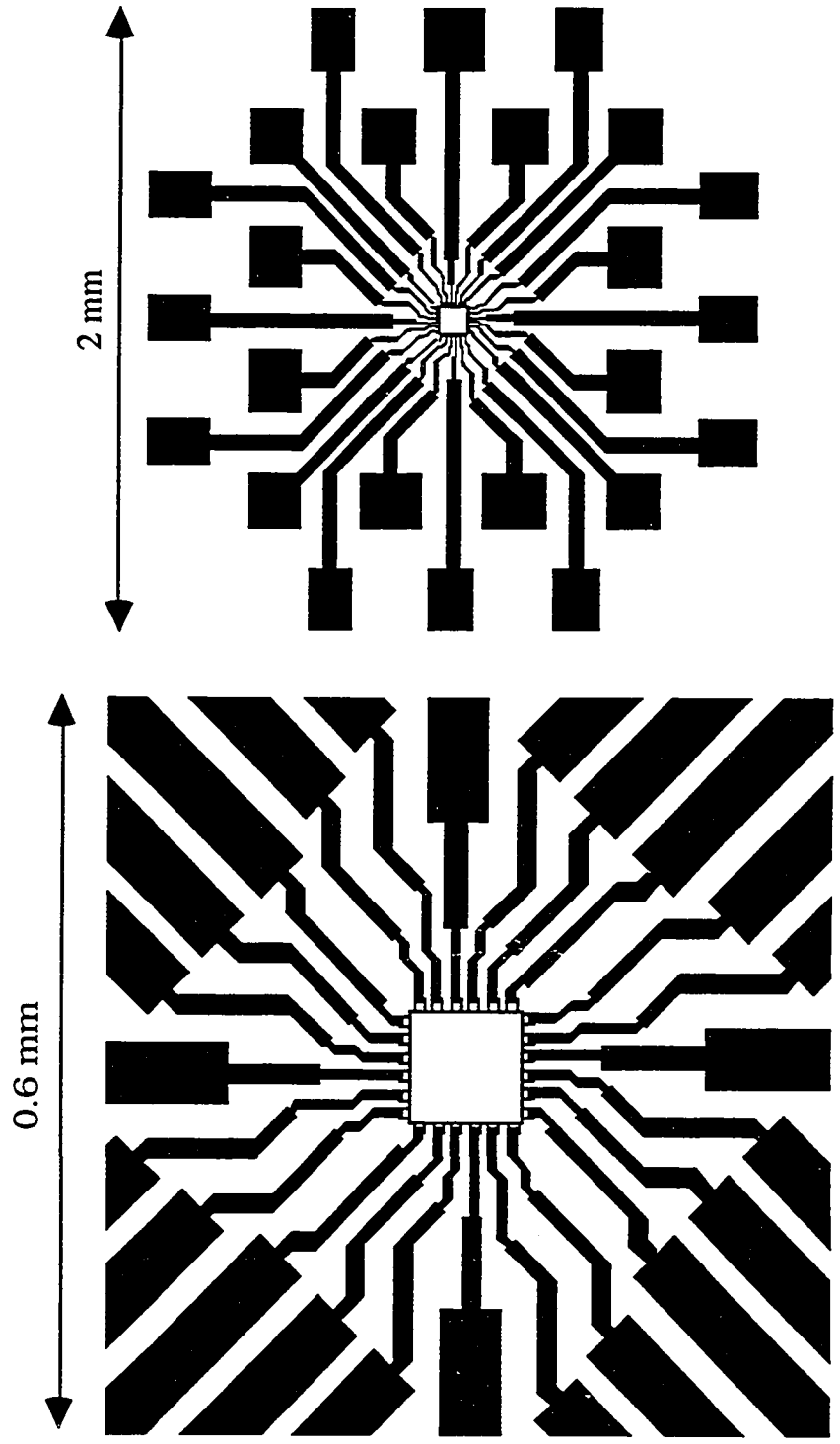

Figure 4.3 Metal pads with leads converging on the 100 μm square mesa of 2DEG. Top shows the entire pattern of the masks made at NNF. Bottom shows an enlarged view of the center. See Figure 4.4 for details of the central square.

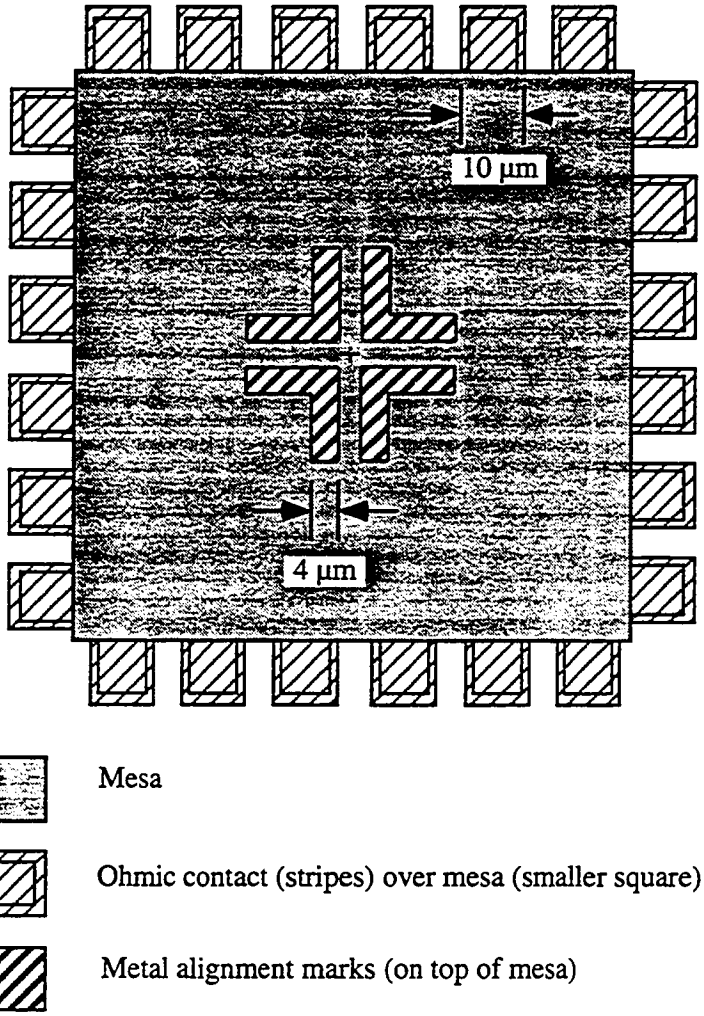

Figure 4.4 Enlarged view of the structures at the center of the patterns in Figure 4.3.

ends of the wires were attached to the pins with silver paint. The Delrin headers would not tolerate high temperature and at room temperature the bonding step was very unreliable, even with a thick layer of Au placed on top of the annealed ohmic contacts. Often a blob of In would be placed on each pad and the Au wire would simply be smashed into it. When the shallow etch samples were made, a custom header from the Jade Corporation with 24 pins was used.[11] The samples were

[11] The Jade headers have a very compact square design with 24 leads occupying only slightly more space than the 8 leads of the custom header. However, a commercial source for a matching square of sockets was not found. Individual sockets were purchased from Advanced Interconnections (part # 1530 TG), and

attached to the header with silver paint. The header was clamped in a stage heated to 200 C and wire bonds were made to both the sample and the header using a wedge-type bonder[12] with 1 mil Au wire. The wedge bonder was very reliable, with typically 23 out of 24 bonds successful on the first try.

4.3 Microstructure Fabrication

The fabrication of submicron structures nearly always involves electron beam lithography (EBL). This is a powerful and flexible method of defining small patterns which has become a standard tool of experimental mesoscopic physics. A carefully characterized and maintained EBL system will produce small patterns for metal liftoff quite reliably. Good metal liftoff is essentially all that is needed to produce microstructures by the common "split-gate" technique. The metal is patterned with gaps of the desired shapes and when a large negative bias is applied to the metal with respect to the 2DEG, the 2DEG is confined within the gaps. The disadvantage of the split-gate method is that the electron density cannot be varied without affecting the size of the structure. For this reason, two other methods were used to create small cavities and leads for the chaotic scattering studies: low energy ion exposure and shallow wet chemical etching. Both of these methods allow the electron density to be changed independent of cavity size and shape. (This advantage is possible because the metal gate which varies the density is not involved in the confinement of the 2DEG to the cavities, which is achieved by the ion exposure or the etching. The gate is positioned directly over the cavity and smaller gate voltages are needed than with the split-gate method.) Both methods require an additional, very critical step beyond metal liftoff which proved difficult to master, but when executed successfully they did produce samples with the tunable density necessary for this work.

4.3.1 Low Energy Ion Exposure

The use of low energy ions to destroy the conductivity of selected regions of a GaAs 2DEG was developed by Scherer and Roukes (Scherer *et al.*, 1987; Cheeks *et al.*, 1988; Scherer and Roukes, 1989). The technique involves patterning a mask on the surface of the sample and exposing it to a broad beam of

---

plastic strips of sockets with the correct spacing were purchased from Amp (part # 104192-8). The Jade headers are slightly magnetic.

[12] Mech-El Industries Model 990.

ions with an energy of 100 to 200 eV. At a sufficient ion dose, the conductivity is destroyed in the unmasked regions, thus confining the 2DEG to the shape of the mask. The first reported work combined Ar ions with Cl_2 gas in a chemically assisted etching process, but it was later found that ions alone were just as effective. Several ion species have been used, including He, Ne, Ar and Xe. Various masking materials have been used, including photoresist and PMMA, but the use of a metal mask has the advantage that it results in a gate which is self-aligned to the 2DEG structures after the exposure.

Scherer *et al.* used the technique to fabricate wires with a structural width of 75 nm which were well-behaved at low temperature. Their work concentrated on empirical studies to determine the optimum parameters and measurements of the characteristics of submicron structures made with the technique. They found that their best narrow wires had several properties which make the technique attractive even though it is more difficult than the split-gate method. First, the mobility and electron density in the 75 nm wires were essentially the same as the bulk values measured in a large sample from the same wafer. Thus the ions did not degrade the properties of the 2DEG under the mask. Second, the conducting width of the wires differed from the mask width by less than 50 nm, which allows small features in the mask/gate pattern to be transferred to the 2DEG with minimal rounding. Third, the conducting width was independent of the voltage on the mask/gate over a significant range. All of these properties make this techniqe an excellent candidate for studies of ballistic scattering, and the third one offers an important advantage over the split-gate method for the chaotic scattering work.

The mechanism by which the ions destroy the 2DEG is not yet understood in detail. Scherer *et al.* noted that the ions removed only a very small amount of the GaAs cap layer, and they found that removing a similar amount of material by wet chemical etching had no effect on the 2DEG. This indicates that the ions cause some electrical *damage* in the heterostructure which affects the 2DEG, even though the ions are not energetic enough to penetrate beyond the cap layer. Later studies by Li *et al.*, 1993 have been interpreted in terms of reduced screening effects related only to removal of material at the surface and do not indicate that the ions act differently from other methods of etching. It is likely, however, that the combination of material removal and some unspecified ion damage is more effective at destroying the 2DEG than is material removal alone.

The ion exposure process used at Yale was as follows. After completion of the large scale fabrication, a metal mask in the shape of the desired cavity and leads

was patterned by electron beam lithography and liftoff of Ti/Au. The sample was then wire bonded to an 8 pin header and mounted in an ion gun vacuum chamber with leads attached for *in situ* monitoring of the sample resistance.[13] The resistance of a narrow wire in the pattern, which had a well-defined number of squares after exposure, was measured with a digital multimeter using a four-wire configuration. The Kaufman-type ion gun was operated with Xe gas and an accelerating voltage of 200 V. Resistance measurements were only possible when the shutter over the ion gun was closed, so we exposed the sample for a few minutes, closed the shutter and recorded the sample resistance, and repeated this process until we observed an increase in the sample resistance. The process is complicated by the fact that a narrow wire that is fully confined at room temperature may not conduct at lower temperature. With several trials using identical sample patterns, we were able to determine the resistance the wire should have in the vacuum chamber at room temperature so that the small structures were properly defined at liquid He temperature and below.

It was found that the confinement decreased over a period of several days at room temperature. This made it necessary to cool the samples to $T \approx 77$ K within a few hours after the ion exposure and store them in a liquid nitrogen dewar between measurements. It also allowed more than one chance at the correct ion dose for each sample. Samples which appeared overexposed at low temperature were left at room temperature for several days and then exposed again. Samples which appeared underexposed were also returned to the vacuum chamber for an additional ion dose. The number of successful samples was too small to determine whether repeated dosing and room temperature "annealing" had any adverse effects on the samples.

Several tens of samples were attempted, but only one sample fabricated by low energy ion exposure is discussed here: 161L5. Very few other samples were worth testing at low temperature, and only two were worth measuring carefully. Most samples did not make it through all of the large scale fabrication steps, for various reasons including lack of skill on the part of the fabricators, who were still learning their trade. There were also problems involving several aspects of the final fabrication steps that are worth mentioning. The EBL at the time was done on a modified ISI SS-60 scanning electron microscope system (Rooks, 1987) which

---

[13] Simply monitoring the ion dose is not sufficient because small changes in sample geometry and ion beam conditions can make the optimum dose vary significantly. This was also found by Scherer and Roukes.

was suffering from a lack of agressive maintainance and did not consistently produce good mask/gate patterns. A few samples were destroyed in the vacuum chamber by instabilities in the ion gun, especially early on when we attempted to use energies below 200 eV. Two samples were destroyed by static discharges during mounting in the vacuum chamber or on the cryostat, before we started wrapping the header pins with a piece of solder during handling. These problems were all solved or in the process of being solved when 161L5 was completed. By the time another sample was needed (after a year of installing and testing the dilution refrigerator and measuring 161L5), the shallow etch method of fabrication looked more promising, so the ion exposure method was abandoned.

Figure 4.5 shows the gate/mask pattern of sample 161L5. Details of the fabrication of this sample are given in Appendix D. Measurements of this sample will be presented in Chapter 6.

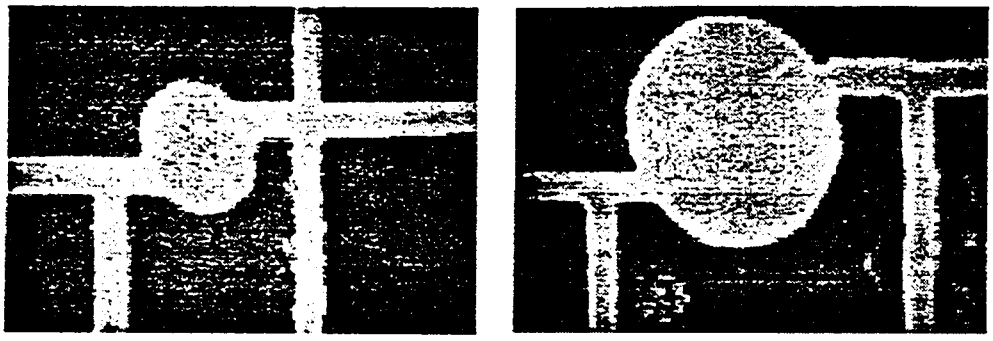

Figure 4.5 Scanning electron microscope images of the Small and Large Stadia of sample 161L5 before ion exposure. The darker regions are the GaAs surface and the lighter regions are the metal mask/gate which is self-aligned to the conducting regions after ion exposure. The black line superimposed on each image is approximately 1 μm.

4.3.2 Shallow Wet Etch

Wet chemical etching is a simple method of patterning small features in many material systems. The desired pattern is created in a mask material that resists the etch solution and then transferred to the sample material by simply immersing the sample in the etch solution for an appropriate time. For a GaAs/AlGaAs heterostructure, it is obvious that an etch depth greater than the depth of the 2DEG will ensure good confinement. However, submicron structures are not much larger than the depth of the 2DEG and they will be destroyed by such a deep etch because of depletion and damage at exposed edges. Fortunately, a deep etch is only

necessary for good confinement near room temperature and a much shallower etch results in good confinement for temperatures below about 100 K.

The use of shallow wet etching in the fabrication of submicron structures in a GaAs 2DEG has been reported by Lee *et al.*, 1991. They used an etch solution of $NH_4OH/H_2O_2/H_2O$ (10:3:1000) and PMMA as an etch mask. After patterning the PMMA with EBL they etched the samples in 10 s intervals and measured the etch depth after each interval until the target depth was reached. The necessary depth depends on the details of the heterostructure layers, but typically the GaAs cap layer and < 100 Å of the AlGaAs were removed. The Fermi level pinning at the AlGaAs surface is then sufficient to deplete the 2DEG beneath the etched regions. At room temperature there is still conduction through the doped AlGaAs layer and the surface states, but at low temperature this freezes out and the electrical confinement of the 2DEG under the mesa is complete.

A shallow wet etch is particularly attractive because it potentially introduces less damage into the final structures than other fabrication methods. The EBL for an etch step exposes only the regions that will be etched and not the conducting structures, so damage from the high energy electrons is automatically avoided. It is possible to avoid exposure to other high energy particles by eliminating common processes such as reactive ion etching and oxygen plasma cleaning. Since the 2DEG and most of the donor layer are not exposed to the edges of the mesa, the depletion distance is small and there is no damage in the plane of the 2DEG as with a deep etch.

Ismail *et al.*, 1991 have used the shallow wet etch technique to make wires of (structural) size 0.4 μm by 2-4 μm and have placed a large area gate over each one to vary the electron density. At low temperature they measured the conductance as a function of gate voltage and found steps of size $2e^2/h$. Such conductance steps had previously been seen only in wires of length shorter than 0.5 μm, known as "quantum point contacts". Ismail *et al.* interpret their results as indicating very clean edges in their wires, and they attribute this property to the gentle nature of the shallow wet etch and the avoidance of any high energy particles throughout the microstructure fabrication. Washburn has since made 0.2 μm wires which did not conduct without a gate, but could be turned on with a gate voltage of order 0.1 V (S. Washburn, private communication, 1993). Smaller wires could not be turned on at all at low temperature. Washburn has also found that the gate voltage changes the electron density without affecting the wire width over a significant range and that the conducting width of the wires is very close to the structural width.

These results indicate the shallow wet etch technique is capable of producing structures with the same attractive properties as samples made by ion exposure. Since Li *et al.*, 1993 find that ion exposure may do little more than remove material from the surface, this is not surprising. It also has a significant advantage over ion exposure in that it is much simpler to dip a sample in liquid than to measure its resistance in a vacuum chamber while bombarding it with ions. The apparent size limit of 0.2 μm is not a problem for the chaotic scattering work because narrower leads would not have enough modes to be in the desired semiclassical regime (see Section 3.3).

The shallow etch process used at Yale was as follows. After completion of the large scale fabrication, a pattern of trenches defining the cavities and leads was written by EBL in a single layer of PMMA. The sample was then immersed in an etch solution of $NH_4OH/H_2O_2/H_2O$ (5:1:1000) plus 5 drops of detergent to reduce surface tension, and gently agitated by hand for approximately 100 s. It was then taken to a probe station where the resistance between various pairs of ohmic contacts was measured. An enclosure for the probe station was built so that these measurements could be done in a nearly dark environment. This process was repeated, with progressively shorter etch times, until the target resistances were obtained. The correct target values for a given pattern of microstructures were found by trial and error. The PMMA etch mask was then stripped and an image of each microstructure was made with a scanning force microscope. A pattern of large area gates covering each structure was defined by EBL and liftoff of Ti/Pd/Au, using a bilayer of PMMA. The completed sample was then bonded to a 24 pin header.

Approximately 15 samples were made using the shallow etch technique, and of these, MBE17S1 and MBE17S6, and MBE17S9 were measured carefully at low temperature.[14] The process converged on success much faster than the ion exposure process for several reasons. First, a new set of optical lithography masks was designed and fabricated at the National Nanofabrication Facility at Cornell, and these Cr on quartz masks were of much higher quality than the emulsion masks made in the darkroom at Yale that were used for the ion exposure samples. These masks and increased attention to many small details made the large scale fabrication

---

[14] Two of these samples, S1 and S6, were good in all respects except for the ohmic contacts. The contact resistance was so high that the cavities could not be cooled to the temperature of ≈ 100 mK required to study the chaotic scattering (see Section 6.1). The changes to the ohmic contact process that produced much better contacts in sample S9 are described in Appendix E.

fairly reliable. Second, the EBL was done by Jeff Sleight on the JEOL system in Professor Reed's lab, and this process also became reliable after a few trials. Third, the refinement of the microstructure fabrication was greatly aided by scanning force microscope images of the samples at various stages in the process. These images were provided by Dr. Mark Amman using the Park Scientific system in Professor Reed's lab. Finally, the simplicity of the wet etch itself resulted in a high rate of success for samples that reached the final step intact.

Figure 4.4 shows the etched microstructures of sample MBE17S9. Details of the fabrication of this sample are given in Appendix D. Measurements of this sample will be presented in Chapter 6.

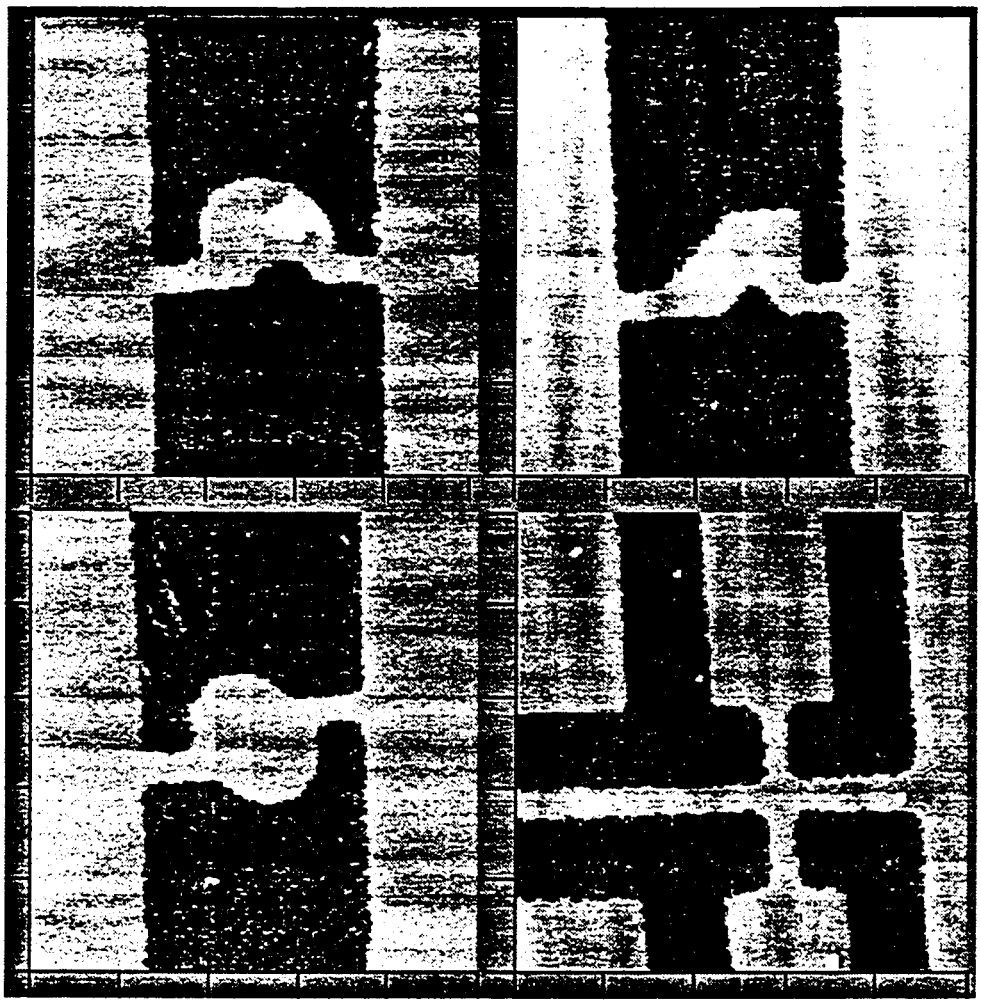

Figure 4.6 Scanning force microscope images of the structures of sample MBE17S9 after wet etch and PMMA strip. Clockwise from upper left: Stomach, Polygon, Cross, and Stadium. Ticks are separated by 1 μm. The dark regions are the trenches etched into the surface of the GaAs. They have a depth of ≈ 230 Å and an RMS roughness of ≈ 20 Å. The 2DEG lies underneath the lighter, unetched regions. The bright spot on the Stomach is contamination on the surface of the GaAs, about 100 Å taller than the surrounding unetched surface, which is not expected to affect the 2DEG. The sharp lines cutting across the images are due to sudden changes in the microscope tip during the scan and do not correspond to real topographic features. After these images were taken, a large area metal gate was placed over each structure and its leads. Images courtesy of Dr. Mark Amman.

5

EXPERIMENTAL APPARATUS AND TECHNIQUES

5.1 ^{4}He and ^{3}He Baths

The first cooldown of each sample was done using a dipstick cryostat in a ^{4}He glass dewar containing a superconducting magnet. The system was essentially the one described by Klepper, 1991. The dipstick was originally configured to accept the 8 pin Yale headers, and was later rewired to accept the 24 pin Jade headers. A temperature of 4.2 K was sufficient for determining whether the sample had cavities that were properly confined, ohmic contacts that survived to low temperature, and good isolation between the gate and the 2DEG. Samples which looked promising at T = 4.2 K were measured at the lowest temperature available: $T \approx 0.3$ K in the ^{3}He system in Professor Wheeler's lab early in the work, and $T \leq 100$ mK in the dilution refrigerator system later on.

5.2 Dilution Refrigerator

A schematic dilution refrigerator (DR) is shown in Figure 5.1. The refrigerant in a DR is ^{3}He, which is pumped through the following closed cycle. ^{3}He from a sealed pump enters the Condenser, which has a high impedance and is cooled by a minature ^{4}He bath called the Pot. The liquid ^{3}He flows down through heat exchangers until it reaches the Mixing Chamber (MC). Inside the MC are two fluids separated by a phase boundary. One phase is nearly pure ^{3}He from the Condenser and the other is ≈ 6 % ^{3}He in an essentially inert background of liquid ^{4}He. The second phase extends back up through the heat exchangers to a chamber called the Still. ^{3}He atoms are removed from the Still by the sealed pump, and for each ^{3}He atom pumped from the Still, another must cross the phase boundary in the MC. As it crosses, it must absorb energy equal to the latent heat for dilution of ^{3}He into the other phase. Thus the continuous flow of ^{3}He atoms through the system provides continuous cooling power at the MC. Unlike evaporation of a liquid, the cooling power of ^{3}He dilution does not fall exponentially with temperature, and this allows the MC to reach much lower temperatures than a simple liquid bath. More

detailed discussions of the principles and practice of dilution refrigeration can be found in the books by Lounasmaa, 1974 and Richardson and Smith, 1988.

The Yale DR was purchased from Oxford Instruments, complete with gas handling system, electronics, dewar, and superconducting magnet. The DR itself was a KelvinOx model, with a base temperature of about 30 mK and a cooling power of about 40 μW at 100 mK. The magnet provided a field of 9 T at 4.2 K or 11 T if the lambda-point refrigerator was used. The sample was mounted outside the MC on an extension rod which placed it at the center of the magnet. Oxford provided detailed operating instructions for all routine procedures. Notebooks for the system contain records of modifications and performance on each cooldown.

The basic steps involved in cooling the system were as follows.

1. Mount sample and attach vacuum can surrounding Pot, Still, MC, and sample.
2. Evacuate vacuum can. (Optional: Leak check vacuum can seal.)
3. Insert DR into dewar and attach pumping lines. Leak check pumping lines. (Optional: Leak check DR.)
4. Transfer LN2 into main bath, wait overnight for magnet and DR to reach $T \approx 77$ K.
5. Blow LN2 out of main bath. (Optional: Leak check DR at 77 K.)
6. Put He exchange gas into vacuum can. Transfer LHe into main bath, wait for DR to reach 4.2 K.
7. Pump exchange gas from vacuum can.
8. Condense $^3He/^4He$ mixture into DR.
9. Begin circulation of ^3He.

The time required to take the system from 300 K to 30 mK varied from several hours if the magnet and dewar are already at $T \approx 77$ K to about 2 days if the magnet was at 300 K and careful leak checking was done at 300 K and 77 K. Once the circulation was started the system reached its base temperature in about 30 minutes. The system required about 45 liters of LHe for the initial transfer and had a usable volume of 20 liters, which lasted about 40 hours under typical conditions.

During circulation the DR system was monitored by resistance thermometers located at the Pot, Still, MC, and sample position. These thermometers were measured using an RV-Elektroniika Oy Model AVS-46 AC resistance bridge. The AVS-46 had a 7-channel multiplexer input and could be controlled by a computer through a GPIB interface. Heater power for the Still and

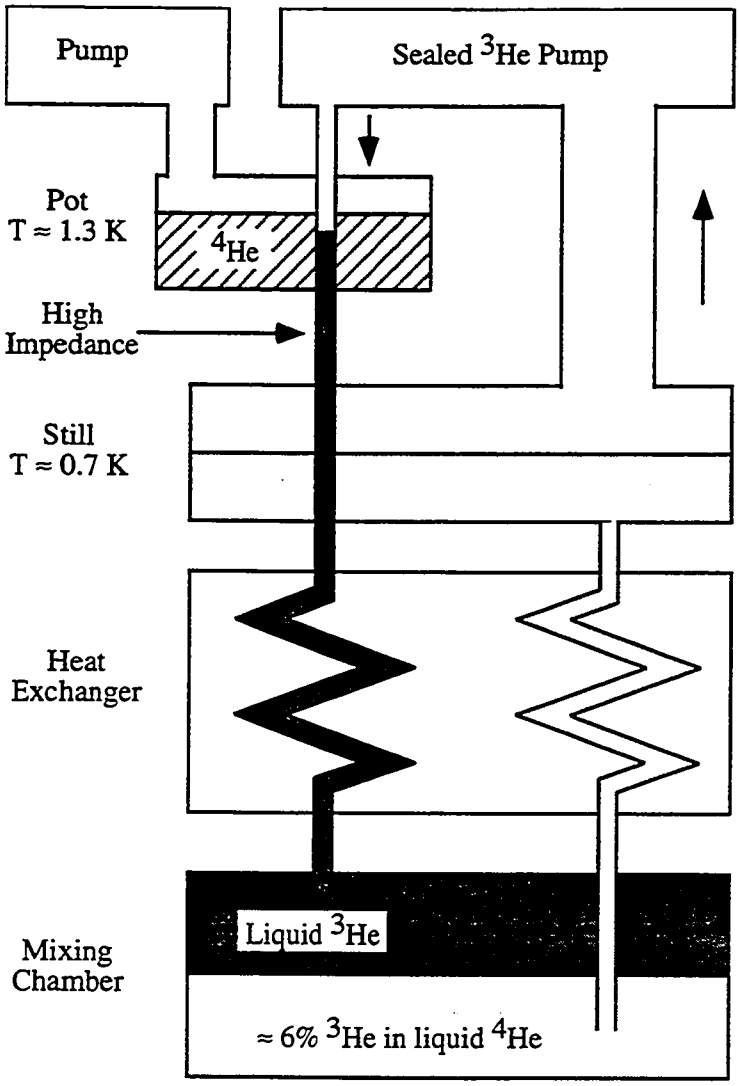

Figure 5.1 Schematic dilution refrigerator. See text for description.

MC was supplied by the Oxford Instruments Model 2603 DR power supply. The AVS-46 and the DR power supply were coordinated into a feedback loop for MC temperature control using an RV-Elektroniika Oy Model TS-530 temperature controller. The MC could be maintained at temperatures up to 0.5 K without disturbing the circulation process.

The superconducting magnet was controlled by a Lakeshore Cryotronics Model 612 Magnet Power Supply. This supply provided current steps of 1 mA, (field steps of 1.066 G for the Oxford magnet), over the entire field range to 11 T. It could be controlled by a computer through a GPIB interface.

Leak checking and high vacuum pumping were done with a Veeco MS-9 leak detector.

The rest of this section describes the most important modifications to the standard DR system, other than the sample mount and wiring which are discussed in the next section.

• The system was delivered with 48 extra leads installed by Oxford from the top of the DR to the sample position. The wires were approximately 36 A.W.G. Constantan or Cu from room temperature to the Pot plate, 50 μm diameter NbTi in a Constantan matrix from the Pot to the MC, and approximately 30 A.W.G. Cu from the MC to the sample position. The superconducting NbTi and Constantan matrix produced a negligible heat load on the MC, even for a large number of such wires.[15] The Cu wires were wrapped around Cu posts to thermally anchor them to the MC temperature. These leads were used for the RuO sensors (see below) and for the sample.

• Two coaxial lines[16] were installed by Oxford from the top of the DR to the Pot plate. These lines would have to be extended to the sample position, with careful design to minimize their heat load, before they could be used. The SMA connectors at room temperature and at the Pot plate were terminated to prevent high frequency noise from entering the vacuum can.

• The temperature at the MC and the sample position was monitored with ruthenium oxide (RuO) resistance thermometers purchased from Scientific Instruments. The sample RuO was calibrated from 20 mK to 20 K by Scientific Instruments. The MC RuO was from the same production batch and is assumed to be very similar to the calibrated RuO. Scientific Instruments claims an interchangeability of ≈ 2 mK at 20 mK. The sensors were mounted in a small Cu can with the leads coming out through an epoxy seal. The can was filled with H egas, but at $T \leq 100$ mK the dominant cooling path is probably through the leads.[17]

---

[15] The NbTi wires, designed for making heat switches, were Niomax CN A61/05, 50 μm diameter, from a British company identified only as "IMI". Some discussion was needed to convince Oxford that such wires would not affect the MC temperature. With the 48 wires they guaranteed a base temperature at the sample position of 35 mK instead of the usual 30 mK. (26 mK was achieved.)

[16] Type UT-85 with stainless steel outer conductors and BeCu inner conductors.

[17] The calibrated sensor was sent with phosphor-bronze instead of Cu leads through a misunderstanding with the manufacturer. Nevertheless, with the leads

• High frequency noise filters were inserted into each lead for the sample and the RuO sensors where it entered the cryostat. The filters were commercially available D-type connectors with a pi filter[18] for each lead. A short cable was made to convert the Fischer connectors on the cryostat to D-25 connectors, and the filters could then be inserted or removed easily. A D-37 filter was also placed at the multiplexer input of the AVS-46 bridge. The filters did not interfere with the bridge measurement at 15 Hz or the sample measurement at 22 Hz. Without the filters the RuO sensors were a few mK colder when the door to the lab was closed than when it was open. When the lab door was open the sensors were also affected by the postion of the door to the office across the hall. Testing with an oscilloscope revealed a large voltage at 100 MHz, presumably from a radio station located on Payne Whitney Gymnasium, which is visible from Becton Center. With the filters in place there was no "door effect".

• The Lakeshore magnet power supply was found to heat the RuO sensors significantly above base temperature, but this problem was eliminated by attaching a power filter to its output. [19] The Lakeshore 612 is a switched DC supply. As delivered, the supply produced a spike at ≈ 23 kHz of almost 1 V peak-to-peak at its output. Without the power filter or the pi filters on the sensor leads, turning on the supply (with the magnet leads connected but no current flowing) raised the temperature of the sample RuO from less than 30 mK to about 45 mK. With only the pi filters in place, the temperature rise was about 4 mK, and with the power filter and the pi filters in place, it was less than 0.5 mK, or almost undetectable.

• The persistent switch on the superconducting magnet was removed. The persistent switch heater would not open the switch for currents less than about 65 mA. At this current the heater dissipated about 0.4 W, which corresponds to a LHe boiloff of 0.5 liter/hour. There was little anticipated need for long runs at fixed field, and the magnet power supply stability was sufficient for transport

---

wrapped carefully it has reached temperatures below 30 mK. The uncalibrated sensors were sent with Cu leads, but with thick Teflon insulation which makes it impossible to heat sink the leads by wrapping them. The recommended solution is to cut the original leads very short, attach Cu leads with thin insulation such as polythermalize, and then wrap those.

[18] See Figure 5.3 for a diagram of a pi filter. The D-type connectors were made by Spectrum Control, Inc. and had a capacitance of 4 nF. The manufacturer claimed an attenuation of 46 dB at 100 MHz and 3 dB at 0.8 MHz.

[19] The power filter was Filter Concepts model LE100 LH (100 A, 250 VAC).

experiments, so Jon Betts from Oxford Instruments removed the persistent switch.

• A removable LHe trap was added to the circulation path to prevent the DR from blocking. Shortly after installation, the DR began to show signs of minor blockage after several days of circulation. The problem gradually worsened, until the blockage would begin after less than 48 hours of circulation and quickly become almost total. It was found that the blockage could be delayed by keeping the LHe in the main bath above the level of the small fixed trap located in the condenser line just above the flange for the vacuum can. Thus the first attempted solution was to attach a Cu braid to the fixed trap and extend the braid below the minimum LHe level. This slowed the blockage but did not eliminate it. Oxford then provided a removable trap to insert into the main bath and the blockage problem disappeared completely.

5.3 Sample Mount and Wiring

The sample mount and wiring for the ^{4}He and ^{3}He bath cryostats were similar to those described by Klepper, 1991. At the relatively high temperatures of these systems the GaAs 2DEG is strongly coupled to the phonons in the chip. Mounting the sample header in a socket with a Cu stub that is linked to the bath and/or surrounding the sample with He gas or liquid then provides adequate cooling. The electrical leads to the sample are usually not involved in cooling the sample; in fact, they are designed to have a low thermal conductance to minimize the heat leak from higher temperature parts of the cryostat.

The situation is different at temperatures below 100 mK in the DR. The coupling of the 2DEG to the phonons becomes very weak and it is thus impossible to cool the electrons by cooling the chip. Heat generated in the 2DEG must flow out through the ohmic contacts, the wire bonds, the header and sockets, and the leads attached to the sockets. This implies several desired features of the sample, the sample mount, and the leads attached to it:

• The sample itself should provide a high conductance path from the microstructures to the ohmic contacts.

• The wire bonds should be Au wire, not Al, to avoid a section of superconducting material in the thermal path.

• The header and sockets should have a high thermal conductance. The ideal design would use purely mechanical contact between the header and the sockets and between the sockets and the leads to avoid the low thermal conductance of solder in its superconducting state.

- The leads should be thermally anchored to the MC temperature and have a high thermal conductance. The ideal lead would have a temperature equal to the MC temperature where it connected to the sockets in the sample mount.

The details of the MC and sample mount in the DR are shown in Figure 5.2.[20] The MC itself was Cu and was bolted to a Cu plate with several threaded holes. An extension rod of Cu and epoxy, constructed by Oxford to minimize eddy current heating, screwed into the bottom of the MC plate. The lower end of the extension had brass threads and a flat Cu stub at the center. The Cu post that supported the sample mount was held tightly against the stub by a brass nut (both Cu faces were polished and cleaned). This Cu post was thus kept close to the MC temperature. The Cu post was soldered to a "Y"-shaped Cu piece. Each arm of the "Y" had a Cu piece extending down to support a circular piece of G-10 epoxy which held the sockets. The G-10 piece contained sockets to accomodate headers with 8, 16, and 24 pins to accomodate the samples of various researchers who used the DR. The outer diameter of the sample mount was 36 mm, which fit easily into the 48 mm inner diameter of the vacuum can without touching the wall. An earlier sample mount with a second vacuum can enclosing the sample had an outer diameter of 45 mm and could not be used because it touched the wall of the main vacuum can, destroying the thermal isolation from the 4.2 K bath.

The wiring for the sample mount was as follows. Cu leads, approximately 30 A.W.G. with polythermaleze insulation, were wrapped several times on Cu posts screwed into the Cu MC plate. Below that they were loosely wrapped around the extension rod, then wrapped tightly around the Cu post just above the sample mount and held in place with GE 7031 varnish. The 24 sample leads were split just above the G-10 piece so that each one was connected to one socket for the 24 pin headers and one socket for the 8 or 16 pin headers. This allowed samples on 8 and 16 pin headers to be cooled and measured simultaneously. Samples on 16 and 24 pin headers could be used together if not all of the pins on each header were needed. Each lead was attached with a combination of SnPb solder joints and removable mechanical contacts such that the assignment of leads to sockets could easily be changed. One or two RuO sensors were attached to leads wrapped in the

---

[20]Sample 161L5 was measured in an earlier sample mount that accepted only the 8 pin headers, with sockets mounted in a Delrin cylinder directly on the end of the Cu post (no "Y" piece). The wiring for this sample mount was essentially the same as described here.

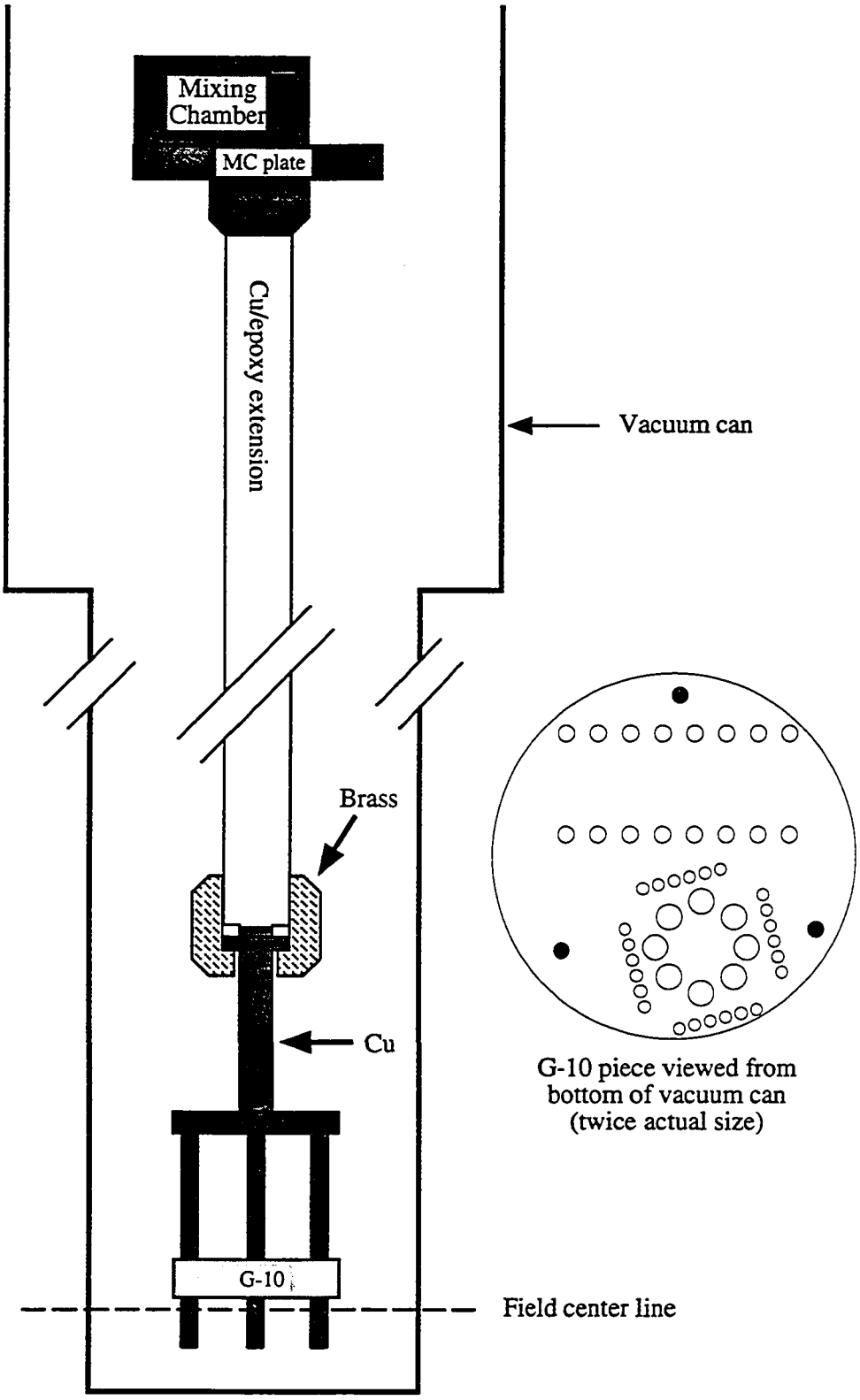

Figure 5.2 Mixing Chamber and sample mount, approximately full size (wiring not shown).

same way. The sensors were then placed in holes drilled in the Cu post or taped to one of the arms of the "Y" with Cu tape.

The scheme described above was not ideal in that it had SnPb solder joints in the thermal path between the sample and the MC. The effect of these joints could be tested by comparing the lowest temperature achieved at zero magnetic field and at a field of a few hundred Gauss, where the SnPb solder becomes a normal metal. No effect was seen with early versions of the sample mount, but with a later version the RuO sensor at the sample position was found to be about 10 mK warmer at zero field than at $B \geq 150$ G. The early versions had fewer solder joints along the thermal path, and more space to wrap the leads at the Cu post just above the sample. A wiring scheme with all joints made mechanically would eliminate this problem, but it would have to be designed carefully to fit into the limited space available.

The temperature difference between the sample and the MC is determined not only by the thermal conductance along the leads, but also by the power that must flow through this thermal conductance. Thus the power dissipated in the sample must be reduced to a minimum. The power necessary to make a resistance measurement can, in principle, be made as small as needed. The power dissipation from electromagnetic noise, which will cause current to flow in the sample, is generally the limiting factor in cooling the sample. This noise is carried through the leads used for the resistance measurement, but it is usually at frequencies much higher than that used for the measurements, so it can be reduced by low-pass filtering of the leads. The shielding and filtering used for the sample leads of the DR system is shown in Figure 5.3. The connections for passing current or measuring voltage were made by plugging coaxial cables into a panel of BNC

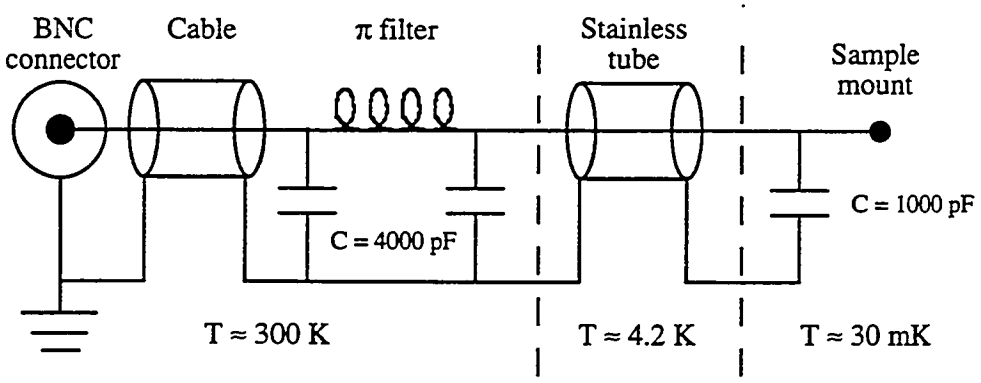

Figure 5.3 Shielding and filtering of leads in the DR system.

connectors. From this panel a shielded cable went to the top of the cryostat, with D-25 connectors so that commercial pi filters could be inserted just before the leads enter the crostat. Inside the metal cryostat the leads passed through the LHe bath inside a stainless tube and entered the vacuum can. Inside the vacuum can the leads were not shielded. Between the MC and the sample mount a polyester film capacitor (C = 1 nF) was soldered to each lead to create a low impedance path for high frequency noise to the MC plate, which was at the same potential as the vacuum can and stainless tube. The sample itself had a much higher impedance than the capacitor, so an additional resistor in series with each lead was not necessary. The leads for the RuO sensor at the sample position were filtered in the same way.

5.4 Small Signal Resistance Measurements

Resistance measurement were done using standard low frequency techniques with lock-in amplifiers (LIAs) for signal detection.[21] The initial measurements used the four-terminal AC bridge described by Klepper, 1991. This bridge was designed for measuring small fractional changes away from a constant average resistance. The chaotic scattering samples had relatively large resistance fluctuations and their average resistance varied significantly, especially when the gate voltage was swept. Therefore a direct measurement of resistance was used, with one LIA for current and one for voltage. Figure 5.4 shows the circuit used for simultaneous measurement of two cavities with a separate gate supply for each cavity. The AC voltage signal is converted into a current source by the 1 MΩ resistor in series with the current leads of the sample. This resistor is also used to sense the sample current.

The LIAs were calibrated by replacing the cavities in the circuit with a decade resistance box. Readings were taken at two known resistance values (spanning the expected range of cavity resistance) to find the multiplicative factor and the offset needed to convert a measurement of LIA voltages to an accurate resistance. The calibration was repeated whenever the gain of the LIAs was changed.

Measurements of each sample were made with several different currents to determine how small the current had to be to avoid heating the sample. A current

---

[21] The LIAs were PAR Model 124 or 126, with PAR Model 116, 117, or 119 preamplifiers.

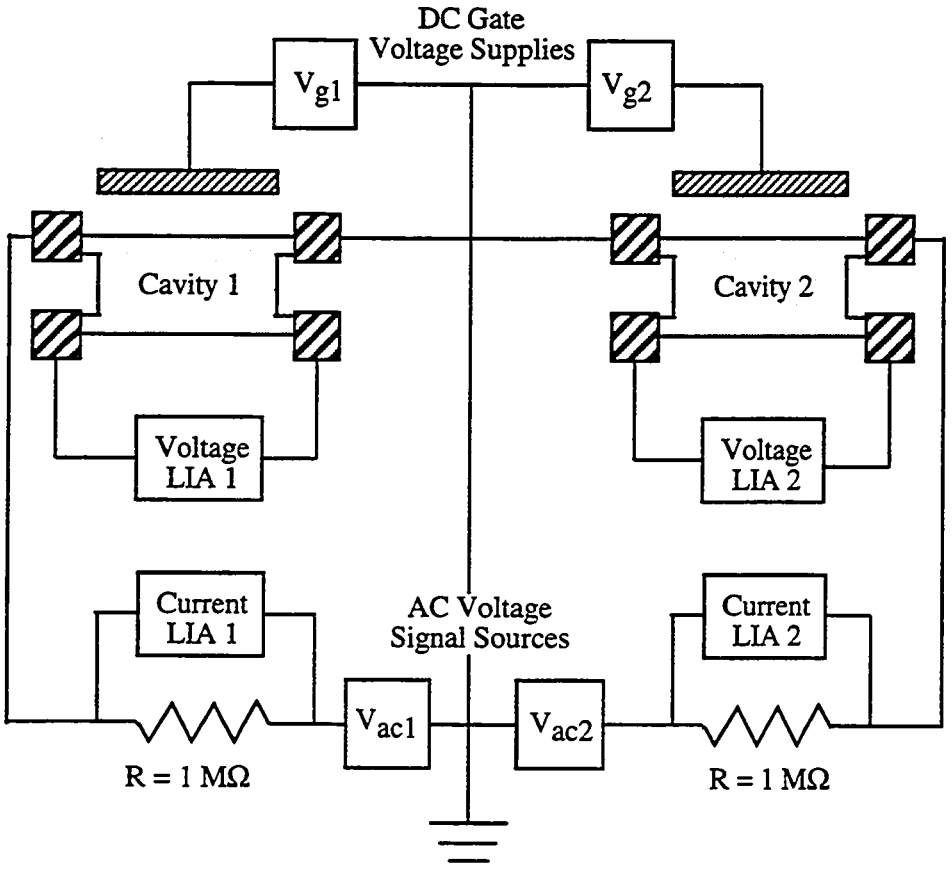

Figure 5.4 Circuit used for measuring two cavities simultaneously, with a separate gate voltage supply for each one. The striped boxes represent the four ohmic contacts for each cavity and the shaded bar above each cavity represents the gate.

between 1 and 3 nA was typical. This produced a voltage signal of order 1 to 50 μV to be detected by the voltage LIA. The output of each LIA was measured with a digital voltmeter with a GPIB interface (Hewlett Packard models 3478A or 34401A) so that the data could be recorded by a computer. The measurement frequency was 22 Hz.

The noise level of the measurement was controlled by the time constant of the LIAs, typically 1 to 10 s, and by the number of voltmeter readings that were averaged to produce each resistance value, typically 1 to 10. The typical sequence used to obtain each resistance value was as follows:

1. Move magnetic field or gate voltage.
2. Wait for magnetic field or gate voltage to settle.
3. Wait three or more time constants for LIAs to respond.

4. Read magnetic field, gate voltage, RuO thermometer, etc. one time.
5. Read each LIA output voltage one time.
6. Repeat step 5 as many times as needed to reduce noise.
7. Average the voltage readings.
8. Compute sample resistance from the averaged voltages and the LIA calibrations.

The gate voltages were produced by Kiethley Model 230 or Yokogawa Model 7651 supplies. The output of each supply was passed through a low pass filter with RC ≈ 1 s before reaching the sample connections. The reading of a digital voltmeter on the sample side of the filter was stable to 0.1 μV.

5.5 Computer Control of Data Acquisition

Early in the work, instrument control and data acquisition were performed by a system based on a Hewlett Packard 9836 computer running code written in HP BASIC. The code, written and modified by several former students, was designed specifically for the four-terminal AC bridge measurement configuration and analog voltage control of the magnet power supply. With the arrival of the DR system shared among three research groups, a much larger variety of instrumentation schemes was anticipated. A Macintosh IIci computer with a GPIB interface card and LabView software from National Instruments was purchased to replace the HP system. LabVIEW's graphical representation of a computer program required some getting used to, but the software makes the coordination of a large number of instruments in various configurations straightforward. A library of LabVIEW virtual instruments was developed to perform the various instrument control functions, such as ramping the magnetic field or changing a gate voltage. These instruments were then integrated into data acquisition routines which controlled the entire process of obtaining a trace of sample resistance versus magnetic field, gate voltage, or time. A routine was also created to monitor the sensors on the DR itself, which provides a record of DR performance that is useful in diagnosing problems.

6

EXPERIMENTAL RESULTS

6.1 Sample Characterization

Before beginning detailed studies of quantum interference effects, several basic aspects of the samples must be checked. Most of these tests can be done using a simple dipstick cryostat, without wasting the time and expense of a dilution refrigerator run on a faulty sample.

The isolation between parts of the 2DEG separated by an etched trench was checked. At room temperature the isolation was of order 1 MΩ (in the dark), and at 77 K and 4 K it was larger than the 35 MΩ limit of the Fluke 77 multimeter. A secondary isolation check was performed by sweeping the gate on one structure while monitoring the resistance of other structures to verify that the various structures could be measured independently.

The leakage from the gate to the 2DEG was measured. For sample 161L5, a relatively crude check gave an upper limit of 100 pA leakage at a bias of +0.2 V ($R > 2$ GΩ). For sample MBE17S9, the I-V curve was measured using an HP4145B semiconductor parameter analyzer. This instrument showed that the gate leakage was less than 1 pA for biases up to about +0.5 V ($R > 500$ GΩ). The leakage obviously must be much smaller than the measurement current, which was 1 to 3 nA, but it must also be small enough that the power dissipation does not heat the 2DEG. The maximum power of (0.5 V)(1 pA) = 0.5 pW is probably negligible, and there was no evidence that the cavities reached noticeably lower temperatures when the gates were shorted to the 2DEG.

The electron density as a function of gate voltage was measured using the magnetoresistance of the cavities at large magnetic field. Typical data are shown in the top plot of Figure 6.1. Landau level quantization produces a resistance that is periodic in $1/B$, similar to the Shubnikov-de Haas oscillations seen in the four-probe measurement of a bulk 2DEG. The period Δ, which can be found from the Fourier Transform (FT) of R *vs.* $1/B$, is related to the electron density n by $n = 2/\phi_0\Delta$. Narrow wires show a deviation from the expected periodicity in the oscillations at small B (see Beenakker and van Houten, 1991 for a review), so the

FT was done only for 3 or 4 oscillations at the highest B. This produced a FT with a single dominant peak, as shown in the bottom plot of Figure 6.1. Even if the density found in this way is not accurate, due to the narrow channel effects just mentioned, the error should be independent of V_g. Thus the change in n with V_g is accurate, and this is the more important quantity for determining the characteristic scale of the fluctuations in $G(k)$.

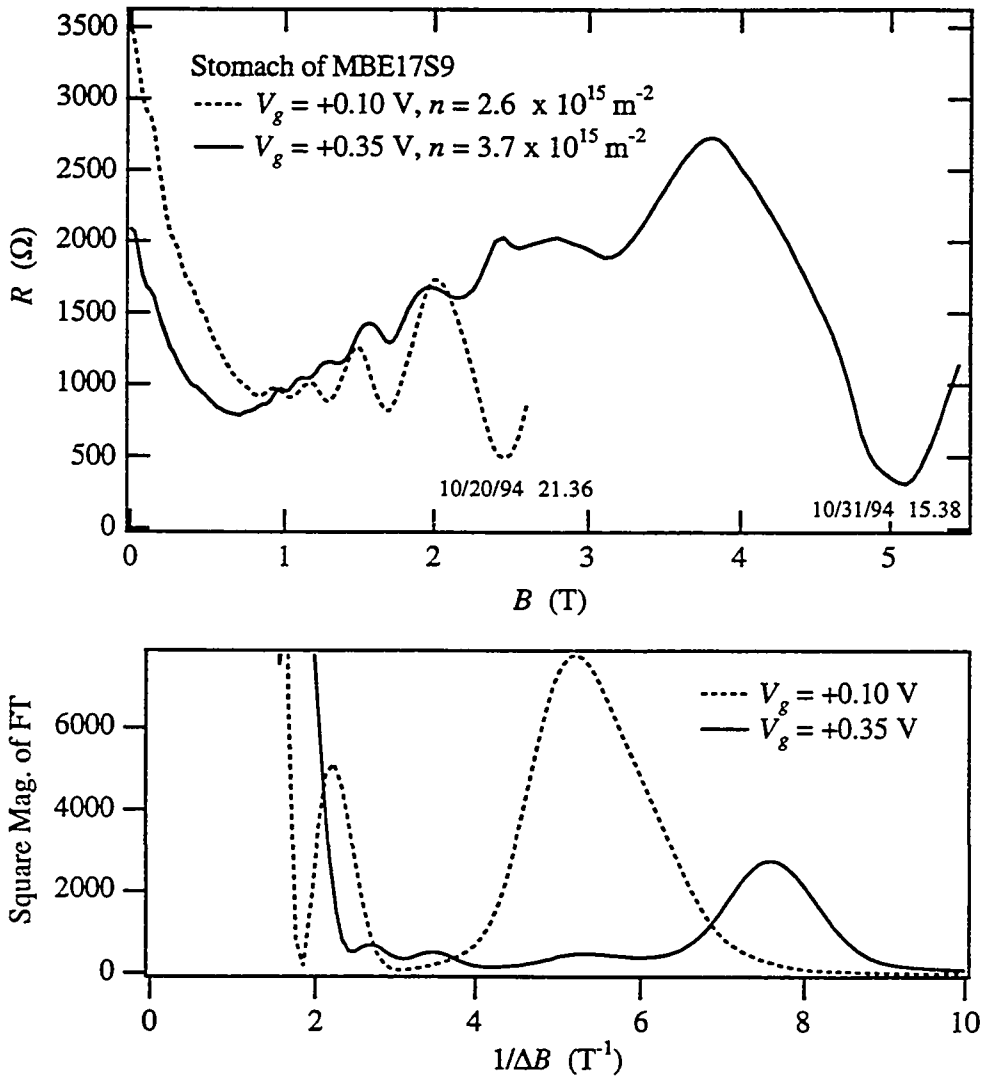

Figure 6.1 Top: $R(B)$ at large B showing the oscillations used to find the electron density. See text for comments of the qualitative change in $R(B)$ with n. Bottom: FT of $R(1/B)$ for B larger than about 1 T. The dominant peak in each FT was used to calculate the electron density in the cavity. Secondary

peaks such as the one at about 2.2 T^{-1} were seen in many cases but are not understood.

The electron density found from the FT of R *vs.* $1/B$ is shown in Figure 6.2. The points fit well to a straight line for each cavity, and the slopes are comparable to the value of 7.2 x 10^{15} $m^{-2}V^{-1}$ estimated by assuming the gate and the electron gas form an infinite parallel plate capacitor. (For sample 161L5, where the gate metal did not overlap the edges of the structures, the capacitance was about half the parallel plate estimate of 8.0 x 10^{15} $m^{-2}V^{-1}$.) This calibration of the gate voltage was done on each cooldown, with the results for a given sample approximately the same each time.

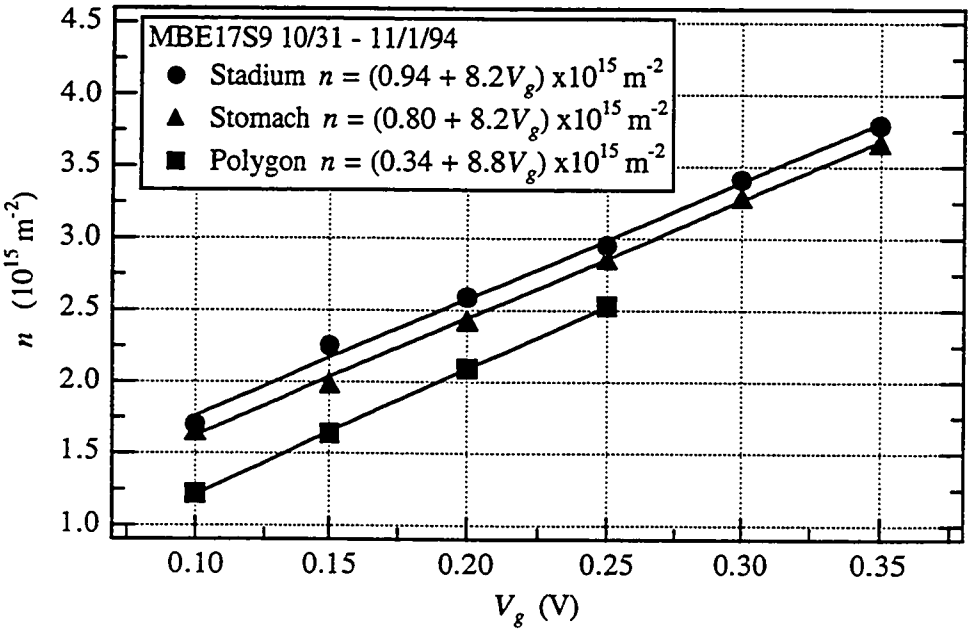

Figure 6.2 Density *vs.* gate voltage for the cavities of sample MBE17S9.

The Fermi wavevector k was calculated from n using the 2D relation $k = \sqrt{2\pi n}$. In the narrow leads the electron gas is quasi-1D, with discrete subbands given by the waveguide modes described in Section 3.2. The 2D relation is only approximately true, but for the samples discussed here with $kW/\pi \geq 5$ it is expected to be a good approximation. (In particular, the error introduced into the determination of γ from the power spectrum of $G(k)$ is expected to be less than the uncertainty from the fitting process.)

Figure 6.1 shows a qualitative change in $R(B)$ that was observed for each cavity of MBE17S9: At low n, $R(B)$ resembles that of a bulk 2DEG, while at

higher n, $R(B)$ has an upward sloping background. This change in behavior is not understood, but it is probably related to the fact that the spatial extent of the skipping orbits at the edges of the sample changes with n. At higher n the orbits are larger, and more coupling between the opposite edges of the narrow leads is expected. For sample 161L5, which had somewhat narrower leads and a lower density than sample MBE17S9, $R(B)$ always showed the bulk-like behavior seen for the lower density in Figure 6.1.

A small cross structure (see Figure 4.6) was fabricated along with the cavities on each sample. The leads were made the same width as the cavity leads. The Hall resistance of such a cross has been observed to display two features that are signatures of ballistic transport (Roukes *et al.*, 1987; Beenakker and van Houten, 1991). Both of these features can be seen in Figure 6.3. The first is the region near $B = 0$ where R_{Hall} is nearly zero (inset) and is known as the "quenching" of the Hall effect. The second is the flat region in R_{Hall} around $B \approx \pm 0.5$ T, which is known as the "last plateau" because it is reminiscent of the quantized steps at multiples of h/e^2 that appear at higher fields. For comparison, the dashed line shows the Hall effect for a bulk 2DEG. A theoretical model for these ballistic effects (Beenakker and van Houten, 1990) predicts the resistance on the low field edge of the last plateau is given by

$$R_{LP} = \frac{h}{2e^2}\frac{\pi}{kW} \tag{6.1}$$

and the upper field at which the last plateau meets the line for the bulk Hall effect is given by

$$B_{LP} = \frac{2\hbar k}{eW} \tag{6.2}$$

The last plateau can therefore be used to estimate the width of the wires that form the cross. Figure 6.4 shows the lead width obtained in this way for the cross of sample MBE17S9. The quantitative accuracy of this measure of lead width is not known, and in one case a fairly large discrepancy with other techniques for obtaining the width has been reported (Roukes, Scherer, and Van der Gaag, 1990). Regardless of the accuracy, these data show that the electron density can be changed by a factor of two with only a 20% change in the lead width.

Assuming the lead width from the last plateau feature is roughly correct, the depletion width can be determined and the actual cavity dimensions can then be estimated. (This is how the cavity dimensions listed in the Sample Profiles of Appendix D were obtained.) For sample 161L5 a scanning electron microscope image (Figure 4.5) gave a structural width of 200 nm for the metal mask/gate, and

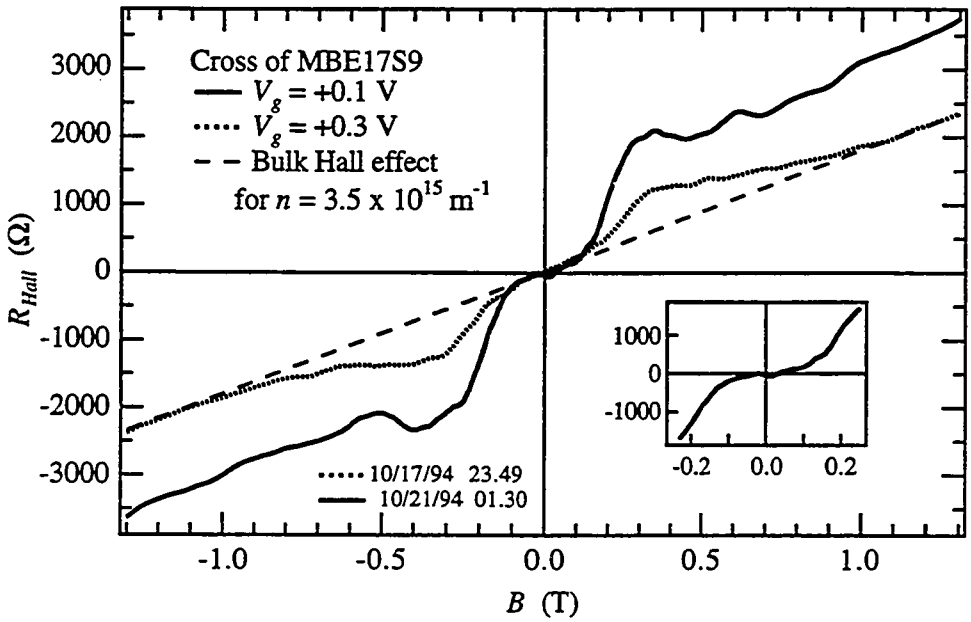

Figure 6.3 Ballistic features in the Hall resistance of a cross junction. The last plateau around $B = \pm 0.5$ T was seen at every gate voltage. The quench was not always seen, and the solid line is the data which showed the most pronounced quench for this sample (inset).

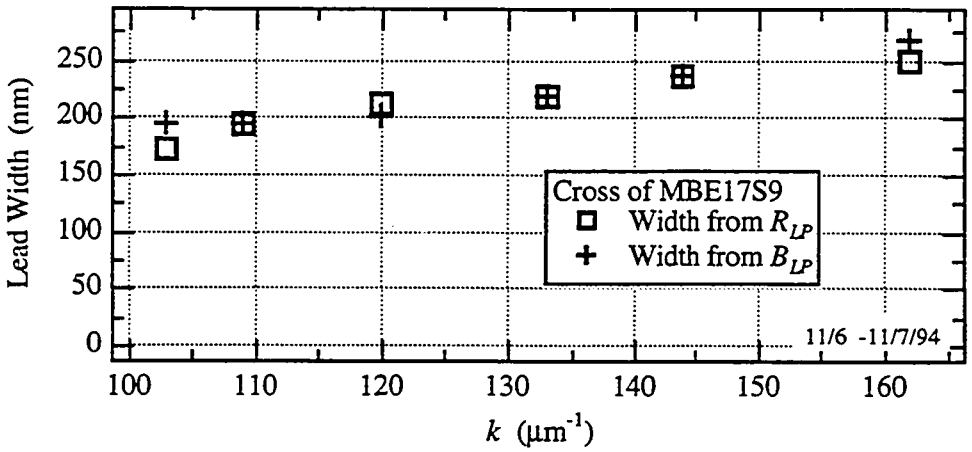

Figures 6.4 Lead width obtained from the last plateau feature in the Hall resistance of the cross structure.

the last plateau of the cross gave a width of 150 nm. This implies a depletion width of 25 nm on each side. With this small amount of depletion the actual shapes of the cavities can be assumed to be very similar to the image in Figure 4.5. For sample MBE17S9 a scanning force microscope image (Figure 4.6) gave a

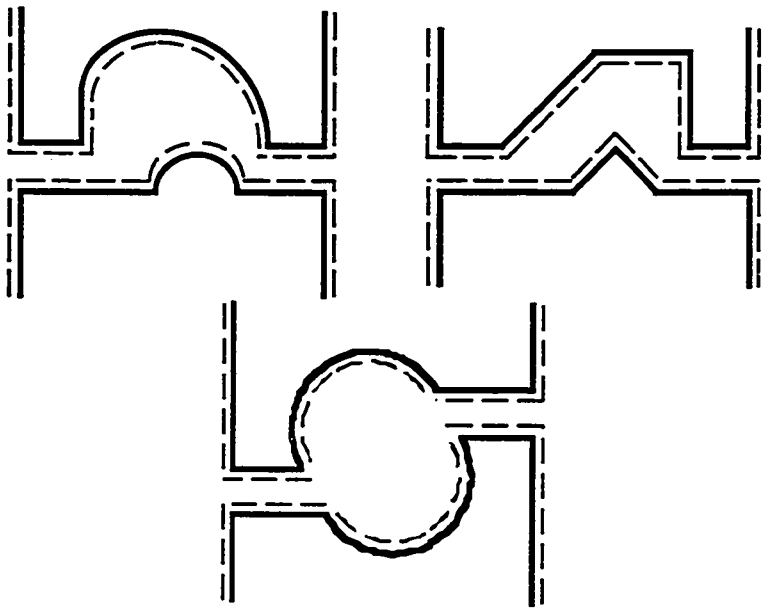

Figure 6.5 Scale drawings of the cavities of sample MBE17S9 showing the edges of the etched mesa as solid lines and the edges of the electron gas with 85 nm of depletion as dashed lines. There would also be significant rounding of the corners which is not shown in these drawings. The solid lines are based on the scanning force microscope images of Figure 4.6.

structural width of 400 nm, so the width shown in Figure 6.4 implies a depletion width of 75 to 100 nm on each side. This larger amount of depletion has a significant effect on the shapes of the cavities. Figure 6.5 shows scale drawings of the cavities (based on the force microscope images of Figure 4.6) where the solid lines indicate the edges of the etched mesa and the dashed lines indicate the edges of the actual conducting regions for a depletion width of 85 nm. The leads are still several times larger than the Fermi wavelength of ≈ 45 nm, but the ratio of the lead width to the total cavity size is smaller than the structural images indicate.

The final aspect of sample characterization was an estimate of the electron temperature T in the cavities. This involved two sets of repeated measurements of conductance over a range of B or k that contained a few quantum interference fluctuations. In the first set, the measurement current was varied with the dilution refrigerator at base temperature. At high current the fluctuations were smeared out because of heating of the electron gas. Based on this, a current that caused negligible heating was chosen, and a few fluctuations were then measured with the mixing chamber at several different temperatures. The temperature at which the fluctuations began to smear out was used as an estimate of the electron temperature

when the refrigerator was at base temperature. This works as long as the effective zero of temperature for the quantum interference is below the inferred temperature, *i.e.*, as long as the fluctuations still have some temperature dependence. The characteristic temperature for quantum interference in a ballistic cavity is set by the typical time spent in the cavity: $T_c \equiv \hbar\theta/k_B$. When the electron temperature is well below T_c, the conductance fluctuations have the full amplitude calculated for $T = 0$. According to the method described above, the cavities of samples 161L5 and MBE17S9 reached $T \approx 100$ to 200 mK. This is comparable to the expected values of T_c based on classical simulations (given in Table 7.1). Thus, the method puts an upper bound on T in this case. The fluctuation amplitude was still somewhat lower than the predicted amplitude for $T = 0$ (see Section 6.2.3), so the cavities probably were not much colder than this upper bound.[22] Samples MBE17S1 and MBE17S6, which had much higher ohmic contact resistances, could not be cooled below 300 to > 500 mK, depending on the contact resistance.[23] In these samples the quantum interference features were noticeably smaller.

6.2 Conductance Fluctuations

Figure 6.6 shows typical conductance fluctuations observed when magnetic field or gate voltage was swept. $G(B)$ and $G(k)$ are apparently random, aperiodic functions, but all of the fine features were retraceable, as shown in Figure 6.7.[24] The inset of Figure 6.7 shows a magnified view of a few fluctuations. The conductance fluctuations clearly have a characteristic scale, in contrast to the fluctuations on all scales seen in the deflection function of a single particle scattering

---

[22] There is also a large uncertainty in the expected T_c of the cavities, since the simulations for ideal cavities did not agree well with the experiments in general (see Chapters 6 and 7).

[23] A large electrical contact resistance implies a large thermal resistance according to the Weidemann-Franz law. The heat dissipated in the cavities, due to the measurement or due to noise, must flow through this thermal resistance. This heat flow forces the temperature of the electron gas above that of the refrigerator, in analogy with Ohm's law. See Appendix E for an account of the changes in the ohmic contact process that produced much better contacts in sample MBE17S9.

[24] The pattern changed if the sample was cycled to a temperature of order 100 K or more. In principle, as long as the sample remains below this temperature, the pattern should retrace whenever the gate voltage is returned to the same value. In practice, there was a slight hysteresis and perfect retraces were not observed unless the gate voltage history before each trace and the direction of the voltage sweep were the same.

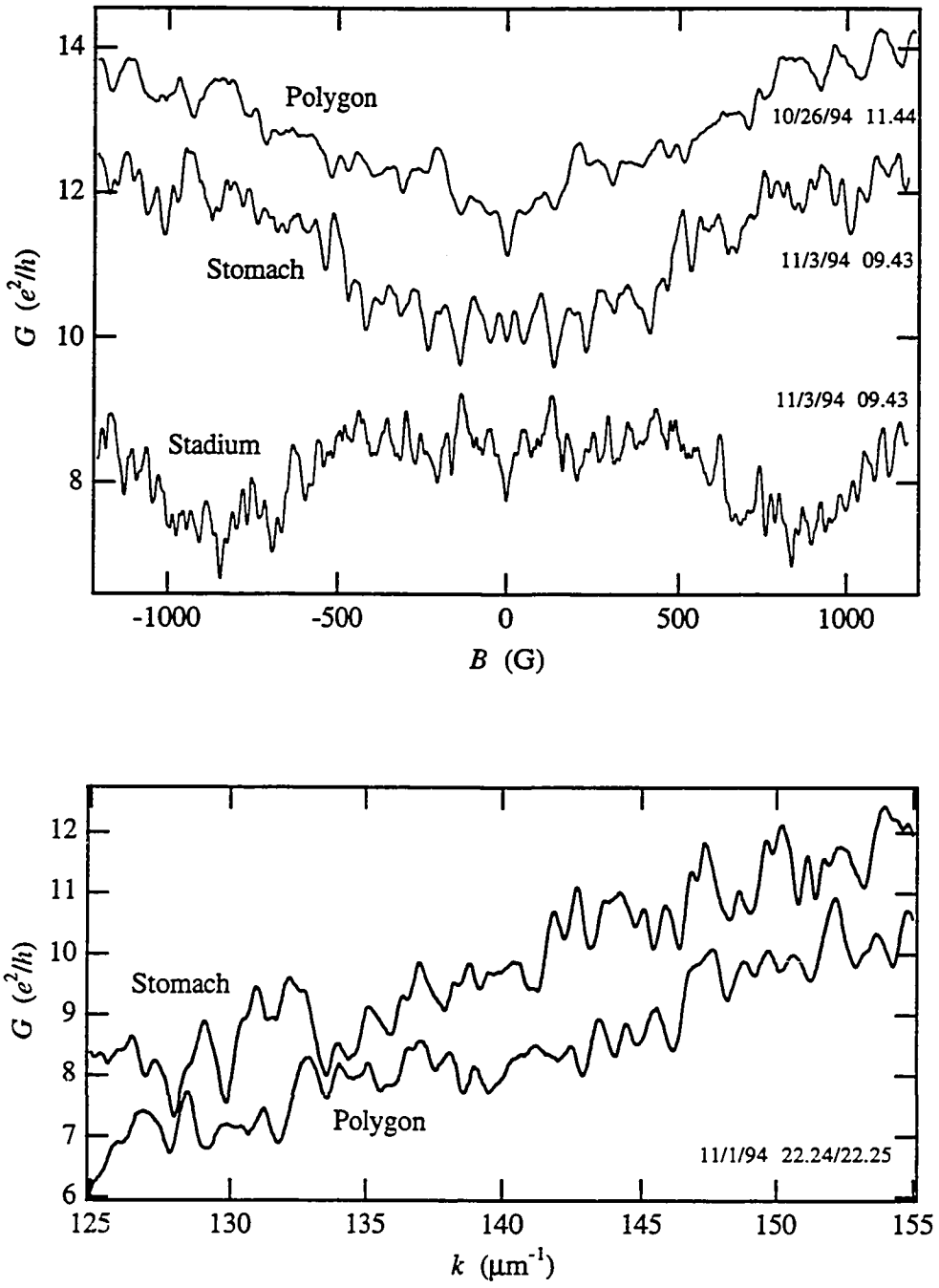

Figure 6.6 Typical fluctuation data at $T_{mc} \approx 40$ mK. Top plot shows $G(B)$ for Polygon, Stomach, and Stadium cavities. The average G reflects the different electron density in each case. A difference in the typical field scale is also evident, especially for the Stadium. This is due to the different cavity shapes; it is not dependent on the density (see Section 6.2.1). Bottom plot shows $G(k)$ for Stomach and Polygon cavities at $B = 0$. These data are from sample MBE17S9.

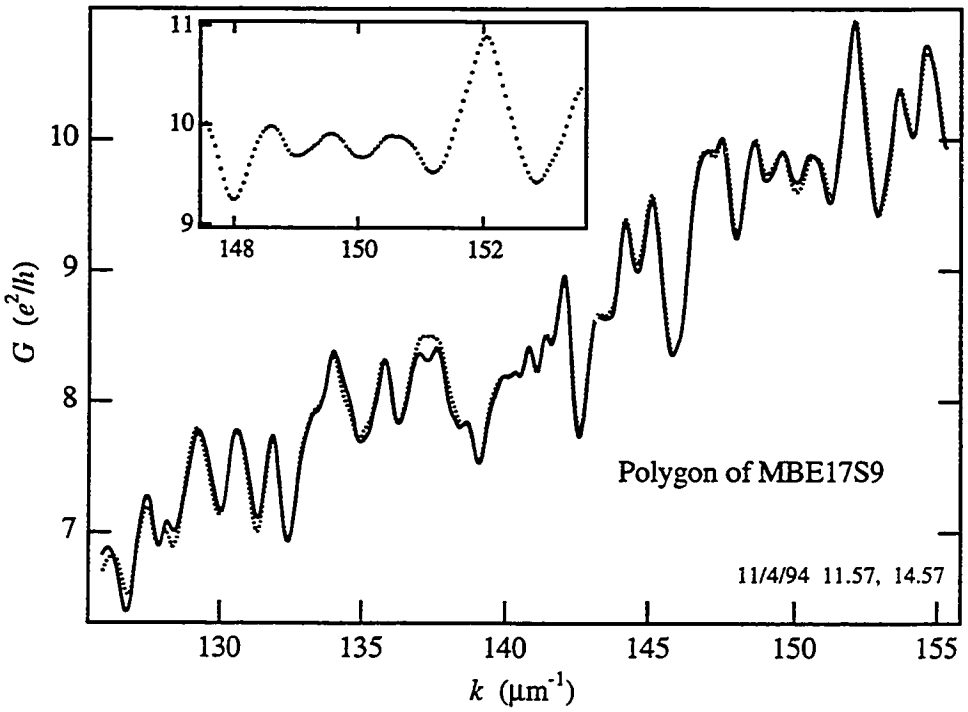

Figure 6.7 Two $G(k)$ traces taken consecutively at $B = 0$ for the Polygon cavity of sample MBE17S9. The imperfections in the retrace, for example at $k = 137\ \mu m^{-1}$, were due to changes in the sample during the time required to obtain the data (about 5.5 hours in this case). The inset shows the density of measured points in k. A similar density of points was used for $G(B)$.

among three disks (Chapter 2). The fluctuations in $G(B)$ were studied in a long-sided stadium by Marcus *et al.*, 1992. Berry *et al.*, 1994b showed that the fluctuations in $G(B)$, as well as the weak localization feature at $B = 0$ (see Section 6.3), are properties of the ballistic cavity itself, since they were not seen in a structure that was much larger than the electron mean free path and phase coherence length. Chan *et al.*, 1994, studied fluctuations in G as a function of a gate voltage that changed the cavity *shape*. Measurements of fluctuations in $G(k)$ for a fixed cavity shape have not been reported before.

The conductance of the cavities was not completely stable in time, and showed occasional discrete changes well above the electronic noise. These changes occured once every few hours if the sample was treated carefully, but the rate increased dramatically if the sample was cooled too quickly or the gate voltage was

changed suddenly by a large amount. Most of the $G(B)$ and $G(k)$ traces had one or two noticeable jumps, and most attempts at retracing the data were imperfect because of these changes. The jumps presumably were caused by some residual impurity motion which still occured occasionally at $T \approx 100$ mK. The different states of the sample were therefore members of the same mesoscopic ensemble, and the jumps do not interfere with the interpretation of the data.

For the cavities of sample MBE17S9, G was symmetric in B because the measurement was effectively two-probe. The stadia of sample 161L5 did not show this symmetry because the measurement was effectively four-probe, but Figure 6.8 shows that $G(B)$ did have the more subtle symmetry required by the Onsager relation (see figure caption).

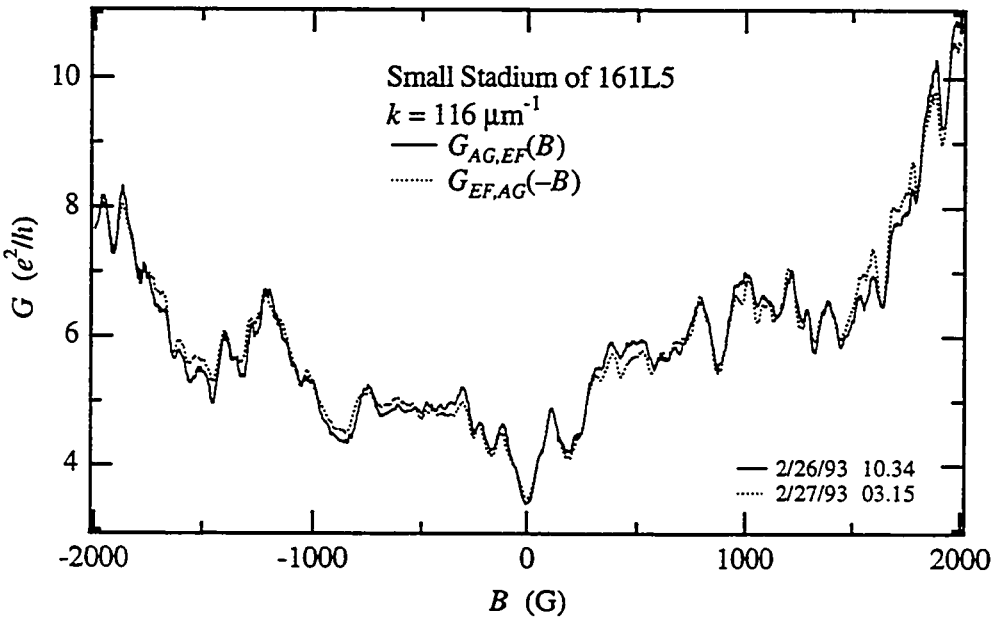

Figure 6.8 $G(B)$ for the Small Stadium of sample 161L5. The Onsager relation requires $G_{ij,kl}(B) = G_{kl,ij}(-B)$, where the first two subscripts label the current leads I^+ and I^-, and the second two subscripts label the voltage leads V^+ and V^- (Buttiker, 1986). This relation was essentially satisfied, with the deviations due to changes in the sample during the 25 hour period of the two field sweeps.

The rms amplitude of the fluctuations at $T \approx 100$ mK was in the range 0.1 to 0.5 e^2/h (see Section 6.2.3). At $T = 4.2$ K the fluctuations were barely visible, as shown in Figure 6.9.

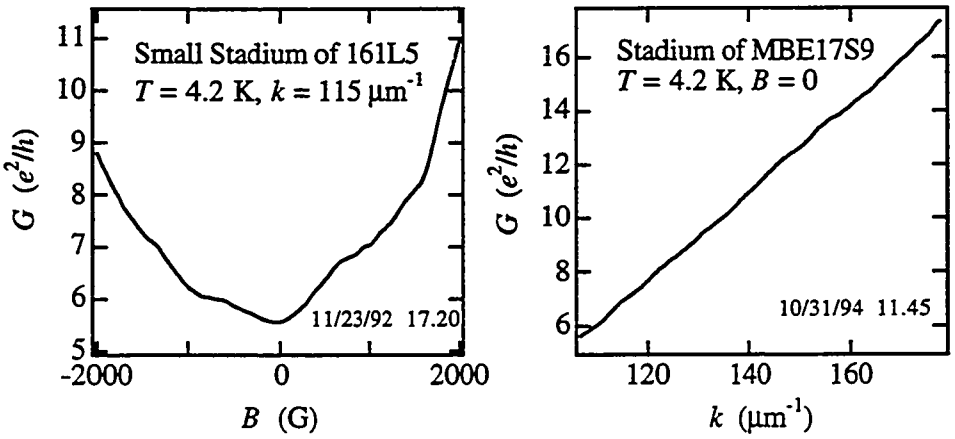

Figure 6.9 Typical $G(B)$ and $G(k)$ data at T = 4.2 K. The quantum interference fluctuations were completely suppressed by thermal averaging and inelastic scattering.

The method for calculating the power spectra of the fluctuations and the recipe for the fits using the semiclassical forms of equations (3.7) and (3.8) will be illustrated for a typical case. S_B is the square magnitude of the Fourier Transform (FT) of $G(B)$. The square magnitude of the FT of a whole $G(B)$ trace is dominated by large fluctuations, as shown in the inset of Figure 6.10. Although these fluctuations are not noise (they are as reproducible as the fluctuations in G), a better fit of equation (3.8) can be obtained if they are smoothed away. The smoothing was done by cutting $G(B)$ into several half-overlapping segments and then computing the logarithmic average of the square magnitude of the FT of each segment.[25] Smaller segments produce a smoother spectrum, but the method is not valid unless each segment is much larger than the typical scale of the fluctuations. A typical smoothed spectrum is shown in the main plot of Figure 6.10. The theoretical prediction of equation (3.8) is nearly a straight line on a semilog plot,

[25] Baranger *et al.* used the same procedure, but with a *linear* average of segments, for the spectra of the numerically-generated fluctuations (see Figure 3.2). As this dissertation was being completed, Baranger pointed out that the linear average is the correct procedure. The effect of the different averages on the spectra was tested and the value of alpha or gamma was affected by about ±2%.

and clearly would not fit S_B over the entire frequency range. The lowest few frequency points in Figure 6.10 reflect the slowly varying background of $G(B)$, which is presumably due to classical bending of the electron trajectories inside the cavities. These points are clearly not expected to fit the form of equation (3.8). All spectra showed a very abrupt change in slope at low frequency (at ≈ 0.005 G^{-1} in Figure 6.10), and this feature was taken as the lower frequency limit for the fit.[26] For frequencies above this feature, S_B was nearly a straight line until a second change in slope occured (at ≈ 0.03 G^{-1} in Figure 6.10), which was taken as the upper frequency limit. As shown in Figure 6.11, equation (3.8) provides a good fit over more than three decades in power and over a frequency range from about $\frac{1}{3}(\phi_o\alpha)^{-1}$ to about $1.7(\phi_o\alpha)^{-1}$.

The second slope change in S_B is not due to noise in the measurement. The effect of noise on S_B was tested by measuring the sample at fixed B as a function of

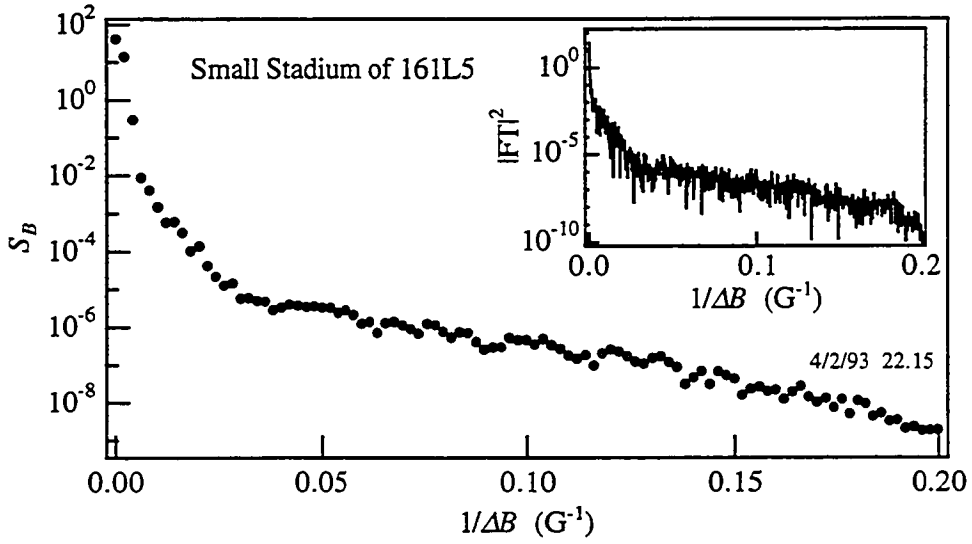

Figure 6.10 Main plot: A typical S_B spectrum computed by averaging the FT of 15 half-overlapping segments of $G(B)$. Inset: Square magnitude of the FT of the whole $G(B)$ trace.

---

[26] The alternative to excluding the low frequency points is to subtract the "background" from the data to put these points in line with the higher frequncy part of S_B. This is difficult to do without biasing the results because it involves identifying some features in the data as "unimportant". It may be possible to determine the true background by measuring $G(B)$ at $T \geq 4.2$ K for the same k as the low temperature trace, but this was not done here. Spectral leakage may have slightly affected the point at the low frequency slope change, but not the points at higher frequency, so it had a negligible effect on the fits.

time under the same conditions as the field sweeps: several hours of readings every 25 seconds. The spectrum of the noise was approximately white and was smaller than S_B over the frequency range used for the fits. The spectra of numerically-generated $G(B)$ fluctuations (Baranger, Jalabert, and Stone 1993b) show a similar deviation from equation (3.8) when the number of modes is around 10 or less, as is the case in the experiments here.

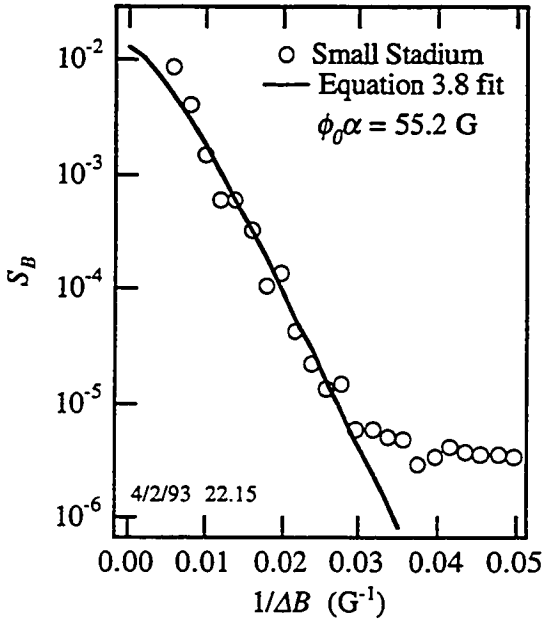

Figure 6.11 Fit of equation (3.8) to the spectrum of Figure 6.10 over the frequency range from 0.006 to 0.030 G^{-1}.

As mentioned in Chapter 3, B must be kept small so the area distribution is not affected by bending of the electron trajectories. Restricting the field range, however, limits the number of fluctuations that can be used for computing S_B. A compromise was made by using data up to a field where the cyclotron radius was approximately equal to the largest dimension of the cavity (*i.e.*, about one half the field where a cyclotron orbit would fit inside the cavity). S_B was computed for several traces using the full range of data as well as subranges at smaller B, and no significant difference was found.

The rest of this section contains a detailed analysis of the fluctuations for the Large Stadium and Small Stadium of sample 161L5 and the Stomach, Polygon, and Stadium of sample MBE17S9. (A summary of all the results can be found in Table 7.1.)

6.2.1 Spectrum of $G(B)$

Fluctuations were measured for each of the four chaotic cavities at several gate voltages. The values of $\phi_0\alpha$ from the fits of equation (3.8) to S_B are shown in Figure 6.12. For each cavity, $\phi_0\alpha$ was roughly independent of k, indicating that the cavity size did not change over the range of voltage used. The spectra at different k were therefore combined to produce an average spectrum for each cavity, shown in Figure 6.13. The fits to these average spectra agree with the mean values of $\phi_0\alpha$ from the individual spectra.

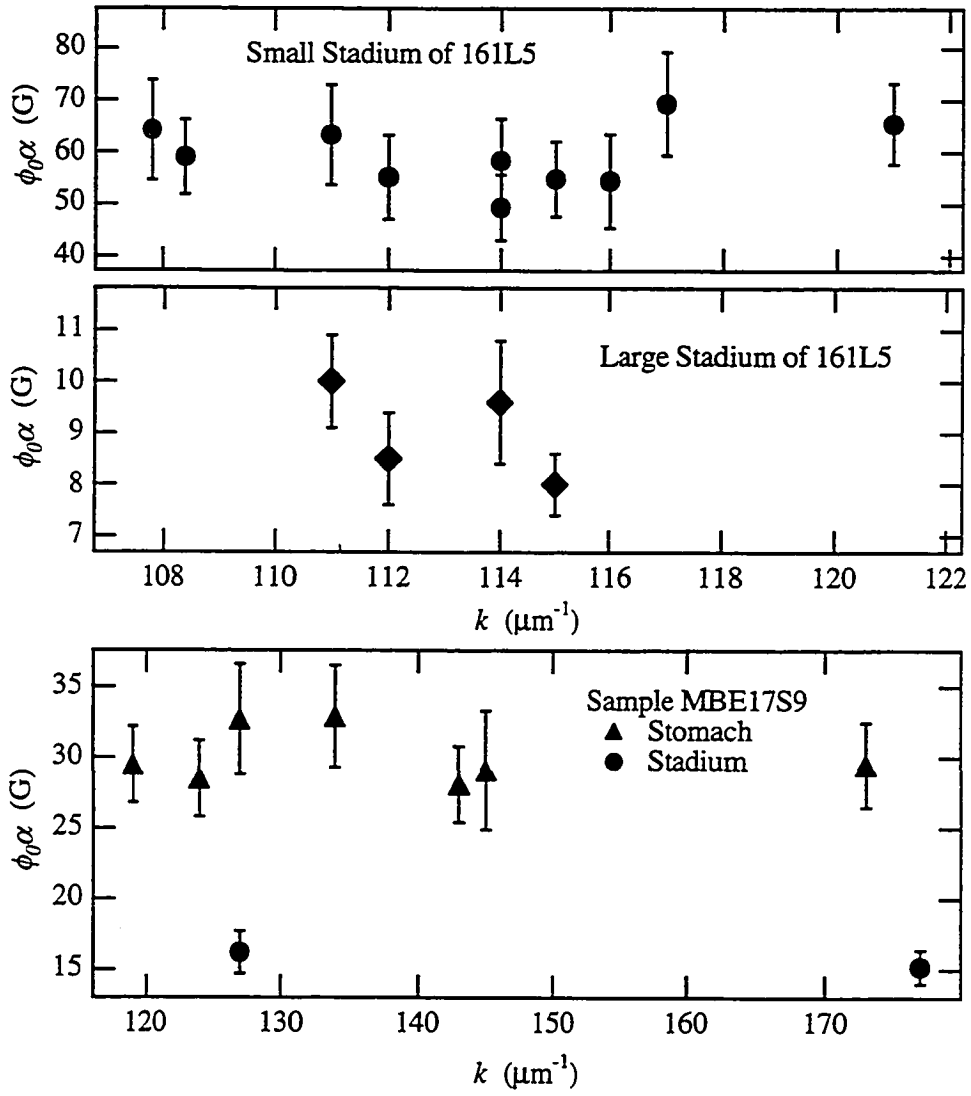

Figure 6.12 $\phi_0\alpha$ values for the four chaotic cavities. (Error bars are $\pm 3\sigma$ as determined by the fitting routine.)

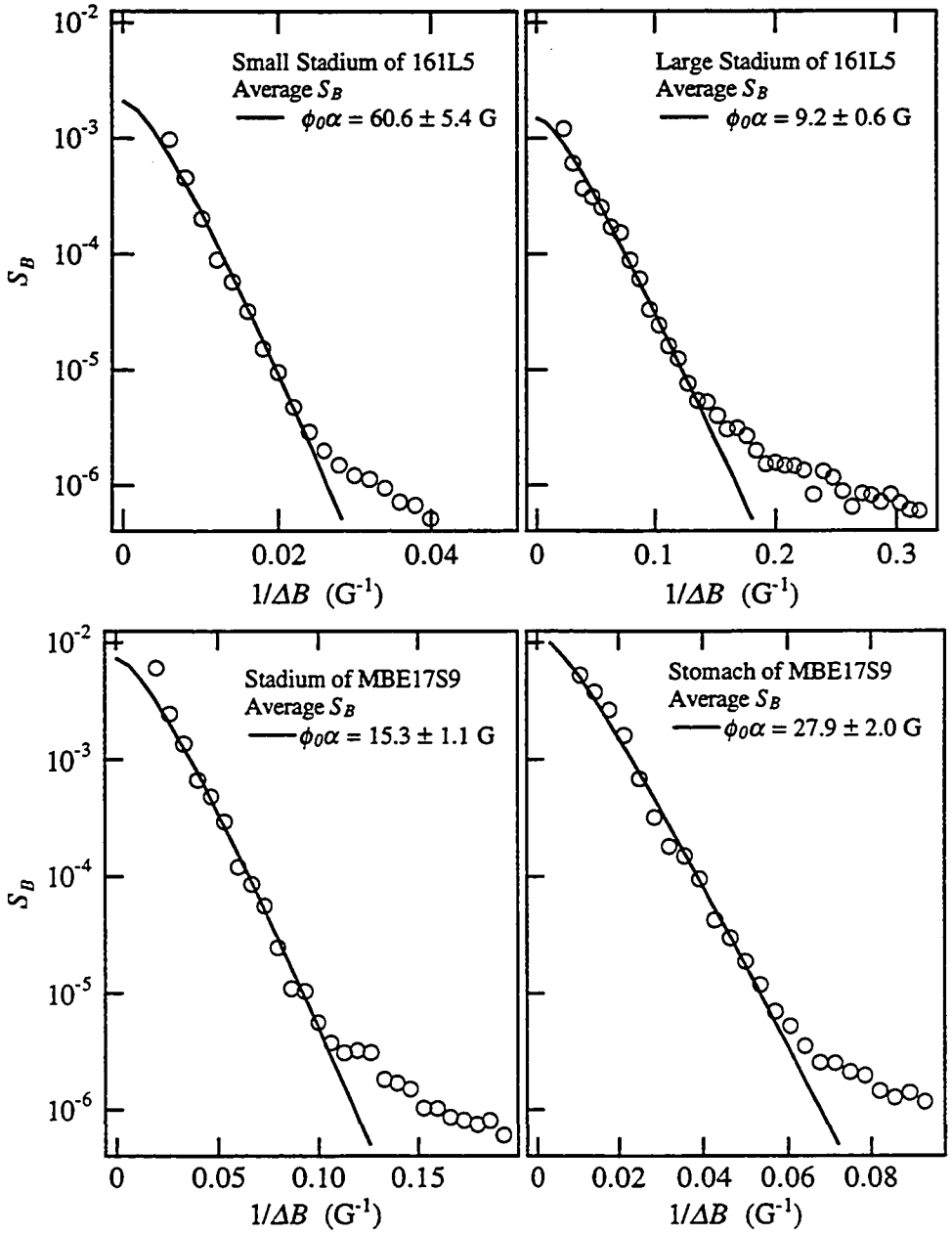

Figure 6.13 Average S_B for the four chaotic cavities (circles) and fits using equation (3.8) (solid curves). (Uncertainties are $\pm 3\sigma$ as determined by the fitting routine.)

Table 6.1 shows a comparison of the experimental values of $\phi_0\alpha$ with the values obtained from numerical simulations of classical scattering. Considering just the three stadia, the agreement is poor for the ideal shapes (mathematically perfect

boundaries), with the experimental values being much larger than expected. This indicates electrons typically enclosed much less effective area than expected. There is a strong tendency for trajectories to circulate in one direction for several bounces in the ideal short-sided stadium. Deviations from the ideal shape destroy this circulation tendency and reduce the typical effective area. Therefore, it is *qualitatively* clear that general disorder in the stadium shape can decrease the effective areas enclosed. The lithographically-defined stadium shape is superimposed on the random impurity potential of the bulk 2DEG. This creates "bumps" in the potential confining the electrons, both at the edges and in the interior of the cavities. An electron traveling across the cavity is not likely to be scattered by a large angle before reaching the opposite edge because the mean free path of the impurity potential is much larger than the cavity size. However, the length for small-angle scattering is comparable to the cavity size[27], so the electron will not follow a straight line to the opposite edge as in the ideal shape. Furthermore, when the electron bounces from the disordered edges it will not bounce with exactly the same angle as in the ideal shape.

Cavity	Experiment	Simulation	
		Ideal	Disordered
Small Stadium[a]	60.6 ± 5.4	23	51
Large Stadium[a]	9.2 ± 0.6	3.5	9.9
Stadium of MBE17S9[a]	15.3 ± 1.1	5.9	14
Stomach[b]	27.9 ± 2.0	32	---

Table 6.1 Comparison of $\phi_0\alpha$ (in Gauss) from experiment and from classical simulations. [a]Simulations by Lin *et al.* 1993 and private communication, using the dimensions given in Appendix D. [b]Simulation by Baranger, private communication. Baranger's result for a Stomach with $L_{dir} = 4W$ has been extrapolated to the actual Stomach dimensions using the arguments for scaling with cavity size by Jensen, 1991 (see Appendix F).

The *quantitative* question of whether the discrepancies shown in Table 6.1 are due to disorder can be answered by choosing a particular model for disorder and repeating the simulation of classical scattering. This has been done for the stadium

[27] A small-angle scattering length of ≈ 0.5 μm was measured using the Shubnikov-de Haas oscillations of a bulk 2DEG sample from wafer MBE17 (J. Pieper, private communication). A somewhat shorter length is expected for wafer 1161.

shape by Lin, Delos, and Jensen, 1993. They changed the scattering angle at the edges of the ideal stadium by a random amount in order to model imperfections only at the cavity edges. As expected, they found that the typical effective area decreased as the size of the random angles increased. For random angles distributed uniformly over $\pm\pi/2$, they found much better agreement with the measured values of $\phi_0\alpha$ in all three stadia, as shown in the "Disordered" column of Table 6.1. The fact that angles up to $\pm\pi/2$ were needed should not be taken as a true indication of the actual disorder at the boundaries, since the effect of disorder in the interior of the cavities must also be accounted for at the boundary in this approach. However, this result does indicate that disorder in general did affect the scattering in the measured cavities. More realistic simulations of disordered cavities, perhaps based on the properties of the impurity potential calculated by Nixon and Davies, 1990, would be helpful.

Turning to the Stomach, the agreement with the simulation for the ideal cavity is quite good. The simulation could be made to agree even more closely if slightly more depletion were assumed in determining the Stomach dimensions. The Stomach presumably has the same disorder as the Stadium from the same sample, but because the ideal Stomach has no strong circulation tendency, its field scale is less sensitive to disorder.

Fluctuations in $G(B)$ of the Polygon were also measured at several gate voltages. Since the classical scattering in the Polygon is regular, S_B was expected to fall off more slowly than the prediction of equation (3.8). However, as Figure 6.14 shows, equation (3.8) provided a fit to the Polygon spectra that was as good as for the chaotic cavities. Fits to all of the Polygon spectra produced the $\phi_0\alpha$ values shown in the inset of Figure 6.14. Since $\phi_0\alpha$ was independent of k, the spectra were combined to give an average spectrum for the Polygon. This average spectrum is plotted along with the average spectrum for the Stomach of the same sample using a normalized frequency axis in Figure 6.15. The two spectra are clearly indistiguishable over nearly four decades.

Figure 6.15 is fairly strong evidence that the area distribution in the Polygon is the same as in the chaotic cavities. The strongest evidence *against* this conclusion that could be found in the $G(B)$ data is presented in Figure 6.16. This plot compares the Polygon spectrum at a *particular* value of k with the Stomach spectrum at another value of k. The Polygon falls off more slowly than the Stomach over the lower part of the spectrum, just as expected if its distribution of

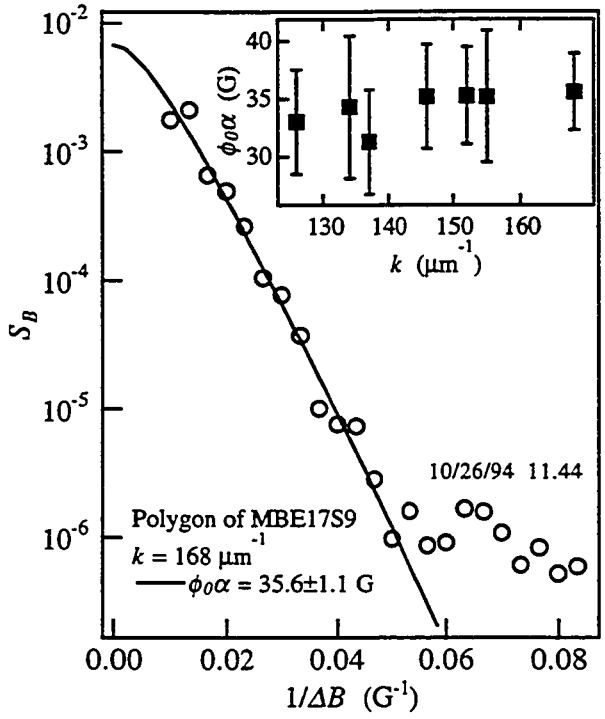

Figure 6.14 S_B for the Polygon of MBE17S9 at k = 168 μm^{-1} (circles) and a fit using equation (3.8) (solid curve). The inset shows the values of $\phi_0\alpha$ for several values of k.

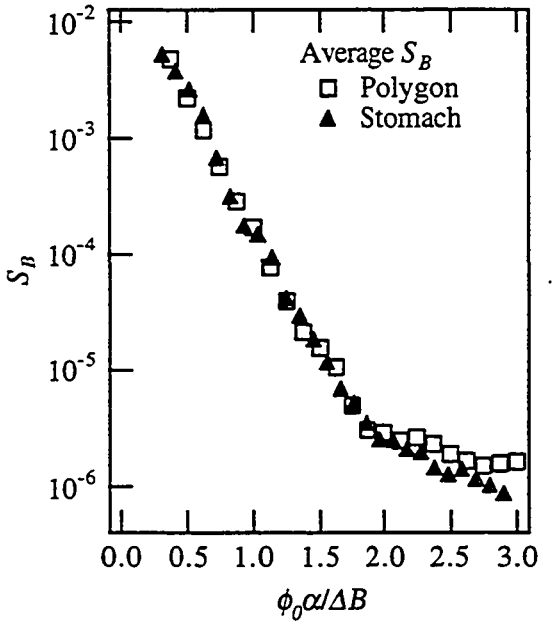

Figure 6.15 Average S_B for the Stomach and Polygon of MBE17S9. The frequency has been normalized by $\phi_0\alpha$ for each spectrum.

areas is a power law instead of an exponential. This data is quite similar to that shown in the original paper on chaotic and regular scattering by Marcus *et al*, 1992. However, no hint of this behavior survives when the spectra at several k values are averaged together, and there is no reason to believe that the particular data shown in Figure 6.16 are more representative of the true spectra of the cavities than are the averages.

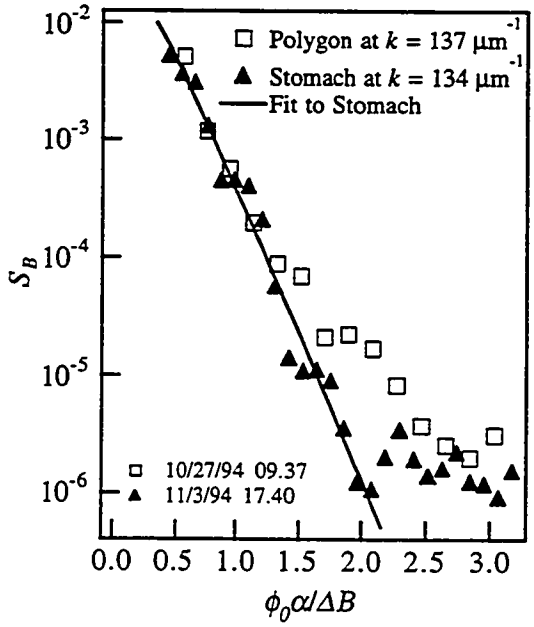

Figure 6.16 Two particular spectra which show the largest difference that could be interpreted as evidence for regular scattering in the Polygon.

Although the shape of S_B for the Stomach and Polygon was the same, the value of $\phi_0\alpha$ for the two cavities was significantly different. In fact, the different typical field scales can be seen directly in the $G(B)$ traces of Figure 6.6. The two cavities were very similar in size and overall shape, but the difference between rounded walls in the Stomach and straight walls in the Polygon was quite clear in the quantum transport properties. This implies that the scattering was dominated by the walls of the cavities and that disorder did not render the shapes indistinguishable.

6.2.2 Spectrum of $G(k)$

The conductance fluctuations as a function of k for the three cavities of sample MBE17S9 are shown in Figure 6.17. The power spectrum S_k was computed using the same procedure as for S_B. Seven segments of 3.8 μm^{-1} were

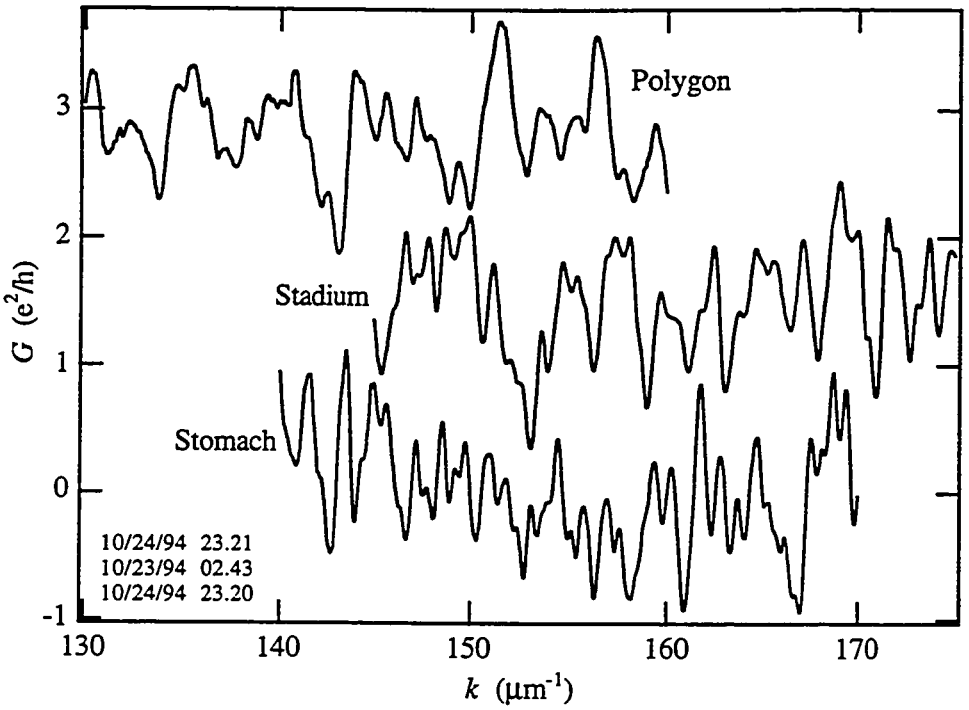

Figure 6.17 $G(k)$ fluctuations for the cavities of sample MBE17S9 at $B = 0$ and $T_{mc} \approx 40$ mK. A third order polynomial fit has been subtracted and the Stadium and Polygon traces are offset upwards.

averaged to produce each spectrum. Since $G(k)$ was nearly a straight line, a background was subtracted. This only affected the spectrum at frequencies below 0.5 μm, and the fits were always done over higher frequencies. $G(k)$ was also measured for the Small and Large Stadia of sample 161L5, but the traces contained an unknown contribution from the long, narrow leads (see Figure 4.5) that made it impossible to study the fluctuations due to the cavities alone.[28] (The contribution from the leads was independent of B for small changes in B because of "flux cancellation" (Beenakker and van Houten, 1991) between the parallel sides of the leads. Therefore it did not interfere with the study of fluctuations in $G(B)$ or weak localization.)

S_k for the Stomach and Stadium cavities is shown in Figure 6.18. The semiclassical form of equation (3.7) provides a good fit over 4 to 5 decades in

[28] The leads near the cavity may contribute to the resistance measured for the stadia because of phase-coherent electron motion into and out of the leads, in the same way that Aharonov-Bohm oscillations from a ring outside the classical current path can be seen in the magnetoresistance of metal wire samples (Umbach *et al.*, 1987).

power and over a frequency range of about $\frac{1}{2}\gamma^{-1}$ to about $2\gamma^{-1}$. Table 6.2 shows a comparison of the experimental values of γ with the values obtained from numerical simulations of classical scattering. The agreement is poor for the ideal shapes, with the experimental values being much larger than expected. This

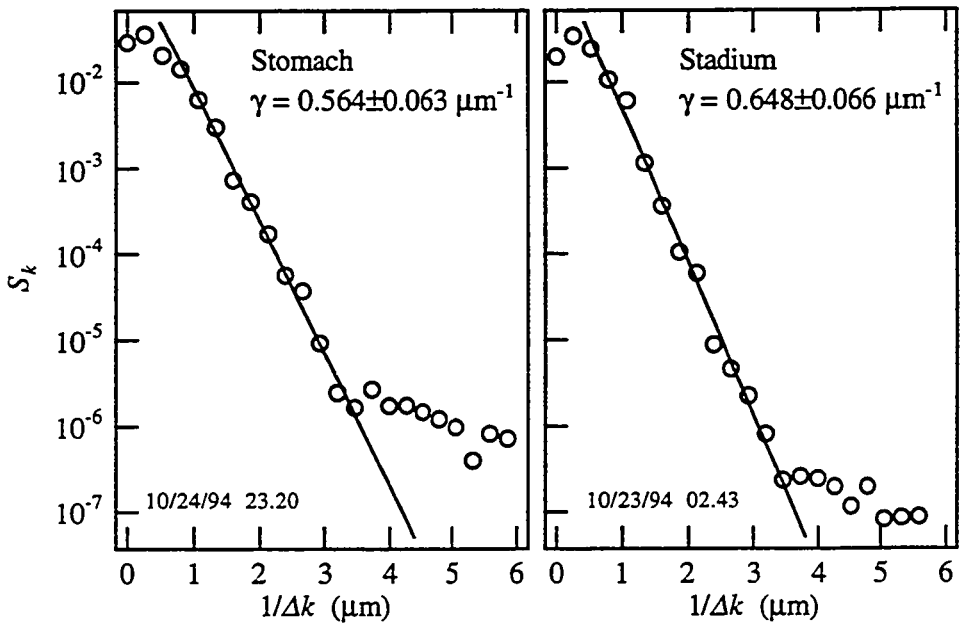

Figure 6.18 S_k (circles) and fits using equation (3.7) (solid lines) for the Stomach and Stadium data of Figure 6.17. (Uncertainties are $\pm 3\sigma$ as determined by the fitting routine.)

Cavity	Experiment	Simulation	
		Ideal	Disordered
Stadium of MBE17S9[a]	0.65 ± 0.07	0.12	0.14
Stomach[b]	0.56 ± 0.06	≈ 0.11	---

Table 6.2 Comparison of γ (in μm^{-1}) from experiment and from classical simulations. [a]Simulation by Lin, private communication, using the dimensions given in Appendix D. [b]Simulation by Baranger, private communication. Baranger's result for a Stomach with $L_{dir} = 4W$ has been extrapolated to the actual Stomach dimensions using the arguments for scaling with cavity size by Jensen, 1991 (see Appendix F).

indicates electrons typically traveled much shorter distances than expected, less than 2 μm in both cavities. The reason for the large discrepancy will be addressed in Chapter 7.[29] When random angles between $\pm\pi/2$ are added to the simulation, γ is nearly unchanged because it is not affected by the circulation tendency described in Section 6.2.1.

S_k for the Polygon cavity is shown in Figure 6.19. Equation (3.7) provides a good fit at low frequency, but it does not fit over as wide a range in power or frequency as for the chaotic cavities. The Polygon spectrum is compared to the Stomach and Stadium spectra in Figure 6.20 using a normalized frequency axis. The Polygon spectrum falls off more slowly than the chaotic cavities for $\gamma/\Delta k > 1.5$. The difference between the Stadium and the Polygon could be partly due to the fact that the Stadium has some direct paths, while the Polygon has none. The comparison of the Stomach and the Polygon does not have this complicating factor. The Stomach and Polygon were measured again on another cooldown and the spectra shown in Figure 6.21 were obtained. In this case there is no significant difference between the two cavities. $G(k)$ at $B = 0$ was also measured during the study of weak localization in the Stomach and the Polygon. The spectra obtained from these traces are shown in Figure 6.22. Again the two cavities appear indistinguishable.

---

[29] The discrepancy between theory and experiment in Table 6.2 is suspiciously close to a factor of 2π. Every effort was made to check both the theoretical expressions leading to equation (3.7) and the numerical analysis used to generate S_k and the fits. It is believed that the comparison shown in the table is valid.

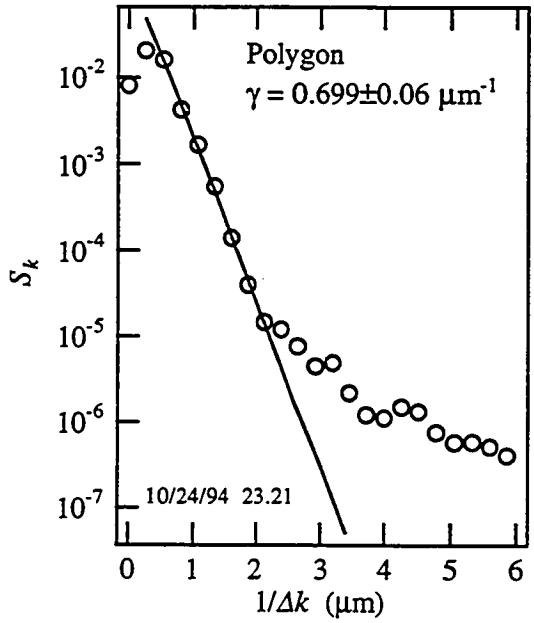

Figure 6.19 S_k for the Polygon data of Figure 6.17.

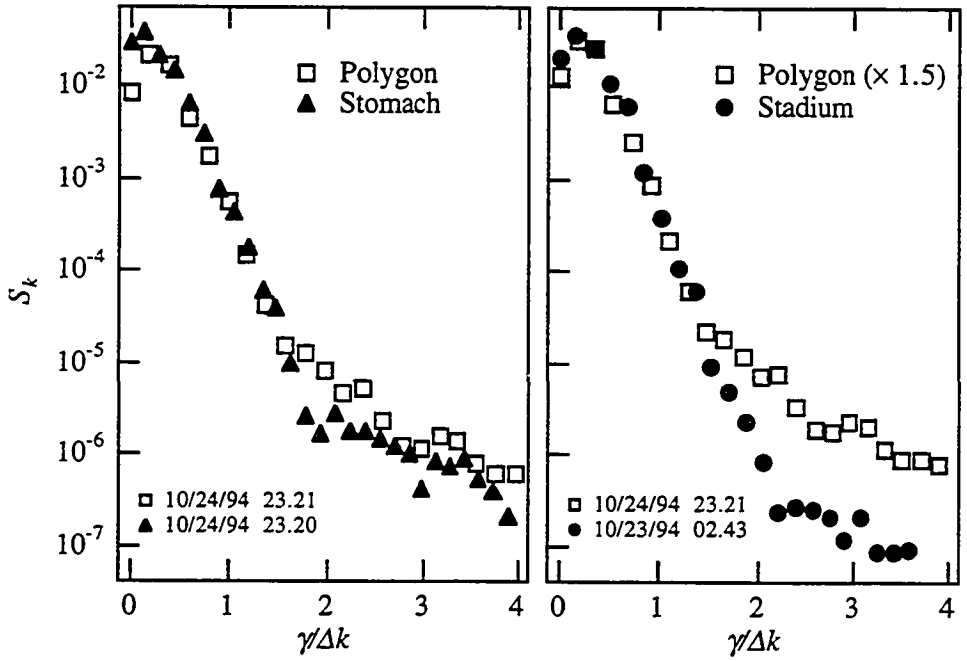

Figure 6.20 Comparison of S_k of the Polygon with S_k of the chaotic cavities from the same sample. The frequency axes have been normalized by γ. The Polygon spectrum on the right has been multiplied by 1.5 to match the amplitude of the Stadium spectrum in the frequency range where they have the same slope.

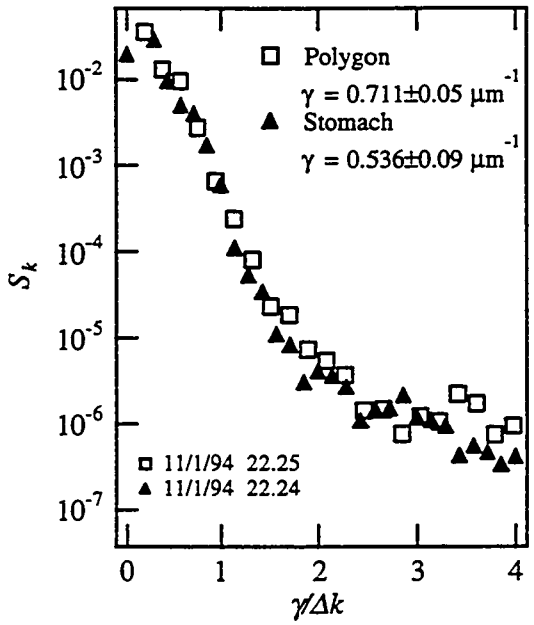

Figure 6.21 S_k for the Polygon and Stomach at $B = 0$ on a different cooldown than Figure 6.20.

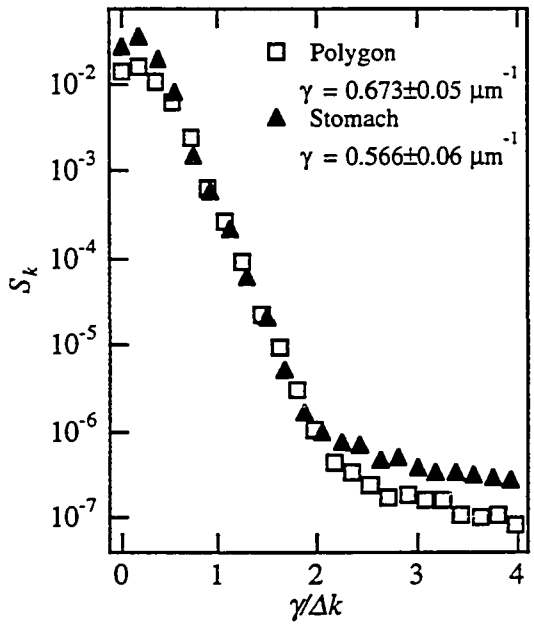

Figure 6.22 S_k for the Polygon and Stomach from $G(k)$ measured during the study of weak localization. The spectra from two traces at $B = 0$ have been averaged together.

6.2.3 Fluctuation Amplitude

The amplitude of the fluctuations can be compared to the predictions of the random matrix theory treatment described in Section 3.5. The "background" must first be subtracted from the traces, which are the same as those used for the study of the power spectra. For $G(k)$ a third order polynomial that was nearly a straight line provided a good fit in all cases. For $G(B)$ each trace was smoothed over a range of about $13\phi_0\alpha$ and then subtracted from the original trace. This procedure was not entirely satisfactory for $G(B)$ because the smoothing range affected the amplitude somewhat, resulting in an uncertainty in the amplitude of perhaps 20%.

Figure 6.23 shows the rms amplitude of the fluctuations in $G(B)$ for all the cavities studied. The predicted amplitude is $0.5e^2/h$. The measured amplitudes are somewhat smaller, presumably because there is still some thermal averaging at an electron temperature of $\approx$ 100 mK. For sample 161L5, the fact that the Small Stadium was much closer to the full amplitude than the Large Stadium is consistent with the fact that T_c is higher in the Small Stadium because the typical trapping time is shorter (see Table 7.1). For each cavity the amplitude was independent of k, in agreement with the predictions of random matrix theory for the "universal" regime where $kW/\pi >> 1$ and $N_\phi << kW/\pi$ (see Section 3.5). This indicates that $N_\phi << kW/\pi$ in the measured cavities. Reports of theoretical and experimental work on the effect of phase breaking on the fluctuation amplitude (Baranger and Mello, 1994b; Clarke *et al.*, 1994; Bird *et al.*, 1994) were recieved during the final stage of preparation of this dissertation. At this point some questions remain about the *quantitative* comparison of experiment and theory in this area. Therefore, a discussion of the effects of phase breaking in the cavities discussed here will be given in a future publication.

Figure 6.24 shows the amplitude of $G(k)$ for the Stomach and Polygon at the values of B used in the study of weak localization. The predicted amplitudes (for chaotic cavities) are $\left(1/\sqrt{2}\right)e^2/h = 0.7e^2/h$ at $B = 0$ and $0.5e^2/h$ at $B \geq \phi_0\alpha$ (see Table 3.1). The measured amplitudes are somewhat smaller, but both cavities show a reduction by a factor of $\approx\sqrt{2}$ when B is increased, as predicted by the theory.

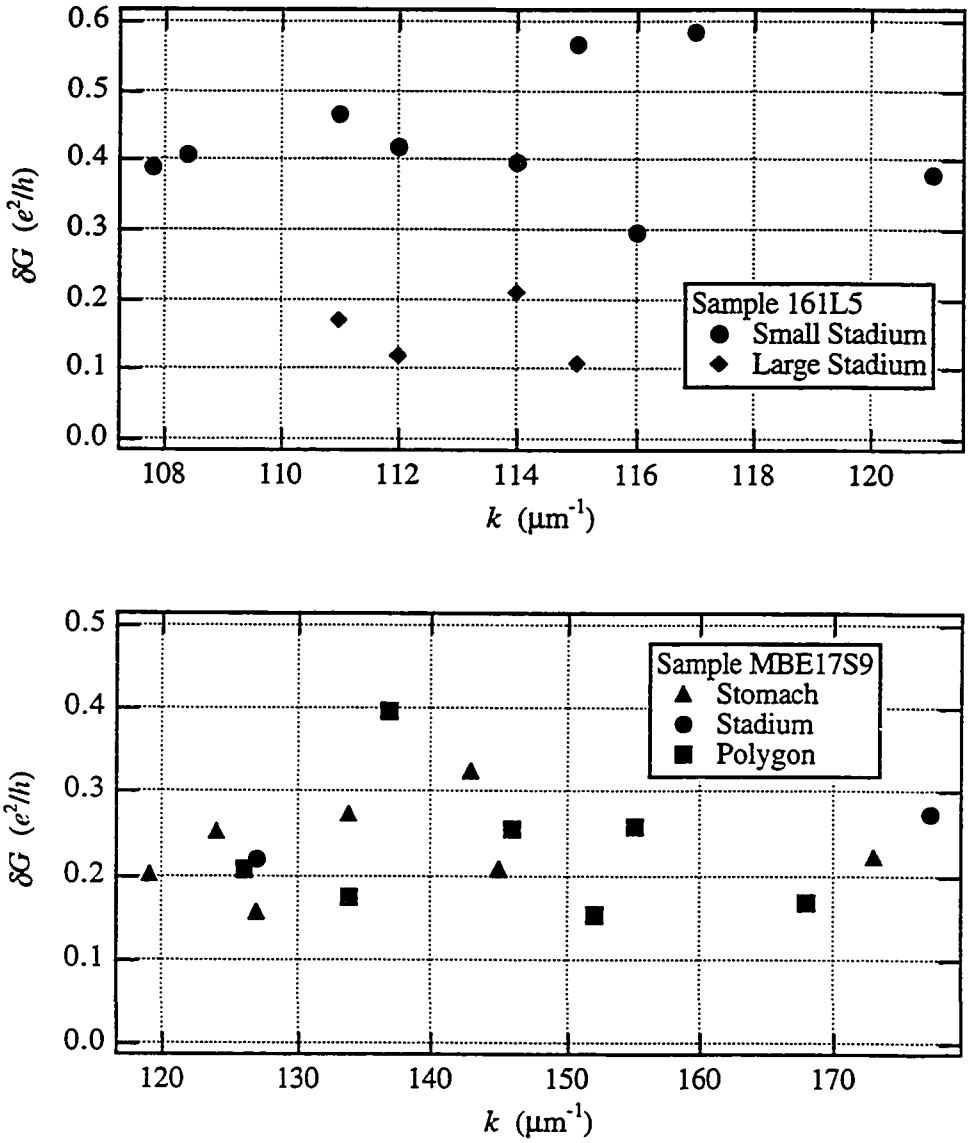

Figure 6.23 Fluctuation amplitude for $G(B)$.

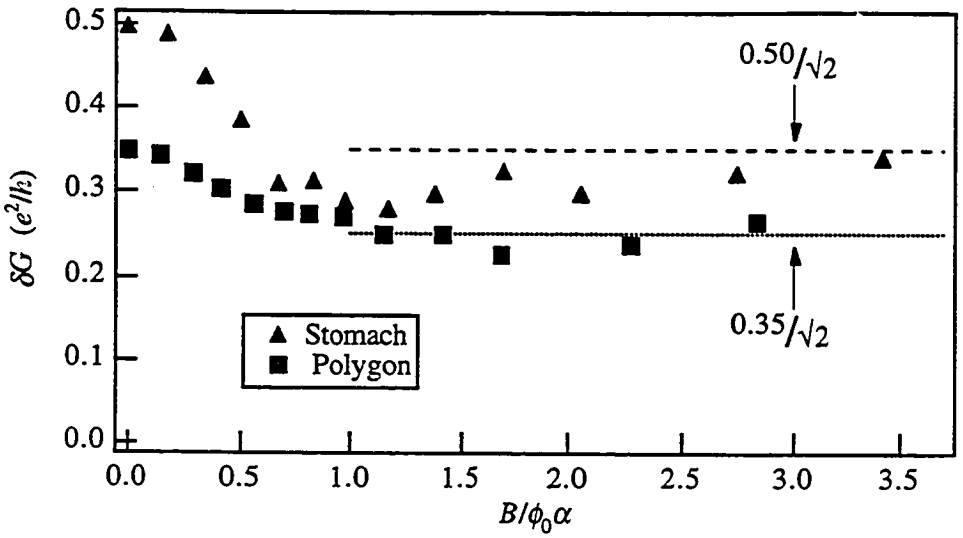

Figure 6.24 Fluctuation amplitude for $G(k)$ measured during the study of weak localization. The dashed (dotted) line shows the expected amplitude after a reduction by a factor of $\sqrt{2}$ for the Stomach (Polygon).

6.3 Weak Localization

The conventional weak localization (WL) effect studied in diffusive transport has as its signature a minimum in conductance centered around $B = 0$. The theory of the effect is based on an average over an ensemble of samples with different impurity configurations but the same macroscopic impurity density. The experiments are done using samples several times larger than the phase coherence length; these samples are effectively several members of an ensemble measured simultaneously. The samples always show the expected conductance minimum at $B = 0$.[30] In contrast, a ballistic cavity that is smaller than the phase coherence length represents a single member of an ensemble and does not necessarily behave as the ensemble average. This explains why a *maximum* in $G(B)$ at $B = 0$ was sometimes observed, as shown in Figure 6.25. Most $G(B)$ traces showed a pronounced minimum at $B = 0$ (see Figure 6.6), but a very small minimum or a maximum was observed several times. WL was studied in a long-sided stadium cavity by Berry *et al.*, 1994a and 1994b, but a maximum in $G(B)$ at $B = 0$ was not

[30] Spin-orbit scattering is ignored here because it is negligible in the GaAs 2DEG at the low densities typical of high mobility heterostructures (Dresselhaus, Papavassiliou, and Wheeler, 1991).

reported, presumably because the measurements were done only at temperatures above 0.4 K where thermal averaging was important. In order to study the ensemble-averaged WL, some way of accessing different members of the ensemble of each cavity must be available. In the samples discussed here, the gate voltage provides this capability.

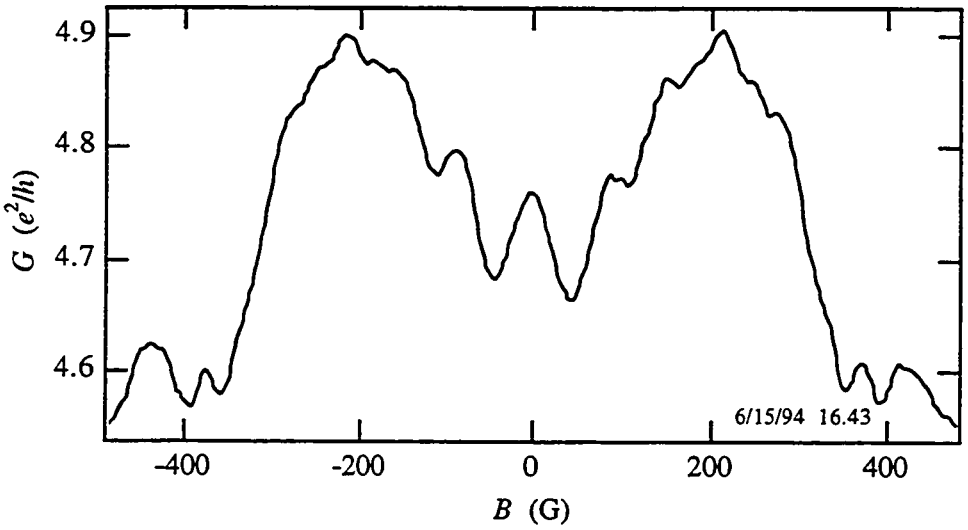

Figure 6.25 An example of $G(B)$ showing a maximum at $B = 0$ instead of the minimum shown by the ensemble average.

To obtain the WL for many members of the ensemble at once, $G(k)$ was measured at several values of B between 0 and a few times $\phi_0\alpha$. The conductance change $\Delta G(k,B) \equiv G(k,B) - G(k,0)$ is shown in Figure 6.26 for the Stomach cavity at several values of B. This plot explicitly shows the variation in the WL of about 25 different members of the ensemble, each labeled by their Fermi wavevector (the range of k is about 25γ). For some members the effect is large and for others it is small, and both positive and negative effects can be seen. The energy-averaged WL is simply the mean of ΔG over the entire measured range of $k \in [119,143]$ μm^{-1} ($kW/\pi \in [7.6,9.1]$), and it is shown in Figure 6.27. $\langle \Delta G \rangle_k$ is positive, as expected, and a field of order $\phi_0\alpha$ produces a conductance change of order e^2/h. Baranger, Jalabert, and Stone (1993a) have calculated the average WL from numerically-generated $G(k)$ traces using the same procedure just described. Their result for a Stomach cavity similar to the measured one is compared to the

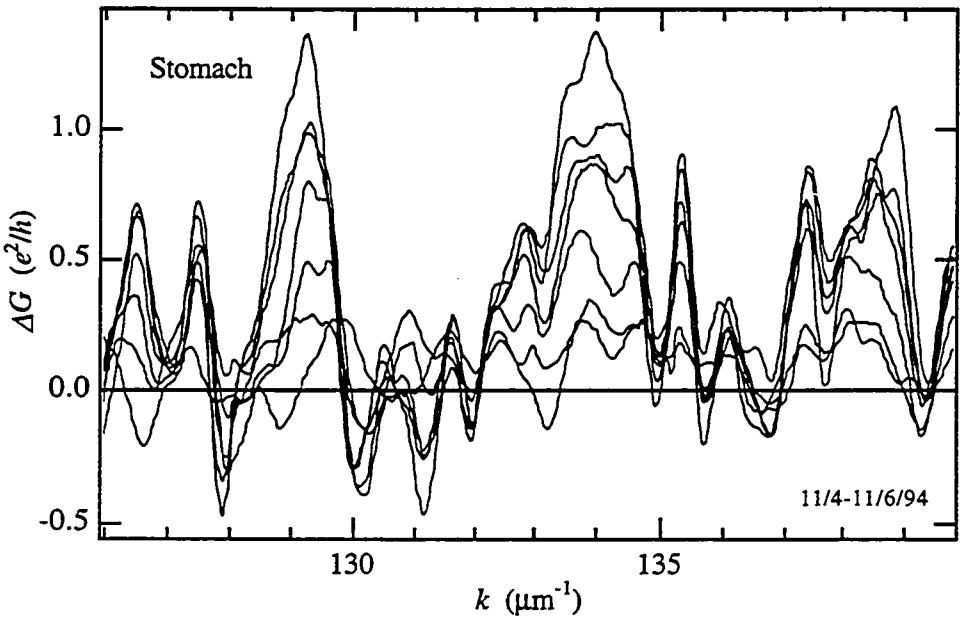

Figure 6.26 $\Delta G(k,B)$ of the Stomach cavity for B = 5, 10, 15, 20, 24, 28, and 34 G. Generally, the curves for small B are close to the line $\Delta G = 0$ and those for large B are farther away in both the positive and negative directions.

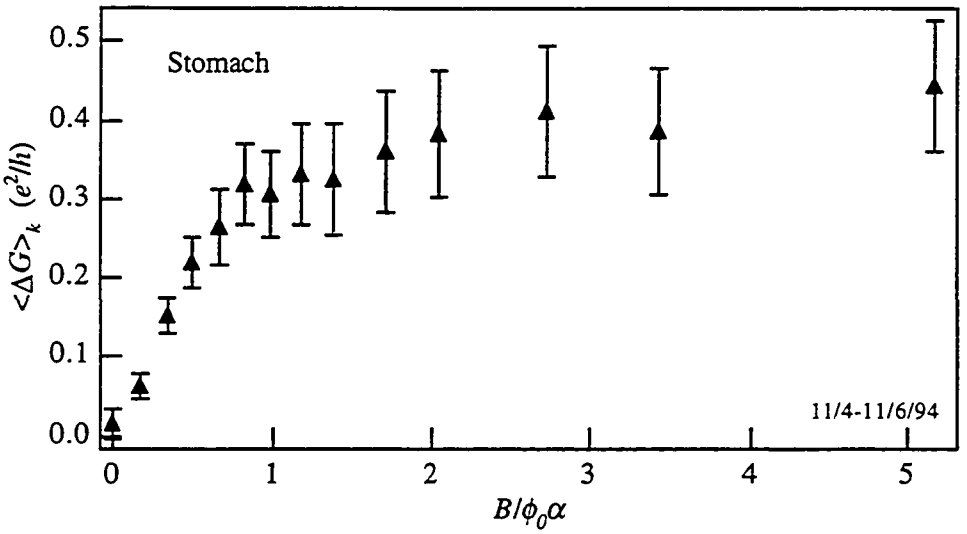

Figure 6.27 Mean of $\Delta G(k,B)$ over the range $k \in$ [119,143] μm^{-1} for the Stomach. This range is about 45γ and, assuming a lead width of 200 nm, corresponds to $kW/\pi \in$ [7.6,9.1]. The point at $B = 0$ is the difference between two consecutive $G(k)$ traces at $B = 0$.

experimental result in Figure 6.28a. With no adjustable parameters (since $\phi_0\alpha$ was determined experimentally), the agreement is quite good for $B \leq 2\phi_0\alpha$. Figure 6.28b shows the WL for the Small Stadium over the range $k \in [108.5,121]$ μm^{-1} ($kW/\pi \in [5.2,5.8]$), which also agrees quite well with the numerical result for the Stomach.

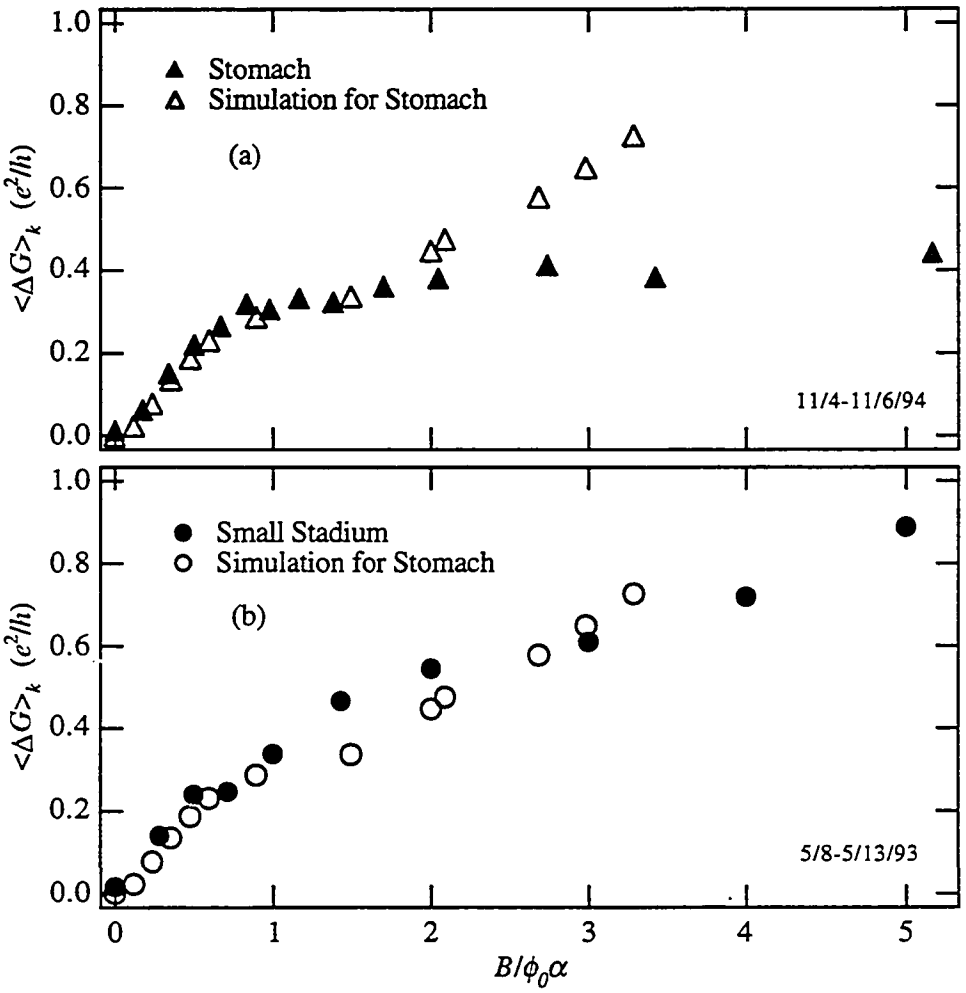

Figure 6.28 Comparison of experimental and numerical results for the energy-averaged WL. (a) The experimental result for the Stomach (same data as Figure 6.27) is compared to the result of Baranger *et al.* for a Stomach cavity with $L_{dir} = 4W$ simulated over the range $kW/\pi \in [4,11]$. The error bars for the simulation are approximately the same size as the markers in the plot. (b) The experimental result for the Small Stadium is compared to the same simulation as in (a). The error bars for the Stadium are similar to those shown in Figure 6.27 for the Stomach.

The WL was also measured for the Polygon. $\Delta G(k,B)$ is shown in Figure 6.29 for several values of B. As for the chaotic cavities, the WL at a particular value of k can be positive or negative. The energy-averaged result for the Polygon is shown in Figure 6.30, along with a simulation for the same shape. The simulation shows the expected behavior for $B \approx 0.1\phi_0\alpha$ to $B \approx \phi_0\alpha$, but the measured WL saturates at $B \approx \phi_0\alpha$. Figure 6.31 shows the behavior of the Stomach and Polygon at small B, along with the simulation for the Stomach for reference. The Polygon is clearly closer to the prediction for a chaotic cavity than for a regular cavity.

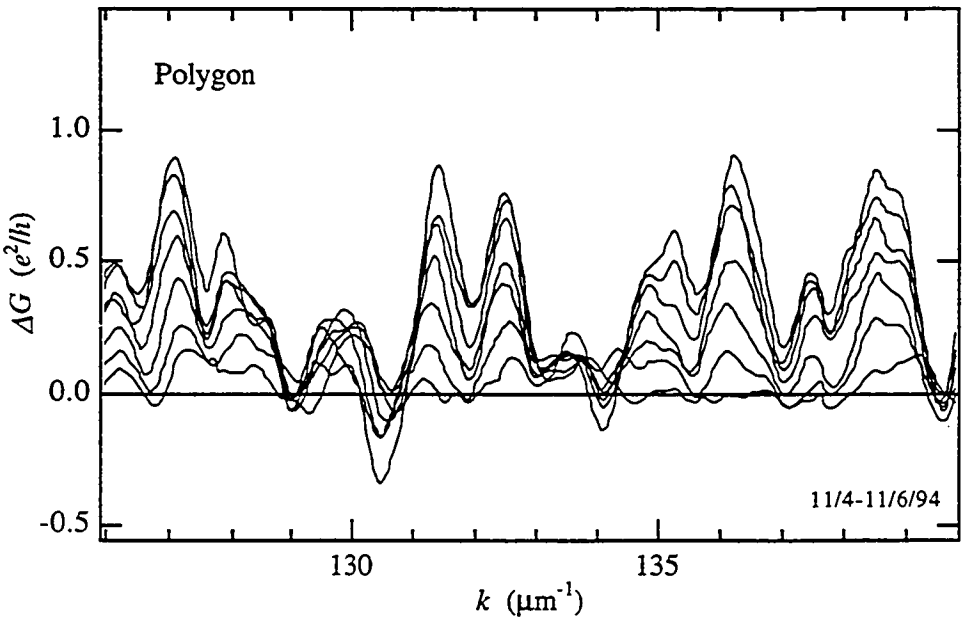

Figure 6.29 $\Delta G(k,B)$ of the Polygon cavity for B = 5, 10, 15, 20, 24, 28, and 34 G. Generally, the curves for small B are close to the line $\Delta G = 0$ and those for large B are farther away in both the positive and negative directions.

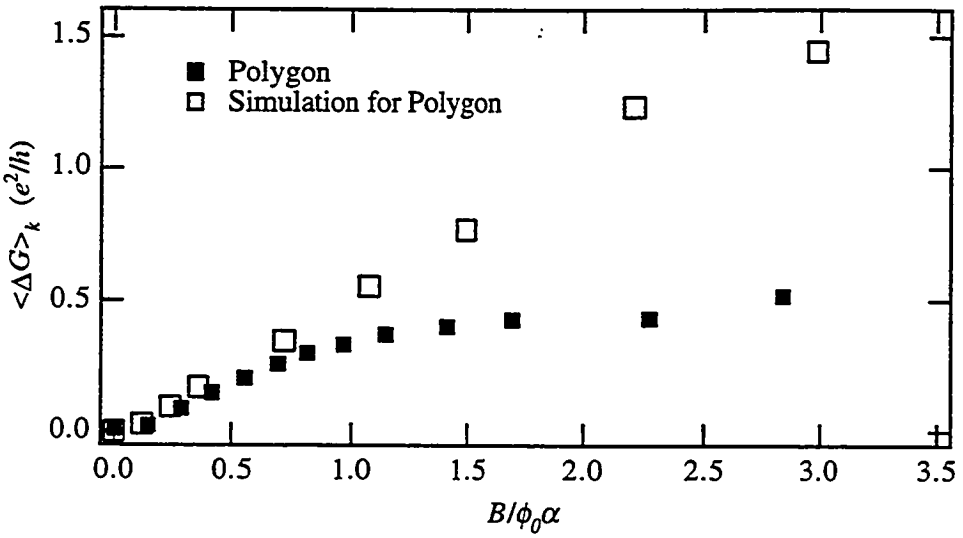

Figure 6.30 Mean of $\Delta G(k,B)$ over the range $k \in [126,155]$ μm^{-1} for the Polygon. This range is about 45γ and, assuming a lead width of 200 nm, corresponds to $kW/\pi \in [8.0,9.9]$. The point at $B = 0$ is the difference between two consecutive $G(k)$ traces at $B = 0$. The simulation is for a Polygon with $L_{dir} = 4W$ over the range $kW/\pi \in [4,11]$.

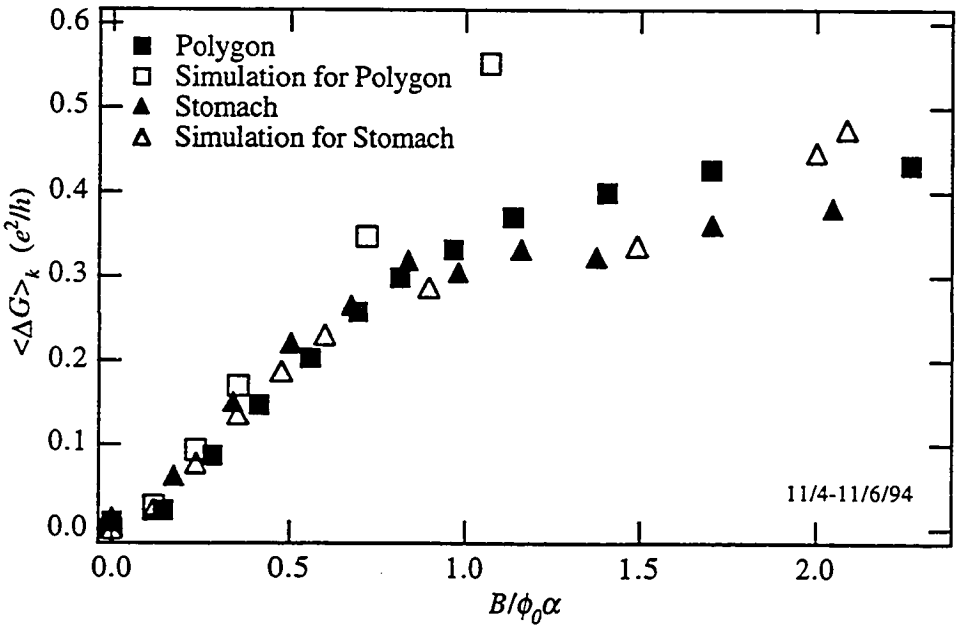

Figure 6.31 Expanded view of the WL behavior of the Stomach and Polygon at small B.

7

DISCUSSION AND CONCLUSIONS

The results presented in Chapter 6 are summarized below and in Table 7.1 at the end of this chapter.

- $G(B)$ and $G(k)$ for all cavities showed fluctuations comparable to the full amplitude predicted by random matrix theory. The amplitude of $G(k)$ was sensitive to time-reversal symmetry as expected. The weak localization (WL) amplitude agreed very well with a zero-temperature simulation. These facts indicate that the data reflect the true quantum interference behavior of the cavities, with weak thermal averaging.
- Equations (3.7) and (3.8) provided good fits to the spectra S_B and S_k of the chaotic cavities over several decades in power and an appropriate range in frequency. This indicates that the observed fluctuations were consistent with the semiclassical predictions, although the fits were not so precise that other functional forms could be ruled out.
- $\phi_0\alpha$ was approximately independent of k for all cavities, indicating that the cavity sizes did not change with k, as required for the study of energy-averaged quantities.
- The comparison of the experimental values of $\phi_0\alpha$ and γ with the values predicted by simulations indicated that the electrons typically enclosed much less area and travelled much shorter distances inside the cavity than expected for the ideal shapes with no disorder. For $\phi_0\alpha$ of the three stadia, adding a simple model of disorder to the simulations improved the agreement with experiment.
- $\phi_0\alpha$ was significantly different in the Stomach and Polygon cavities. This implies that disorder did not mask the distinction between curved and straight walls in the two cavities, which were otherwise very similar.
- The energy-averaged WL, constructed explicitly from measurements of the effect at many different energies, was in very good agreement with a simulation for a Stomach cavity.

- Some evidence for regular scattering in the Polygon was observed, but it was not robust. A difference in S_B was seen only for one particular value of k, and not in the average spectrum. A small difference in S_k was seen only for data from one of three measurements of the fluctutations in $G(k)$. The WL effect in the Polygon was nearly identical to that in the Stomach and Small Stadium.

Before going on to discuss these results, two other experimental investigations of chaotic scattering in ballistic microcavities (Marcus *et al.*, 1992 and Chang *et al.*, 1994) will be described. Both of these studies used cavities made from a GaAs 2DEG. For comparison with these two other studies, the basic parameters of the samples measured at Yale are as follows.

Cavity size: ≈ 1 μm
Bulk mean free path: 5.5 μm (161L5) or 19.5 μm (MBE17S9)
Electron temperature: 100 to 200 mK
kW/π: 5 to 9

Marcus *et al.* measured the fluctuations in $G(B)$ for a long-sided stadium and a circle. The cavities were made using the split-gate technique, so the electron density could not be varied independent of the cavity size. The cavities were about one micron across, the mean free path in the bulk 2DEG was 2.6 μm, the electron temperature was around 100 mK, and the gate voltages were adjusted so that $kW/\pi \approx 1$ to 3 in each lead. S_B was reported for the case of $kW/\pi \approx 3$, and it showed the same slope for both cavities at low frequency, but S_B for the circle fell off more slowly at higher frequency. The spectra were qualitatively similar to those shown in Figure 6.16, but with a somewhat larger quantitative difference. Because the cavity size depended on the gate voltage, an energy average could not be obtained, but similar behavior was seen in a second sample having a nearly identical pair of cavities. When the values of $\phi_0\alpha$ for the two stadia were compared with classical simulations (Lin, Delos, and Jensen, 1993), it was found that the electrons enclosed much less area than expected for the ideal shape. When simulations including random angles were done, they produced agreement with the experiment for random angles distributed over $\pm\pi/2$. Classical simulations of the circle cavity with random angles of the same size showed that the distribution of areas was exponential, implying that scattering in the circle was no longer regular, but chaotic. The experimental difference in S_B could therefore be interpreted as reflecting the difference between the tendency for circulating trajectories in the circle and the lack

of this tendency in the long-sided stadium. However, given the relatively crude nature of this model of disorder, it is not clear that this is the only possible interpretation. Overall, the results of Marcus *et al.* suggest a difference between chaotic and regular cavities, but do not constitute conclusive evidence.

Chang *et al.* measured the WL for a long-sided stadium and a circle. To achieve an effective average over disorder configurations, 48 nominally identical copies of each shape were measured simultaneously. The cavities were defined using low voltage reactive ion etching, which is similar to the shallow wet etch described in Section 4.3.2. There was no gate, so the electron density could not be changed. The cavities were about one micron across, the mean free path in the bulk 2DEG was 17 μm, the electron temperature was about 50 mK, and $kW/\pi \approx 4$ in each lead. The lineshape of $\langle G(B) \rangle_{48}$ for the stadia was Lorentzian, as expected for a chaotic cavity, and the lineshape for the circles was much more linear. In fact, the experimental difference seen at finite temperature and with some disorder appears to be more striking than the difference seen in the simulations done at zero-temperature and for ideal cavities. Because the fluctuations disappeared in the average over many copies of each cavity, $\phi_0\alpha$ could not be determined from the fluctuation power spectrum.

The results of Marcus *et al.* and Chang *et al.* indicate that the conductance of circular ballistic cavities can show a difference from the behavior seen in chaotic shapes. They do not indicate whether the experimental chaotic cavities can display values of $\phi_0\alpha$ and γ close to those found by classical simulations in ideal cavities.

If the values of γ are ignored for the moment, a reasonably coherent picture of the results for $\phi_0\alpha$ shown in Table 7.1 can be proposed. The Stomach cavity agrees well with the ideal simulation, indicating that there was no gross distortion of the cavity shape by disorder. The Polygon had a somewhat higher field scale, which is consistent with the existence of flux cancellation (see Beenakker and van Houten, 1991) from the short lengths of parallel sides. In the three stadia, the tendency for trajetories to circulate was destroyed by moderate disorder, causing electrons to enclose about 2.5 times less area than expected for the ideal cavities. The important aspect of the experiments that this picture does not explain is the lack of evidence for regular scattering in the Polygon. Could there be disorder weak enough to have a negligible effect on $\phi_0\alpha$ in the Stomach, but strong enough to destroy the power law distribution of areas in the Polygon? Numerical simulations with realistic disorder could probably answer this question.

Further evidence for moderate disorder in sample MBE17S9 comes from a short wire, estimated to be 1.9 μm by 0.21 μm with 85 nm of depletion, that was fabricated along with the cavities. $G(k)$ for this wire showed no evidence of quantized conductance at multiples of $2e^2/h$. Ismail *et al.*, 1991 saw good quantization in similar wires fabricated with the shallow wet etch technique from a wafer having a bulk mean free path of about 5 μm. The reasons for increased disorder compared to structures fabricated by other researchers are not known.

Turning to the results for γ, it is more difficult to construct a consistent picture. The typical length, γ^{-1}, was less than 2 μm, implying that the electrons travelled only about twice across each cavity before escaping. The simulation of the stadium shape with random-angle disorder did not reproduce the measured value of γ because γ is not as sensitive to circulation as $\phi_0\alpha$. Furthermore, the values of T_c inferred from γ (see the caption of Table 7.1) imply that the quantum interference probably should have no temperature dependence at $T = 200$ mK, and yet a clear temperature dependence was seen in all three cavities of sample MBE17S9.

One possible reason for the large values of γ in the Stomach and Polygon has been pointed out recently by Baranger (private communication). The stoppers of these cavities extend further toward the center of the cavity than those of the shapes used in the simulations. This may cause a large fraction of the entering electrons to be reflected back into the lead after just one bounce from the stopper. This would reduce the typical length, but would not affect the typical area, since such backscattered trajectories would enclose little or no area. This picture does not explain why the Stadium also had a very short typical length.

Another mechanism which could cause large values of γ is very strong phase breaking, *i.e.*, a phase coherence length ℓ_ϕ of order 2 μm. Electrons traveling longer distances inside the cavities would effectively be removed from the cavity as far as quantum interference effects are concerned. This would destroy the fluctuations from the longer paths, and make S_k steeper than it would be if all the trajectories that make up the expected distribution of lengths were contributing. However, such a short ℓ_ϕ would imply that the fluctuations and the WL should be much smaller than predicted for $T = 0$, in contradiction with the observed effects. It would also contradict the expectation that ℓ_ϕ can be estimated from WL experiments on narrow wires, which show good agreement with a quasi-1D theory of phase breaking (Kurdak *et al.*, 1992). The phase coherence time from this theory implies a ballistic phase coherence length ($\ell_\phi = v\tau_\phi$) of about 70 μm at $T = 100$ mK and 11 μm at $T = 1$ K for sample MBE17S9.

Despite the unresolved issues discussed above, the experiments described here show that the theory of chaotic scattering is very useful in understanding quantum electron transport in the ballistic regime. This is an important addition to our understanding of mesoscopic physics. Perhaps experiments of this type will allow mesoscopic physics to return the favor by helping to resolve some of the current issues in the field of quantum chaos. At the present time, however, it appears that microstructures made from the GaAs 2DEG are still too imperfectly made and imperfectly understood to provide conclusive tests.

Cavity	Dimensions (μm)	Experimental $\phi_0\alpha$ (G)	Experimental γ (μm^{-1})	Experimental T_c (K)	Simulation - Ideal $\phi_0\alpha$ (G)	Simulation - Ideal γ (μm^{-1})	Simulation - Ideal T_c (K)	Simulation - Disordered $\phi_0\alpha$ (G)	Simulation - Disordered γ (μm^{-1})	Simulation - Disordered T_c (K)
Small Stadium of 161L5	R = 0.28 W = 0.15	60.6	---	---	23	0.27	0.40	51	---	---
Large Stadium of 161L5	R = 0.58 W = 0.15	9.2	---	---	3.5	0.073	0.11	9.9	---	---
Stadium of MBE17S9	R = 0.54 W = 0.20	15.3	0.65	1.2	5.9	0.12	0.22	14	0.14	0.26
Stomach of MBE17S9	L_{dir} = 1.4 W = 0.21	27.9	0.56	1.0	32	0.11	0.20	---	---	---
Polygon of MBE17S9	L_{dir} = 1.3 W = 0.21	35	0.70	1.3	---	---	---	---	---	---

Table 7.1 Summary of the characteristics of the five cavities studied in this work. The temperature scale $T_c \equiv \hbar\theta/k_B$ was found from the measured value of γ using $\theta = v\gamma$ ($v = \hbar k/m^*$ is the Fermi velocity) with k = 114 μm^{-1} for 161L5 and k = 140 μm^{-1} for MBE17S9.

Appendix A

$GaAs/Al_xGa_{1-x}As$ Heterostructures

MBE 1161, grown by Dr. Robert N. Sacks

200 Å	NID GaAs
400 Å	n - $Al_{0.24}Ga_{0.76}As$ 1×10^{18} Si/cm^3
300 Å	NID $Al_{0.24}Ga_{0.76}As$
1.0 μm	NID GaAs
	20 times (50 Å AlAs / 50 Å GaAs)
100 Å	NID GaAs
	Semi-insulating GaAs substrate

Bulk parameters at T = 2 K: $n = 2.6 \times 10^{11}$ cm^{-2}
$\mu = 0.65 \times 10^6$ cm^2/V-s
=> Mean free path = 5.5 μm

MBE17, grown by Ms. Hadas Shtrikman

100 Å	NID GaAs	
200 Å	n - $Al_{0.37}Ga_{0.63}As$	3.3 x 10^{18} Si/cm^3
350 Å	NID $Al_{0.37}Ga_{0.63}As$	
≈ 10 Å	δ-doped layer	4.0 x 10^{18} Si/cm^3
350 Å	NID $Al_{0.37}Ga_{0.63}As$	
1.0 μm	NID GaAs	
500 Å	NID $Al_{0.37}Ga_{0.63}As$	
	25 times (100 Å $Al_{0.37}Ga_{0.63}As$ / 50 Å GaAs)	
2000 Å	NID GaAs	
	Semi-insulating GaAs substrate	

Bulk parameters at T = 4.2 K: $n = 3.5 \times 10^{11}$ cm^{-2}
$\mu = 2.0 \times 10^6$ cm^2/V-s
=> Mean free path of 19.5 μm

Small-angle scattering length ≈ 0.5 μm
(J. Pieper, private communication)

Note: Wafer MBE18, grown under nearly identical conditions to MBE17 and having similar bulk parameters, showed very nonuniform etching. Many deep pits, of order 0.1-0.5 μm in size, occurred in a density of one or more per square micron. This made the wafer unsuitable for fabricating microstructures.

Appendix B

Fabrication Notes

Photolithography

General:

A small chip size of 3.5 mm by 3.5 mm was used to conserve the limited amount of high mobility heterostructure. With such small chips, photoresist (PR) beads at the edges and corners were a major problem. The NNF mask set a perimeter clean pattern that was designed to remove the PR beads by exposing and developing them. In practice, the beads were so thick that more than one exposure was needed and by the time the perimeter was clean the center of the sample had spent so much time in the developer that it's performance suffered. This problem was solved by simply scraping the corners of the sample with a razor blade immediately after spinning the PR.

Shipley 1470 PR was used for the etch steps and Hoechst AZ 5218E was used in an image reversal process for liftoff steps. The AZ 5218E was also tried as an etch mask but it did not adhere well enough.

PR exposure was done with the HTG mask aligner. The small chips could not always be pressed flat against the mask plate even when the chuck float was used. This problem was solved by placing a clean 2-inch Si wafer on the chuck, pressing it against the mask, floating the chuck so it was parallel to the mask, and then releasing the float to fix the chuck. The sample was then placed on the chuck and brought into contact with the chuck float off. This greatly improved the uniformity of contact over the chip.

All PR developing steps were done with Shipley Microposit 351, 1:5 in DI water, T ≈ 21 C.

All baking was done on a hotplate.

Standard cleaning procedure:

Trichloroethane, acetone, methanol, each ~ 5 s in ultrasonic and then ~ 60 s soaking.

Blow dry with N_2.

Bake at T > 100 C, ~ 3 minutes to dehydrate.

Black spots of sizes up to tens of μm that are not removed by ultrasonic cleaning are probably pits in surface from MBE growth. They cannot be removed. They will grow slightly during the mesa etch step.

Mesa Etch:

Clean and dry. Glue to glass slide (#2 thickness is best) with PR, bake 90 C, 2 min. Spin cool ~ 40 s.

Spin Shipley 1470 PR, 6000 rpm, 40 s.

Scrape PR from corners of sample.

Softbake 90 C, 5 min.

Expose pattern with ≈ 30 mJ/cm^2 at 365 nm.

Develop 60–90 s.

Optional: O_2 plasma (1 kV, 1 mA, 5 min.) or RIE (60 W, 60 mTorr, 30 s).

Bake 110 C, 10 min.

Mix etch solution: 5 ml of 30% NH_4OH, 1 ml of 30% H_2O_2, 1000 ml of H_2O, 5 drops of Fischer FL-70 detergent.

Wait until etch reaches T ≈ 21 C. Hold sample with locking forceps and stir gently while etching. Etch rate depends on layer structure of wafer.
Strip PR in acetone.
Measure etch depth with Dektak.

Ohmic Contacts:
Clean and dry. Glue to glass slide (#2 thickness is best) with PR, bake 90 C, 2 min. Spin cool 40 s.
Spin AZ5218 resist at 6000 rpm, 40 s.
Softbake 90 C, 5 min.
Expose pattern with ≈ 30 mJ/cm^2 at 365 nm. (Lower dose gives more undercut but rounds corners and makes holes bigger than design size. If contact is not good over pattern region because chuck is not parallel to mask or perimeter is not clean, dose will need to be somewhat higher.)
Bake 115 C, 100 s. (If in doubt, bake harder.)
Flood expose ~ 500 mJ/cm^2.
Develop 45 - 60 s.
Examine: Undercut should be visible as a faint but distinct double line around all cleared areas, but liftoff will usually work even if undercut is not that strong. The 10 μm holes should have PR between them that is almost unchanged in color; corners should not be too rounded. Circular defects in PR may be seen, but they don't seem to affect liftoff.
O_2 plasma (1 kV, 1 mA, 5 min.) or RIE (60 W, 60 mTorr, 30 s).
Bake 130 C, 10 min. (Softer bake risks cracking during evap.)
Examine: Should look the same as before plasma, or maybe slightly darker at edges of cleared areas.
Strip oxide in 3% NH_4OH in H_2O with 1 drop of FL-70 detergent in ≈ 50 ml; soaking for 10 s. No DI rinse. Blow and spin dry, then immediately place in evaporator and pump down. (10% NH_4OH for 30 s sometimes attacked PR.)
Evaporate 400 Å Ni, 400 Å Ge, 1500-2500 Å Au.
Liftoff in acetone. If it does not come off easily let it sit for an hour or overnight. If it still won't come off, try brief ultrasonic.
RTA at 425 C, 60 s, N_2 flowing.
Examine: Contacts should be dull yellow, not bright yellow like just after evaporation. Any bubbles in contacts should be small and uniformly distributed. Surface should look rough, but a mottled look is not good.

Ti/Au Wiring and Alignment Marks:
Same photolithography as for Ohmic Contacts.
Examine after develop: Undercut should be visible as a distinct double line around all cleared areas. The 4 μm alignment marks should be separated by PR of almost unchanged color; corners should not be too rounded (the mask itself is slightly rounded).
Same O_2 plasma, hard bake, and oxide strip as for Ohmic Contacts.
Evaporate 50 Å Ti and enough Au to cover depth of mesa plus ohmic metal.
Liftoff in acetone.

E-Beam Lithography
Clean and dry.
Place sample on spinner chuck with center of pattern over center of chuck.

Put a few drops of PMMA on and spin immediately. (Otherwise sample will get stuck to chuck.) Put on two or three more drops right after starting spin.
Push sideways to loosen before lifting from spinner chuck (this applies to hotplate also).
Check in microscope; try again if PMMA is not uniform over area to be exposed.
For etch step: Spin 5% 150k m.w. PMMA in MIBK at 3000 rpm, 40 s, bake at 170 C overnight (≈ 18 hours). A softer bake risks poor adhesion of PMMA and problems during etch step. Dose ≈ 185 $\mu C/cm^2$.
For liftoff step: Spin 5% 150k m.w. PMMA in MIBK at 3000 rpm, 40 s, bake at 170 C, 1 hour. Spin 2% 950k m.w. PMMA in MIBK, ramping from 3000 rpm to 8000 rpm in about 1 s, spin 40 s, bake at 170 C, 1 hour. Dose ≈ 250 $\mu C/cm^2$.

Other steps

Dicing a wafer:
Spin and bake a thick coat of PR on front of wafer.
Mark back side of wafer with pencil. Best size for 24 pad masks is 3.5 mm X 3.5 mm.
Scribe lightly along pencil marks, using a clean edge as a guide, e.g. a plastic ruler.
Break over a clean edge.
Rinse in DI to remove particles.
Strip PR in acetone.

Measuring at Probe Station:
Putting LN2 around chuck condenses all kinds of crap onto the sample. It will usually come off in the standard solvents with ultrasonic, but sometimes some of it stays. Clean the sample right away to have the best chance of getting it off.

Cleaning Masks:
Blow off loose chunks with full pressure N2 nozzle next to HTG.
Soak in acetone to remove PR. A few seconds of ultrasonic won't hurt the Cr features.
Wash thoroughly with DI, blow dry immediately.
If there is spotting from droplets of DI, squirt with IPA after DI wash and then blow dry.

Appendix C

Optical Lithography Masks from NNF

When the transition was made to 24-pin headers, a new set of masks was needed. The JEOL EBL system worked conveniently with a 100 μm square field or smaller, but getting 24 leads to converge to a 100 μm square required smaller features than could be made reliably in the Yale darkroom. Fortunately, the National Nanofabrication Facility at Cornell University was only a long drive away. The masks were made using NNF's optical pattern generator, which can create features down to about 2 μm. Smaller features can be created by the ebeam mask writing system, but there is usually a long waiting list.

Fabricating the masks was straightforward, thanks to the help of Garry Bordanaro at NNF. The more difficult part was getting the mask designs into a format that NNF could use. The CAD system at NNF requires files in GDS format, which is not one of the standard graphics formats used by other CAD software outside the microelectronics industry. NNF has a method of converting DXF format to GDS, but only if a limited set of CAD operations were used to make the DXF file. To avoid confusion, the L-Edit program was purchased because it does create GDS format. When the designs were finished, Mike Rooks at NNF helped ensure that the NNF CAD system could interpret the L-Edit GDS files properly. Several changes were made while at NNF, and it was much easier to make these changes with L-Edit than to learn the NNF CAD system.

L-Edit is meant to be used for designing masks, and it did the job nicely once a few quirks in the Macintosh version were smoothed out. However, it is not useful as a general purpose CAD program for two reasons. First, it cannot create files in any of the more common formats needed for export of high quality graphics to other software. Second, its own printing capabilities are quite limited: it does not print in color and its shading and fill patterns are difficult to use effectively. But if you want the ability to design in GDS format, it's the only inexpensive way to get it.

The 24-pad masks contain four versions of the overall layout shown in the top of Figure 4.3. Two versions have metal film leads from the bonding pads to the 100 μm square and two have leads made of 2DEG. One pattern of each lead type has bars of 2DEG shorting 23 of the pads together, with the 24th pad connected to metal gates which cross each shorting bar. The idea is that with no

voltage on the gate, the completed sample could be handled without risk of damaging the microstructures by static discharge. After mounting the sample on the cryostat and cooling it down, a large negative voltage on the 24th pad would turn off all the shorting bars, allowing the microstructures to be measured. The four patterns are summarized in the table below. Only pattern 1 was used for the chaotic scattering samples.

Pattern	Leads	Shorting Bars
1	Metal film	No
2	2DEG	No
3	Metal film	Yes
4	2DEG	Yes

Appendix D

Sample Profiles

161L5

Wafer: MBE 1161

Large scale fabrication: Emulsion masks made in Yale darkroom
1. Mesa etch: Approximately 2000 Å
2. Ohmic contacts: 200 Å Ni / 200 Å Ge / 800 Å Au, RTA at 450 C, 60 s in N_2
3. Fresh metal over ohmic contacts for wire bonding: 200 Å Ti / 1000 Å Au
4. Pads to isolate mask/gate from ohmic contacts: 1500 Å SiO
5. Large mask/gate: 500 Å SiO / 500 Å Cr / 1000 Å Au

Microstructure fabrication:
1. Small mask/gate: 300 Å Ti / 1200 Å Au
2. Ion exposure: Beam voltage = 200 V, dose ≈ 1 x 10^{17} ion/cm^2

Microstructures with leads labeled A-G and dimensions assuming 25 nm depletion width on each side:

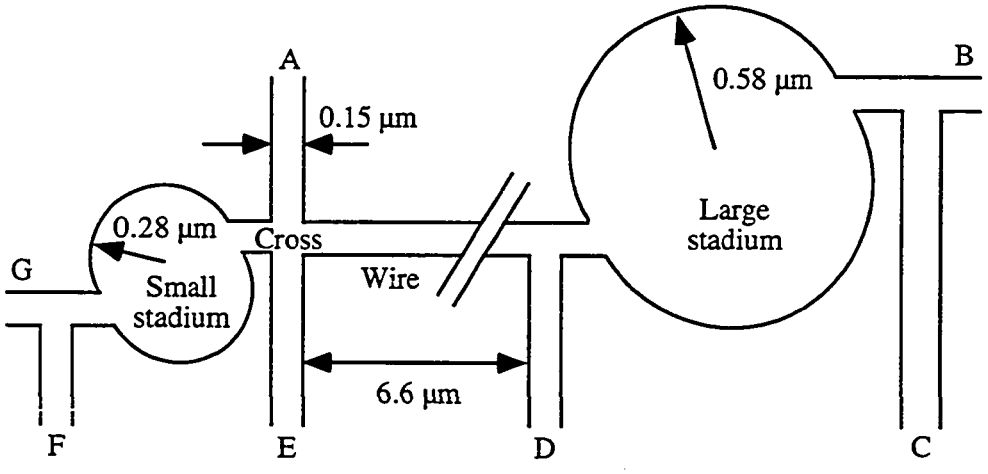

MBE17S9

Wafer: MBE17

Large scale fabrication: Pattern #1 from NNF mask of 10/13/94
1. 100 μm square mesa etch: 1800 ± 50 Å
2. Ohmic contacts: 380 Å Ni / 400 Å Ge / 2500 Å Au, RTA at 425 C, 60 s in N_2
3. Metal wiring: 50 Å Ti / 5000 Å Au

Microstructure fabrication: Pattern Chaos6
Isolation trenches: 230 ± 20 Å.
Gates: 50 Å Ti / 150 Å Pd / 800 Å Au

Microstructures with leads numbers and dimensions assuming 85 nm depletion width on each side:

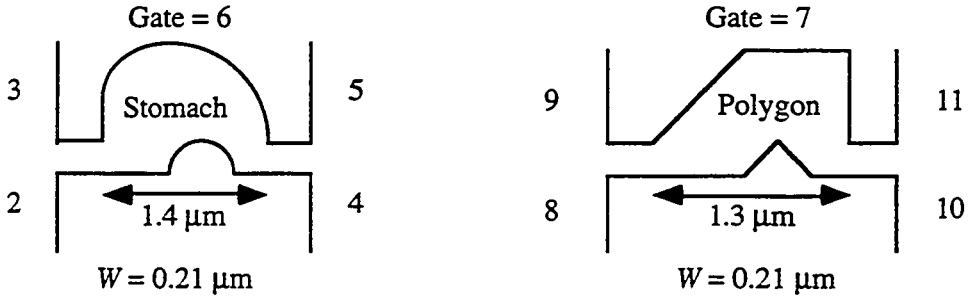

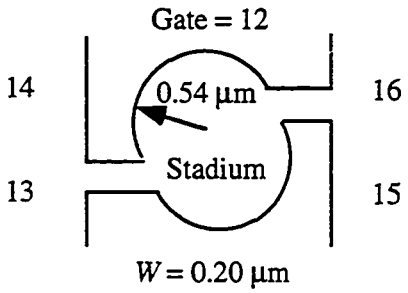

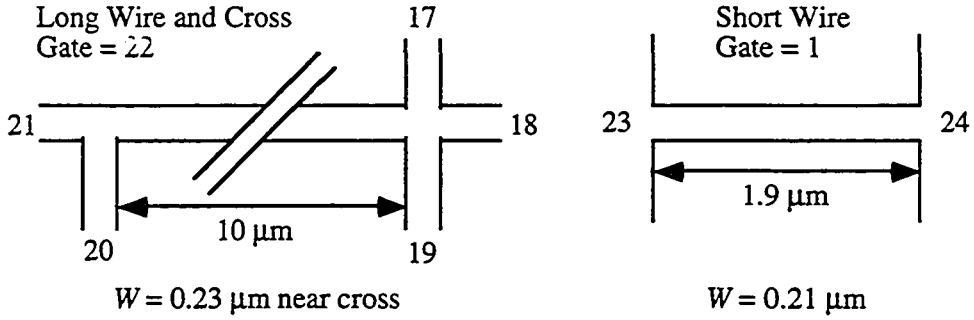

MBE17S1
(Bad ohmic contacts)

Wafer: MBE17

Large scale fabrication: Pattern #1 from NNF mask of 10/13/94
1. Ohmic contacts: 200 Å Ni / 200 Å Ge / 1000 Å Au, RTA at 450 C, 60 s in N_2
2. 100 μm square mesa etch: 1030 ± 50 Å
3. Metal wiring: 50 Å Ti / 100 Å Pd / 3000 Å Au

Microstructure fabrication: Pattern Chaos2
1. Isolation trenches: Approximately 300 Å. (SFM image taken *after* gate deposition.)
2. Gates: 50 Å Ti / 100 Å Pd / 1000 Å Au

MBE17S6
(Bad ohmic contacts)

Wafer: MBE17

Large scale fabrication: Pattern #1 from NNF mask of 10/13/94
1. Ohmic contacts: 200 Å Ni / 200 Å Ge / 1000 Å Au, RTA at 450 C, 60 s in N_2
2. Metal wiring: 50 Å Ti / 4000 Å Au
3. 100 μm square mesa etch: 1430 ± 50 Å

Microstructure fabrication: Pattern Chaos4
Isolation trenches: 400 ± 50 Å.
Gates: 50 Å Ti / 100 Å Pd / 350 Å Au

Appendix E

Ohmic Contact Problems

Alloyed NiGeAu ohmic contacts to the 2DEG of the GaAs/AlGaAs heterostructure are notorius throughout the experimental community for failing to work properly at low temperatures. The contacts may have linear I-V curves at room temperature, but when the sample is cooled the I-V curves become very nonlinear, the effective resistance becomes many times larger, and the contacts become very noisy. Such behavior was seen in the early samples made from wafer MBE17 using the shallow etch technique. About half the contacts became so highly resistive ($R > 500\ k\Omega$) that a reliable measurement of the cavity resistances was impossible. Other contacts had resistances of roughy 5 to 25 $k\Omega$ per contact, and this prevented the cavities from cooling properly, since by the Weidemann-Franz law the there is a thermal resistance proportional to the electrical resistance. Attempts were made to resurrect the bad contacts at low temperature using infrared light and by forcing a current of about 50 mA through them. The light had no effect and the large currents caused breakdown along paths other than through the contacts, causing considerable damage to the cavity gates in some cases.

A systematic study of the reason for the contact failure was not done, due to time constraints, but several aspects of the process were changed and the contacts improved, so those changes are summarized here.

- The quartzware of the rapid thermal annealer was etched in $HF:HNO_3$ (1:1) to remove impurities that may have been introduced by other materials heated in the chamber. Of particular concern was the fact that zinc had been used to check the temperature calibration of the thermocouple, and zinc is known to be a p-type dopant in GaAs (bad news for n-type contacts).
- The thickness of the Ni and Ge layers was increased from 200 Å to 400 Å, and the thickness of the Au layer was increased from 1000 Å to 2500 Å.
- The temperature of the rapid thermal anneal was decreased from 450 C to 425 C. The anneal time was left at 60 s.

Since most of these changes were made simultaneously, the relative importance of the changes cannot be determined. After the changes, samples were made with all 24 contact resistances $\approx$ 100 to 500 Ω at 4.2 K. With the new contacts, the cavities could be cooled to $\leq$ 200 mK (see Section 6.1).

Appendix F

Scaling of $\phi_0\alpha$ and γ with Lead Width

Jensen, 1991 has shown how to use the ergodic properties of classical chaotic scattering to derive scaling relations for the typical areas and lengths in various cavities. These arguments will not be reviewed here, but the expressions found by applying them to the Stomach cavity will be given explicitly. The definitions of the various quantities can be found in Chapter 2.

$$\alpha \propto \frac{\sqrt{\eta}}{A_{basic}} \propto \frac{\sqrt{\eta}}{L_{dir}^2}$$

$$\eta = \frac{2W}{perimeter} \propto \frac{W}{L_{dir}}$$

$\alpha_{Stom} = \frac{C_{Stom}}{L_{dir}^2}\sqrt{\frac{W}{L_{dir}}}$ where the constant C_{Stom} characterizes the shape

For $L_{dir} = 4W$, $\alpha_{Stom}L_{dir}^2 = 1.97$ (Baranger) $\Rightarrow C_{Stom} = 3.94$

For the measured Stomach, $L_{dir} = 1.4$ μm and $W = 0.21$ μm

$\alpha_{Stom} = 0.779$ μm^2, $\phi_0\alpha = 32$ G

$$\gamma = \frac{\eta}{L_{typical}} \propto \frac{\eta}{L_{dir}}$$

$$\gamma_{Stom} = \dot{C}_{Stom}\frac{W}{L_{dir}^2}$$

For $L_{dir} = 4W$, $\gamma L_{dir} = 0.26$ (Baranger) $\Rightarrow \dot{C}_{Stom} = 1.04$

For the measured Stomach, $\gamma_{Stom} = 0.111$ μm^{-1}

References

Baker, G.L. and Gollub, J.P. (1990), *Chaotic Dynamics: An Introduction* (Cambridge University Press, New York).

Baranger, H.U. and Mello, P.A. (1994a), *Phys. Rev. Lett.* **73**, 142.

Baranger, H.U. and Mello, P.A. (1994b), "How Phase-Breaking Affects Quantum Transport Through Chaotic Cavities", preprint.

Baranger, H.U. and Stone, A.D. (1989), *Phys. Rev.* **B40**, 8169.

Baranger, H.U., Jalabert, R.A., and Stone, A.D. (1993a), *Phys. Rev. Lett.* **70**, 3876.

Baranger, H.U., Jalabert, R.A., and Stone, A.D. (1993b), *Chaos* **3**, 665.

Baranger, H.U., DiVincenzo, D.P., Jalabert, R.A., and Stone, A.D. (1991), *Phys. Rev.* **B44**, 10 637.

Beenakker, C.W.J. and van Houten, H. (1989), *Phys. Rev. Lett.* **63**, 1857.

Beenakker, C.W.J. and van Houten, H. (1990), in *Electronic Properties of Multilayers and Low-Dimensional Semiconductor Structures*, edited by J.M. Chamberlain, L. Eaves, and J.C. Portal (Plenum, New York).

Beenakker, C.W.J. and van Houten, H. (1991), in *Solid State Physics*, Vol. 44, edited by Ehrenreich, H. and Turnbull, D. (Academic Press, New York)

Bergmann, G. (1984), *Physics Reports* **107**, 1.

Berry, M.J., Katine, J.A., Marcus, C.M., Westervest, R.M., and Gossard, A.C. (1994a), *Surf. Sci.* **305**, 495.

Berry, M.J., Baskey, J.H., Westervest, R.M., and Gossard, A.C. (1994b), *Phys. Rev.* **B50**, 8857.

Bird, J.P., Ishibashi, K., Aoyagi, Y., Sugano, T., and Ochiai, Y. (1994), *Phys. Rev.* **B50**, 18 678.

Blumel, R. and Smilansky, U. (1988), *Phys. Rev. Lett.* **60**, 477.

Blumel, R. and Smilansky, U. (1989), *Physica* **D36**, 111.

Blumel, R. and Smilansky, U. (1990), *Phys. Rev. Lett.* **64**, 241.

Buttiker, M. (1986), *Phys. Rev. Lett.* **57**, 1761.

Chan, I.H., Clarke, R.M., Marcus, C.M., Campman, K., and Gossard, A.C. (1994), "Ballistic Conductance Fluctuations in Shape Space", preprint.

Chang, A.M., Baranger, H.U., Pfieffer, L.N., and West, K.W. (1994), *Phys. Rev. Lett.* **73**, 2111.

Cheeks, T.L., Roukes, M.L., Scherer, A., and Craighead, H.G. (1988), *Appl. Phys. Lett.* **53**, 1964.

Clarke, R.M., Chan, I.H., Marcus, C.M., Duruöz, C.I., Harris, J.S. Jr., Campman, K., and Gossard, A.C. (1994), "Temperature Dependence of Phase Breaking in Ballistic Quantum Dots", preprint.

Coleridge, P.T. (1991), *Phys. Rev.* **B44**, 3793.

Doron, E., Smilansky, U., and Frenkel, A. (1991), *Physica* **D36**, 367.

Dresselhaus, P.D., Papavassiliou, C.M.A., and Wheeler, R.G. (1991), *Phys. Rev. Lett.* **68**, 106.

Giannoni, M.-J., Voros, A., and Zinn-Justin, J., editors (1991), *Chaos and Quantum Physics* (North-Holland, New York).

Gutzwiller, M.C. (1991), *Chaos in Classical and Quantum Mechanics* (Springer-Verlag, New York).

Imry, Y. (1995), *Introduction to Mesoscopic Physics*, to be published by Oxford University Press.

Ismail, K., Washburn, S., and Lee, K.Y. (1991), *Appl. Phys. Lett.* **59**, 1998.

Jalabert, R.A., Baranger, H.U., and Stone, A.D. (1990), *Phys. Rev. Lett.* **65**, 2442.

Jensen, R.V. (1987), *American Scientist* **75**, 168.

Jensen, R.V. (1991), *Chaos* **1**, 101.

Keller, M.W., Millo, O., Mittal, A., Prober, D.E., and Sacks, R.N. (1994), *Surf. Sci.* **305**, 501.

Klepper, S.J. (1991), Ph.D. thesis, Yale University.

Kurdak, Ç., Chang, A.M., Chin, A. and Chang, T.Y. (1992), *Phys. Rev.* **B46**, 6846.

Landauer, R. (1970), *Phil. Mag.* **21**, 863.

Lee, K.Y., Kern, D.P., Ismail, K., and Washburn, S. (1991), *J. Vac. Sci. Technol.* **B9**, 2834.

Lee, P.A., Stone, A.D., and Fukuyama, H. (1987), *Phys. Rev.* **B35**, 1039.

Li, F., Spencer, G.F., Wang, T., Andrews, C.C., and Kirk, W.P. (1993), *J. Vac. Sci. Technol.* **B11**, 2592.

Lin, W.A., Delos, J.B., and Jensen, R.V. (1993), *Chaos* **3**, 655.

Lounasmaa, O.V. (1974), *Experimental Principles and Methods Below 1 K* (Academic Press, New York).

Marcus, C.M., Rimberg, A.J., Westervelt, R.M., Hopkins, P.F., and Gossard, A.C. (1992), *Phys. Rev. Lett.* **69**, 506.

Nixon, J. and Davies, J. (1990), *Phys. Rev.* **B41**, 7929.

Richardson, R.C. and Smith, E.N. (1988), *Experimental Techniques in Condensed Matter Physics at Low Temperatures* (Addison-Wesley, Redwood City).

Rooks, M.J. (1987), Ph.D. thesis, Yale University.

Roukes, M.L., Scherer, A., Allen, S.J., Craighead, H.G., Ruthen, R.M., Beebe, E.D., and Harbison, J.P. (1987), *Phys. Rev. Lett.* **59**, 3011.

Roukes, M.L., Scherer, A., and Van der Gaag, B.P. (1990), *Phys. Rev. Lett.* **64**, 1154.

Scherer, A. and Roukes, M.L. (1989), *Appl. Phys. Lett.* **55**, 377.

Scherer, A., Roukes, M.L., Craighead, H.G., Ruthen, R.M., Beebe, E.D., and Harbison, J.P. (1987), *Appl. Phys. Lett.* **51**, 2133.

Stone, A.D., Mello, P.A., Muttalib, K., and Pichard, J.-L. (1991), in *Mesoscopic Phenomena in Solids*, edited by Altshuler, B.L., Lee, P.A., and Webb, R.A. (North-Holland, New York).

Umbach, C.P., Santhanam, P., van Haesendonck, C., and Webb, R.A. (1987), *Appl. Phys. Lett.* **50** 1289.

Washburn, S. and Webb, R.A. (1986), *Advances in Physics* **35**, 375.